Fall 12-18-2020

Design and Fabrication of a 3-Dimensional Capacitive-based Force Sensor

Md Shafiqur Rahman
md.s.rahman@maine.edu

DESIGN AND FABRICATION OF A 3-DIMENSIONAL CAPACITIVE-BASED FORCE SENSOR

by

Md Shafiqur Rahman

B.Sc. Khulna University of Engineering and Technology, 2014

A THESIS

Submitted in Partial Fulfillment of the

Requirements for the Degree of

Master of Science

(in Mechanical Engineering)

The Graduate School

The University of Maine

December 2020

Advisory Committee:

Babak Hejrati, Assistant Professor of Mechanical Engineering, Chair

Mohsen Shahinpoor, Professor of Mechanical Engineering

Vincent Caccese, Professor of Mechanical Engineering

DESIGN AND FABRICATION OF A 3-DIMENSIONAL CAPACITIVE-BASED FORCE SENSOR

By Md Shafiqur Rahman

Thesis Advisor: Dr. Babak Hejrati

An Abstract of the Thesis Presented

in Partial Fulfillment of the Requirements for the

Degree of Master of Science

(in Mechanical Engineering)

December 2020

The detection of abnormal gait patterns is imperative for early diagnoses and treatment of serious health issues such as loss of mobility and balance, risk of falls, cardiovascular disease, etc. Human gait analysis is the tool used to detect abnormal gait patterns. Gait analysis also can help to understand the cause of gait abnormalities and to make a treatment plan for individual patients. Ground reaction forces (GRFs) at the foot during walking or running are essential for kinetic analysis of the human gait. However, there are no wearable systems that can directly measure three-directional (3D) forces during daily walking. Currently, the 3D GRFs are either measured by estimating the shear forces from the normal force measured by pressure insoles, or using instrumented treadmills, or walking on a limited number of force platforms in gait labs. There are always errors associated with estimating other force components from the normal one. Also, instrumented treadmills and force platforms are very expensive, and treadmill walking may not be sufficiently similar to over ground walking. So, a wearable system is needed to measure 3D ground reaction forces during walking for complete gait analysis in both indoor and outdoor conditions. The main challenge in developing such a wearable

system or a smart shoe to measure 3D GRFs lies in the lack of a low-profile, lightweight, and portable force sensor that can measure 3D forces during the user's walking. The main research objective here is to develop such a wearable force sensor for gait analysis applications.

In this thesis work, the design, analysis, and fabrication of a capacitive-based 3D force sensor have been presented. The sensor mainly consists of an elastic element, three parallel plate capacitors, capacitance measuring electronics, and a bottom plate. The elastic component deforms under applied forces and this deformation leads to capacitance changes that are measured by the electronic circuit. An experimental setup was built to perform experiments needed to find the force-capacitance relationship and evaluate the sensor's performance. A calibration matrix was found between the applied forces and the capacitance changes using the linear least-squares method.

Five types of experiments were conducted to evaluate the developed sensor and the evaluated matrix, where the estimated forces were compared with the reference values obtained by commercially available force sensors. The developed sensor could measure forces in all three directions with the mean errors of less than 4.5%. The experiments showed that the force sensor could successfully decouple the forces applied in different directions and had no residual offsets when no force was applied. Also, no drifts and changes in the behavior of the sensor were observed after a long period of usage. The developed sensor also demonstrated adequate repeatability, hysteresis characteristics, and dynamic response. The measurement errors increased in some scenarios, in which the forces were simultaneously applied in different directions. Future work can be done to reduce the error in the combined conditions.

TABLE OF CONTENTS

LIST OF TABLES

LIST OF FIGURES

CHAPTER 1

INTRODUCTION

1.1. Gait

A person's way of walking is called gait. Michael W. Whittle [1] defined normal human walking and running as a method of locomotion involving the use of the two legs. Normal walking depends on different parts of our body such as brain, eyes, ears, muscles, nervous system etc. When one of these body parts which control a person's, walking does not function in the normal way, then the person cannot walk in the usual way. This deviation from normal walking is called abnormal gait or pathological gait.

Figure 1.1: Pathological gait

Pathological gait can be occurred due to various reasons including neurological conditions (e.g. sensory or motor impairments), orthopedic problems (e.g. osteoarthritis and skeletal deformities) and medical conditions (e.g. stroke) [2]. Pathological gait disturbs the normal life of the patients, decrease the quality of life, increase their dependency on other people, require twice the metabolic energy of the healthy gait [3], and decrease the ability to avoid obstacles [4]. In 2008, about 33 million American adults had balance problems caused by medications, ear infection, injuries or neurological disorders [5].

1.2 Gait Analysis

The systematic study and investigation of human walking is called gait analysis. Through gait analysis, different gait parameters can be measured and analyzed to describe fundamental gait characteristics [6]. These fundamental characteristics help to identify pathological gait. Gait analysis is also done to learn about a condition affecting a group of patients, to assess rehabilitation outcomes by analyzing the effect of an intervention [7], develop prosthetics for trans-tibial amputee (TTA) patients [8], design ankle-foot orthoses for stroke patients [9], early detection of gait imbalance in older adults to reduce fall-induced injuries [10].

There are four types of gait analysis such as electromyography (EMG), spatio-temporal, kinematics, and kinetics.

1.2.1 Electromyography

Muscles are the main engine for producing movements. Through electromyography, we can know whether a muscle is active during a gait cycle [11], to

detect asymmetric phenomenon in adolescent idiopathic scoliosis (AIS) patients [12].
There are commercial electromyography (EMG) hardware and software available for
electromyography analysis. Bovi et al. [11] used 8-channel wireless electromyography,
ZeroWire (Aurion, Milano, Italy) with 10 mm diameter adhesive electrodes to analyze
the activation of particular muscles in different particular gait activities (toe-walking,
heel-walking, step ascending and step descending). Mahaudens et al. [12] recorded
electrical bilateral activity of some muscles by a telemetry EMG system (Telemg, BTS,
Italy) with surface electrodes (Medi-Trace, Graphic Controls Corporation, NY, USA),
based on the timing and duration of EMG muscular contraction expressed as a percentage
of the gait cycle.

Figure 1.2: Electromyography

1.2.2 Spatio-Temporal

In spatio-temporal gait analysis, spatial (distance) and temporal (time) parameters of gait are measured. Spatial parameters include step length which is the distance between corresponding successive points of heel contact of the opposite feet and stride length which is the distance between successive points of heel contact of the same foot. Temporal parameters include cadence which is the number of steps per unit time and speed of walking or running. In a normal gait pattern, right step length is equal to left step length, stride length is equal to double the step length. So, by measuring and comparing these parameters, pathological gait can easily be detected. Yoon et al. [13] compare the spatiotemporal parameters of freezing of gait (FOG) patients after Hypoxic-ischemic brain injury (HIBI) compared to patients without FOG after HIBI.

Normally people use photoelectric system [14] or pressure mat [15] for doing spatio-temporal gait analysis. A photoelectric system mainly consists of a light transmitting unit and a light receiving unit. Subjects walk between these two units and the spatio-temporal gait parameters are measured. Pressure mat consists of pressure sensors under the mat and when subjects walk on the mat, the spatio-temporal gait parameters can be measured.

1.2.3 Kinematic

Kinematic is the scientific geometric description of motion, in terms of displacements, velocities, and acceleration irrespective of the influence of weight and force. Kinematic analysis gives us the information about position and orientation of the body segments, the angles of the joints and the corresponding linear and angular velocities and accelerations [1].
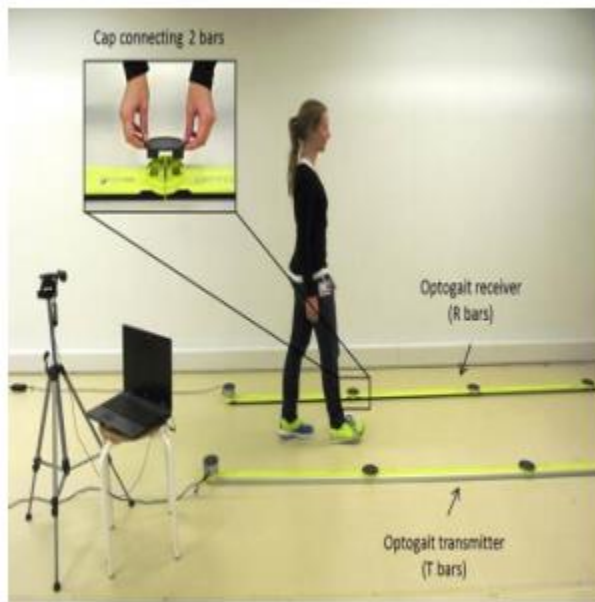
Figure 1.3: Spatio-temporal gait analysis (a) photoelectric system [14], and (b) pressure mat

Kinematic gait analysis is used to compare the kinematic parameters of freezing of gait (FOG) in patients after the hypoxic-ischemic brain injury (HIBI) compared to patients without FOG after HIBI [13], describe the presence of joint level impairments and associated kinematic patterns during gait in children with recurrent clubfoot [16], compare the kinematic gait variables between able-bodied subjects and adolescent idiopathic scoliosis (AIS) patients [12], evaluate the psychometric properties of kinematic gait analysis in knee and hip of osteoarthritis patients [17], identify abnormalities in the gait of spinal cord injured (SCI) patients, and evaluate the role of spasticity in altering the gait patterns in SCI individuals [18].

Earlier kinematic analyses were done by visual observations [19] [20] but it has couple of serious limitations. With the invention of high-quality, high-framerate digital imaging systems, researchers can do the kinematic analysis precisely. Motion data are collected using computerized gait system (VICON MX-T10 Motion Analysis System, Oxford Metrics Inc, Oxford, UK) with sixteen reflective markers [13], 12 camera Vicon 512 Motion Capture System (Vicon, Los Angeles, CA) [16], Elite system (BTS, Italy) consists of six infrared cameras and twenty two reflective markers [12]. Connor et al. [21] developed an algorithm to automatically determine the timing of heel strike and toe off from kinematic data recorded by a four-camera system (Motion Analysis Corporation, Santa Rosa, CA) with a sampling frequency of 60 Hz, with 15 marker Helen Hayes Hospital set. Their algorithm eliminated the necessity of force plates to detect these gait events. Cutlip et al. [22] developed an instrumented walkway system which was portable, required little set-up time. It had six sensor pads to measure the kinematic parameters of gait. They compare their system with a video-based system and found that their system could accurately measure the temporal parameters.

People also did kinematic analysis using electromagnetic tracking systems (ETS) which are free from marker obscurement problems, record absolute movements with six-degree-of-freedom, and relatively inexpensive than image-based kinematic measurement systems [23] [24] [25] [26]. These systems also have some disadvantages such as limited capture volume and susceptibility to magnetic interference from metal objects located within and near their capture volume [25].
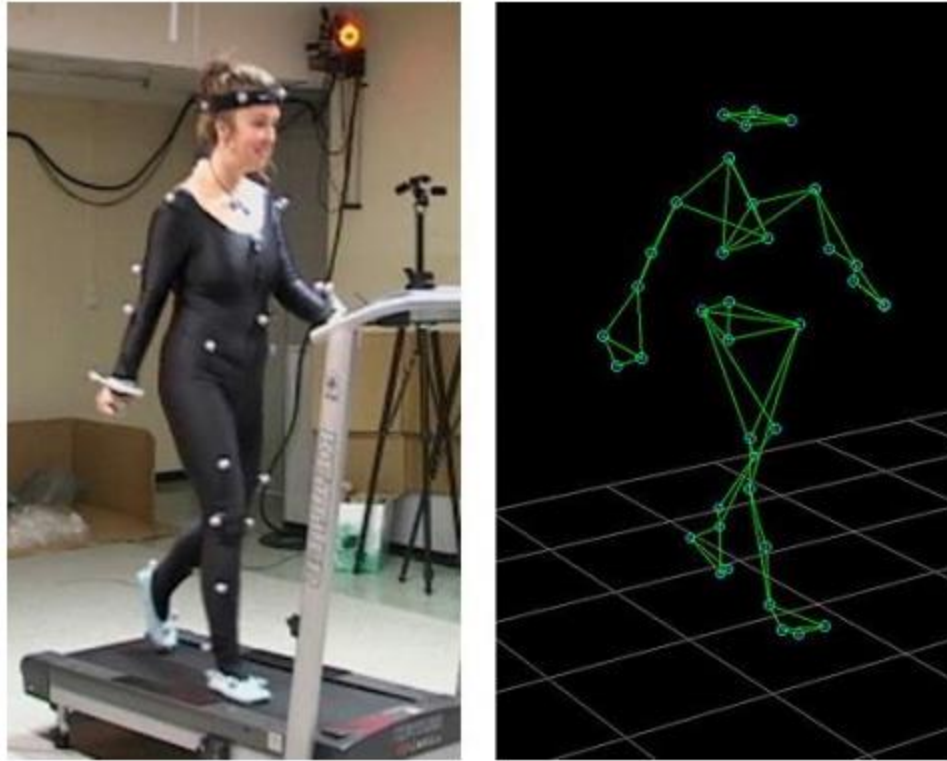
Figure 1.4: Kinematic gait analysis using vision-based motion capture system

1.2.4 Kinetics

Kinetic gait analysis is the study of the forces involved in the production of movements. In this type of analysis, ground reaction forces (GRF), net joint movements, and powers at the hip, knee ankle are measured and analyzed.

1.2.4.1 Ground Reaction Force (GRF)

When people walk or run on the ground, the reaction forces which are supplied by the ground in contact with the body is called ground reaction force (GRF). These are the reactions forces which we apply to the ground by producing a certain combination of muscle actions. Ground reaction force has three components. One component is vertical

force which is a normal force, acts perpendicular to the ground. This vertical force is the reaction force of the body weight. The other two components are anterior-posterior force and medial-lateral force which are shear forces and associate with our movement.

Figure 1.5: Ground reaction forces

Kinetic gait analysis helps to calculate three direction ground reaction forces to calculate the contributions of gravity and energy, compare the kinetic parameters of freezing of gait (FOG) in patients after Hypoxic-ischemic brain injury (HIBI) compared to patients without FOG after HIBI [13], detect and quantify the hind limb lameness and spinal ataxia in horses [27], compare the ground reaction force features between left and right leg during normal gait cycle [28], evaluate the biomechanics of running under controlled conditions [29], to understand the role of the knee musculature during trans-tibial amputee (TTA) gait [8].

Figure 1.6: Kinetic gait analysis (a) using instrumented treadmill, and (b) force plate

Force plates [8] [13] [27] [28] [29] and instrumented force treadmill [29] [30] [31] are normally used for kinetic gait analysis. But with the force plates we have only limited walking steps and sometimes subjects alter their gait to target the force plate [10] [32]. On the other hand, the instrumented treadmills are too much expensive and in some cases treadmill gait differs from normal gait as it does not require torso motion [9] [33]. Also, we cannot do kinetic gait analysis for unstructured environment such as stair climbing and walking on uneven surface by using force plates and instrumented treadmills. So, we need a wearable system for kinetic gait analysis which can be attached to the body of the subject so that we can do kinetic gait analysis in any walking condition.

Rosquist et al. [34] used Nano composite piezo-responsive foam (NCPF) sensor technology for estimating ground reactions forces. Nano composite piezo-responsive

9

foam produces voltage when it deforms. They inserted four NCPF sensors inside the

shoe insole and calibrated the sensors using force plate and motion capture data to predict

the ground reaction forces. Cordero et al [35] combined pressure insole data and motion
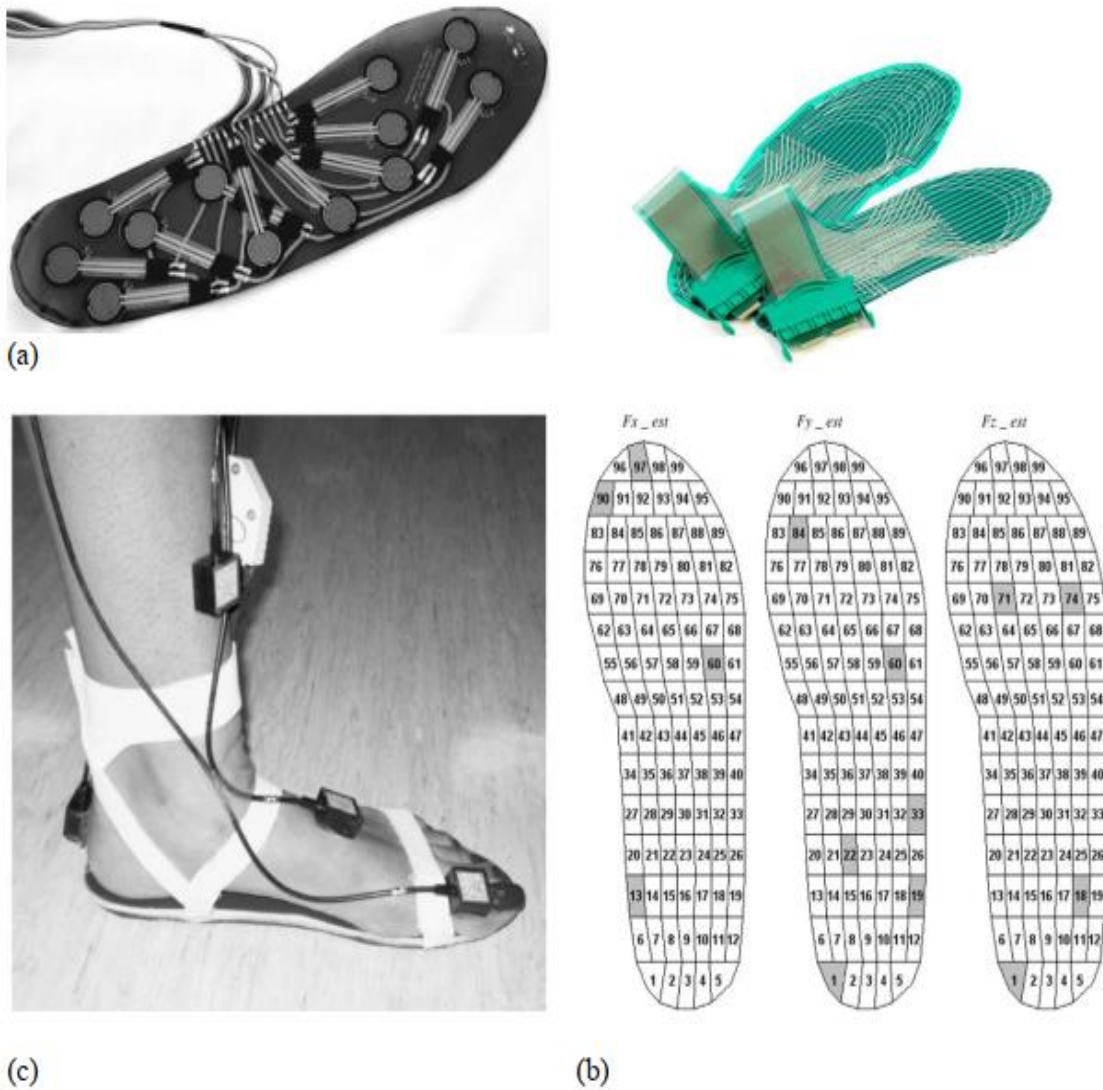
Figure 1.7: Wearable system for kinetic gait analysis using (a) force sensing resistors

(FSRs) [9], (b) pressure insole [33], and (c) inertial measurement units (IMUs) [34]

capture data and developed an algorithm to calculate complete ground reaction forces. But as this method relies on motion capture system, thus this system cannot be used to do kinetic gait analysis in outdoor environment. Fong et al. [36] used a pressure insole consists of 99 pressure sensors and used stepwise linear regression to estimate the ground reaction forces. Their system does not need any motion capture data to estimate the forces. They calibrated the sensors using motion capture data and force plate data. Rouhani et al. [37] also developed a wearable system for kinetic gait analysis using plantar pressure insoles. Then they developed a wearable system which consisted of four inertial sensors and a plantar pressure insole. The inertial sensors were placed on toes, forefoot, hindfoot, and shank [38].

All the above systems measure the vertical force and estimate or predict other two ground reaction forces. A wearable three-dimensional force measuring system can be a good alternative for doing gait analysis.

1.3 Force Sensor

Force sensors are devices that convert forces into measurable outputs signals and the magnitude of the forces can be measured from those output signals. Most of the multi-component force measuring sensor work on the following principle: Multi-component forces act on an elastic element. The physical change (displacement, strain, potential) of the elastic element is converted into electrical signals by measuring element and measuring circuit. In order to convert multi-component forces into electrical signals, several measurement techniques such as resistive, capacitive, optical, piezoelectric have been used. Then calibration techniques are used to convert the electrical signals into force values.

1.3.1 Strain Gauge Based Sensor

Earlier, most of the researchers worked on resistive based force sensor which uses strain gauges as a force sensing element. Research on resistive based force sensors mainly focuses on optimization of elastic structure to increase the deformation and reduce the coupling error, use finite element analysis to find the best position for the strain gauges by using finite element analysis software (ANSYS, ABAQUS). Researchers' first use Maltese cross type beam [39] [40]. But using this type of structure results in large coupling error. So, researchers tried different ways to reduce the errors. Mastinu et al. [41] installed elastic sliding spherical joints. Some researchers also used parallel mechanism (PM) [42] as an elastic element. Joo et al. [43] used parallel plate structure (PPS) with beams arranged in parallel which connects a fixed block and a movable block. Kim [44] used more modified parallel-plate beams (PPBs) for lower deflection of the sensor due to bending moment and lower twist due to twist moment from the applied force/moment to sensor. Sanders et al. [45] used parallel plate spring at the end of elastic element for greater deformation and for increasing the sensitivity of the sensor. Quinn and Mote [46] used mathematical modeling and design optimization technique to develop an uncoupled six-degree of freedom dynamometer. Ma and Song [47] proposed a simple mechanical model where they considered all the deformable beams of the elastic bodies as deep beams or short beams, analyzed the mechanical model using Timoshenko beam theory, and validated by finite element analysis and calibration experiments The elastic element contains four cross elastic beams and eight compliant beams.

1.3.2 Capacitive Based Sensor

But manufacturing of these complex structure is hard so that the cost of fabrication is much higher. Also, due to lack of automation technology, highly time-consuming manual works are needed for bonding the strain gauges to the elastic elements. So, it is hard to maintain the quality. So, researchers start using capacitive technology which has higher sensitivity, resolution, compactness, and resistance to severe environments.

1.3.2.1 Parallel Plate Capacitor

A parallel plate capacitor is the simplest form of capacitor. It can be made by placing two metallic plates at a distance parallel to each other.

The capacitance of a parallel plate capacitor,

$$C = \frac{\varepsilon \, A}{d}$$

(1.1)

Here,

C = Capacitance of the capacitor

A = Area of the parallel plate

d = Distance between two parallel plates

$\varepsilon = k\varepsilon_0$, where k = relative permittivity of dielectric material and $\varepsilon_0 = 8.854 \times 10^{-12}$ F/m

The capacitance of a parallel plate capacitor depends on the surface area A, distance between two plates d, and the relative permittivity of the dielectric material between two plates, k. If the area and the dielectric material between two parallel plates are fixed, then the capacitance of the parallel plate capacitor will be changed with the change of distance between the parallel plates. This phenomenon is used in capacitive based sensors.

$$C = \frac{\epsilon A}{d}$$
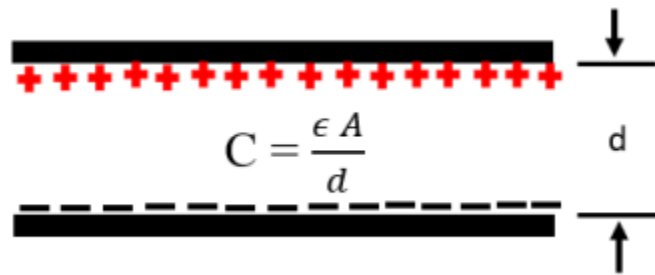
Figure 1.8: Schematic diagram of a parallel plate capacitor

1.3.2.2 Research on Capacitive Based Sensor

The research on capacitive based force sensor mainly focuses on number and orientation of capacitors, and calibration techniques. Tiwana et al. [48] developed a shear force measuring sensor using parallel plate capacitor concept. In a capacitive based force measuring sensor, the physical change of the elastic element is measured by the capacitance change of the capacitors. Viry et al. [49] and Peng et al. [50] used four parallel plate capacitors to develop three axial force sensor and to measure the normal and the shear elasticity. They measure the deflection of membrane under the normal force

by averaging the four capacitance values and measure the deflection of membrane under the shear force by taking the differences of capacitance values of the four capacitors in that direction.

Kim et al. [51] developed a six-axis capacitive force/torque sensor based on dielectric elastomer. They made the capacitors by cutting grooves in branch of the elastic structure, plastering silver paste on both sides of grooves, soldering wires, and filling up the grooves by dielectric elastomer. They used optimization technique to find the best dimensions, positions and distances of the grooves by finite element analysis using ANSYS. Lee et al. [52] placed six electrodes on a single printed circuit board, so no manual wiring was needed for connecting sensing elements, simplify the fabrication process. They used an electrically grounded solid metal disc with groove in its bottom surface as ground electrode. This one solid metal disc formed six parallel plate capacitors with the six electrodes on the PCB. They optimize their parallel plate capacitors by finding the best initial horizontal and vertical offset using COMSOL. They used vertical offset of the ground electrode to measure the normal forces and horizontal offset of the ground electrode to measure the shear forces. Later, Kim et al. [53] showed that the shear force sensing in two orthogonal electrodes is five times higher than the two parallel-electrode configurations. So, they used three orthogonal-electrode configuration capacitors for the shear force measurement. Lee et al. [54] and Kim et al. [55] [56] developed laparoscopic grasping tool with force sensing capability by placing capacitive based multi-component force sensor at the distal end of the tool shaft. They both used three discrete in-plane lower electrodes and a common ground electrode but used different shape elastic element and different orientation for placing the electrodes.

1.3.3 Calibration

Calibration of a force sensor is one of the most important things due to cross coupling, joint frictional moment, manufacturing error such as machining error, assembling error. Also, to convert the electrical quantities into force values, a relationship must be established between applied forces and the electrical quantities. Kim et al. [51] used a calibration matrix to establish the relation between forces and change of capacitances, and calculated the calibration matrix using singular value decomposition. Some researchers established the relation by using transformation matrix and used linear least-squares method to find all the elements of the transformation matrix [53] [56] [57] [55]. As the data from the developed sensors were highly nonlinear, an exponential fit was performed to fit the data linearly. Liang et al. [58] obtained the relationship between the applied force and the measured values (the output of A/D converter) by static decoupling method based on Neural Network (NN). Here, the input vector is the electrical quantity (output voltages of the sensitive bridge circuits), the output vector is the forces/torques outputs of the sensor after decoupling, the learning samples are a group of applied forces/torques and the corresponding outputs electrical quantities, and the weight value of the network training is the decoupling matrix. But a normal neural network has low computational efficiency. So, Liang et al. [59] proposed to use artificial neural network (ANN) and showed a three-layer artificial neural network (ANN) with tan-sigmoid transfer in the hidden layer to decouple and calibrate the force sensors. Oh et al. [60] used deep-neural-network (DNN) which has a non-linear activation function to handle the highly nonlinear output data and powerful fitting capability. It can learn the decoupled correlation about forces and torques.

In this thesis work, a capacitive based three directional force measuring sensor is developed. The main purpose of this sensor is to use in gait analysis application. This sensor can give force measurement in three direction. That means, this one sensor can measure all three component of the ground reaction forces at a point. As the discussion above, currently researchers use one directional normal force measuring sensor to measure the vertical ground reaction force and use different predictive formula to predict the other two components of the ground reaction force (anterior-posterior force, medial-lateral force). Using this three directional force measuring sensor will help the researcher to measure all the three components of ground reaction forces directly.

To develop the sensor, first theoretical analyses have been done. First, the displacement behavior of the ground electrode has been analyzed. Then considering the displacement behavior, capacitance analysis has been done to see the change of capacitance behavior under different direction of forces. This analysis has helped to make a relationship between the physical change of the elastic element and the electrical change of the measuring element. This relationship has been used to find the calibration matrix for the developed sensor. The sensor has been modeled and simulated in COMSOL to see whether the displacement behavior of the elastic element and the capacitance change behavior of the capacitors match with the theoretical analyses. Then using this modeling, simulations have done first to find the calibration. Then, the calibration matrix has been evaluated by doing more experiments. After then, a prototype sensor has been developed. The mechanical parts of the developed sensor have been fabricated using a CNC machine. The material of the mechanical parts is aluminum 7075 T6. The electronic parts are in two printed circuit board (PCB). Then through

experiments, first, the prototype sensor has been calibrated and then, its performance has

been evaluated. A test setup has been built to do the experiments. This test setup can

apply force in three direction simultaneously and can be controlled using a computer.

CHAPTER 2

THEORETICAL ANALYSIS

2.1 Basic Design

In a capacitive-based force sensor, the physical change of the elastic element under applied force is converted into measurable output signal by capacitor. Figure 2.1 shows a schematic of the developed sensor. In this sensor, parallel plate capacitors are used. When the distance between two parallel plate of the capacitor changes, the capacitance of the capacitor also changes. So, among the two parallel plates, one plate is attached to a fixed bottom plate and another plate is attached to the elastic element. When the elastic element has some deformation under applied forces, the plate which is attached to the elastic element moves. As it moves, the distance between the parallel plate changes as well as the capacitance changes.
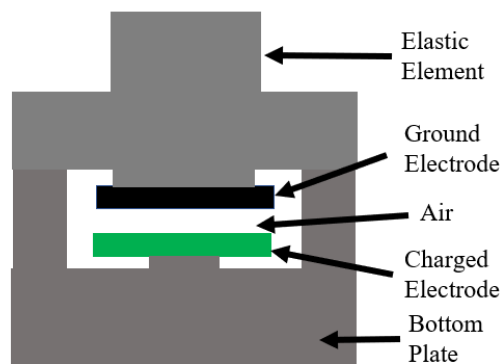
Figure 2.1: Basic design of the force sensor

2.2 Elastic Element

As shown in Fig. 2.2, the elastic element consists of a large hollow cylinder, a solid cylinder smaller than the hollow cylinder, and six beams. The large hollow cylinder is fixed and does not have any rotational or translational movement. The solid cylinder stays inside the hollow cylinder and have both rotation and translation under applied force. The solid cylinder is connected to the large hollow cylinder using these six beams. Among these six beams, three beams are connected to the larger hollow cylinder at one end and are connected to the solid cylinder at another end. As the large hollow cylinder has no movement under applied forces, so it works as a fixed support for these three beams. Also, as the solid cylinder rotates and translates under applied forces, it works as a roller support for these three beams. So, these three beams have fixed support at one end and roller support at another end. That means these three beams are behaving as propped cantilever beam. The other three beams have fixed support at both end and they behave as fixed beam.

When the normal forces are applied on the solid cylinder, the solid cylinder will move in only the normal force direction. It will not have any displacement in any other direction for the normal force. For example, if the direction of the normal force is along y-axis, the solid cylinder will have displacement in only y-direction (Fig. 2.3 a). The solid cylinder will have both translational and rotational movement due to the shear forces. The forces are applied on top of the central solid cylinder. The top surface of the central solid cylinder is higher than the position of the beams. So, the line of action of the force and the axis of rotation does not coincide to each other. That's why the shear forces will be converted into torque for the beams. The direction of translation may be either in the

shear force direction or opposite of the shear force direction. The rotation will be along the axis perpendicular to the shear force direction. For example, if the shear force is along x-axis, the solid cylinder will have translational movement in x-axis direction and rotational movement along z-axis. If the shear force is applied towards positive x-axis, then the rotation will be clockwise along positive z-axis and if the shear force is applied towards negative x-axis, then the rotation will be anti-clockwise along positive z-axis.
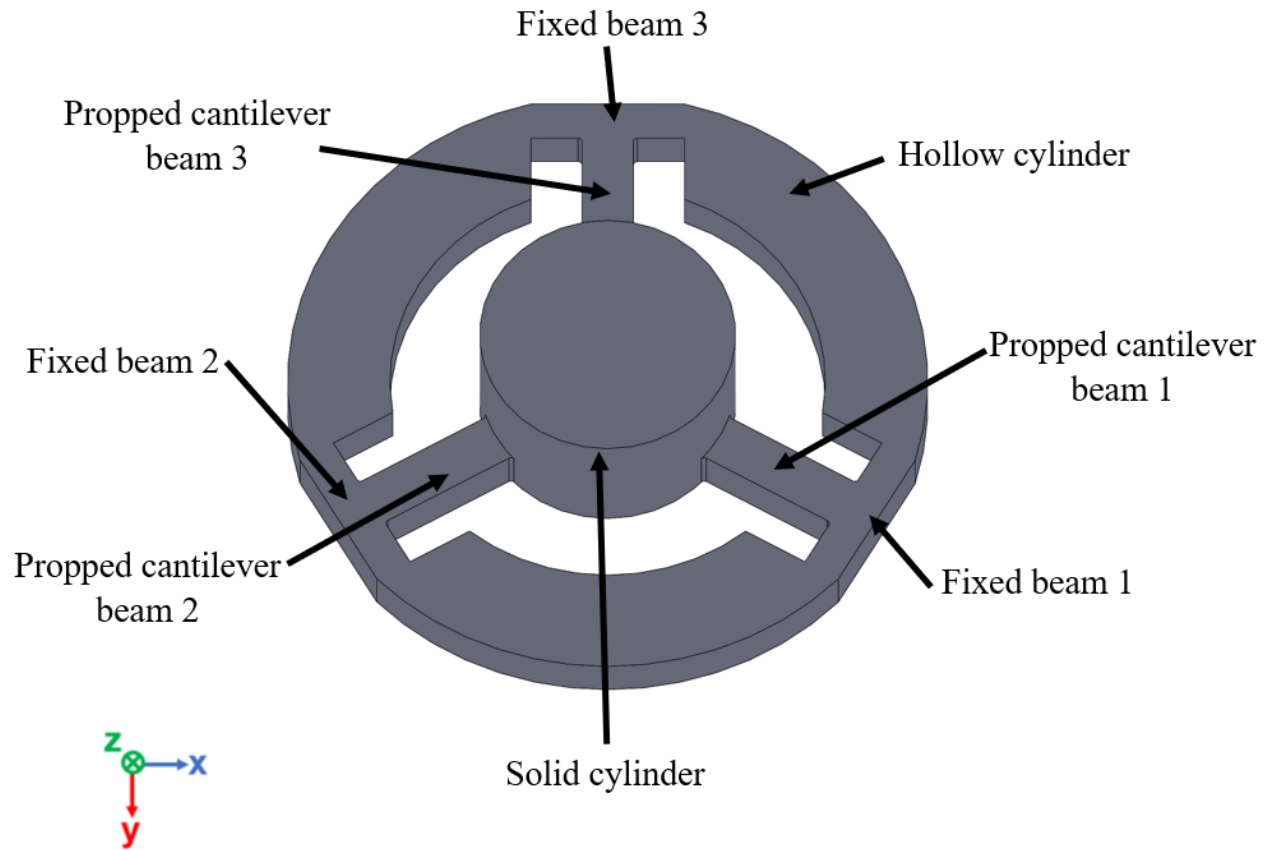
Figure 2.2: CAD model of the elastic element in the developed sensor

The solid cylinder will not have any significant movement towards z-axis for the shear force in x-axis direction (Fig 2.3 b). Similarly, when the shear force is applied towards z-axis, the solid cylinder will not have any significant movement towards x-axis, will have translational movement along z-axis, rotational movement along x-axis. Also, the rotation will be clockwise along the positive x-axis if the shear force is towards positive z-axis direction and the rotation will be anti-clockwise along the positive x-axis if the shear force is towards negative z-axis direction. The movement of solid cylinder depends on the dimensions of the beams and the solid cylinder. During the shear force, the deformation is not uniform, so the average of the deformation is considered.
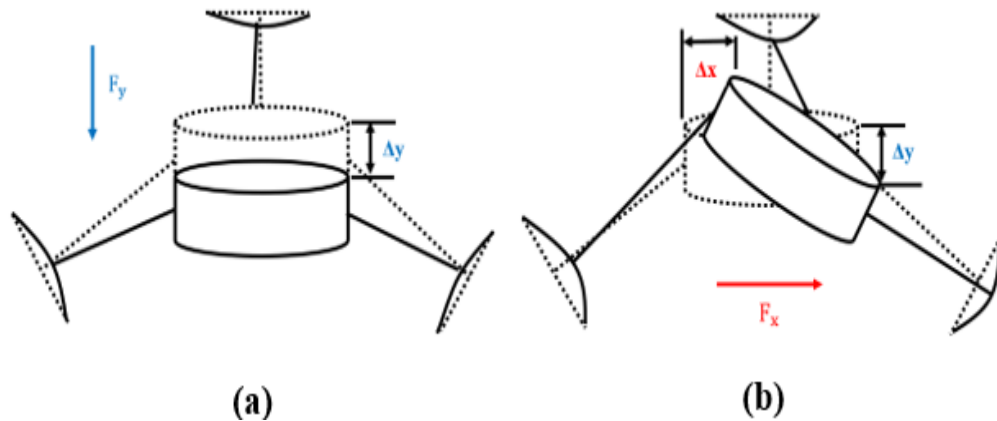
Figure 2.3: Movement of solid cylinder under applied force (a) normal force, and (b) shear forces

2.2.1 Behavior of Beams under Applied Forces:

There are three fixed beams and three propped cantilever beams. These beams have different displacement behavior under applied forces. The three fixed beams have similar displacement behavior under the normal force F_y but they have different displacement behavior under the shear force F_x and F_z. Similarly, the three propped cantilever beams have similar displacement behavior under the normal force F_y but have different displacement behavior under the shear force F_x and F_z.

The propped cantilever beam 1 is at an angle of 30^0 from the x – axis of the sensor. For the ease of analysis, a new axis is considered for this beam. It is shown in Fig. 2.4. The axes are defined as x_{b1}, y_{b1}, and z_{b1}. The y_{b1} axis is parallel to the sensor's y – axis. The other two axes, x_{b1} and z_{b1} are in the xz – plane of the sensor but at an angle of 30^0.
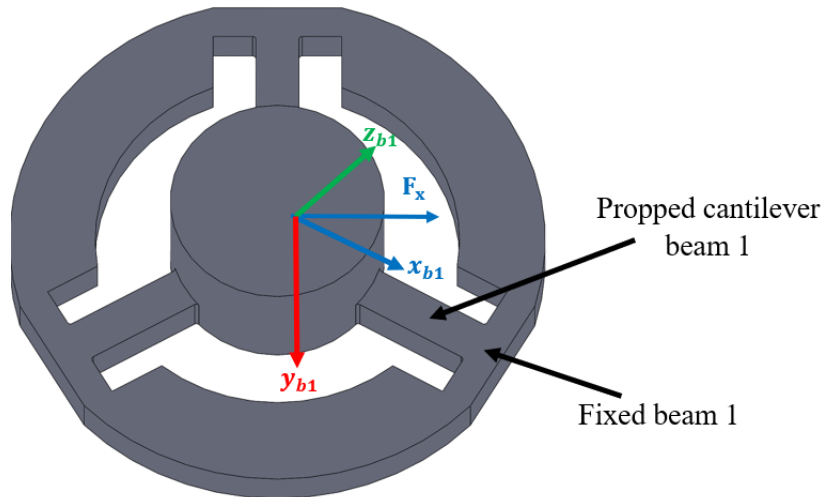
Figure 2.4: Propped cantilever beam 1 under shear force F_x

When the shear forces are applied in the x – axis direction (Fig. 2.4), the force divided into two force components for the beam. One component is towards x_{b1} axis which is $F_x \cos 30^0$ or $0.87F_x$, and another component is towards z_{b1} which is $F_x \sin 30^0$ or $0.5F_x$. Similarly, when the shear forces are applied in the z – axis direction (Fig. 2.5), the force divided into two force components for the propped cantilever beam 1. One force component is towards z_{b1} axis which is $F_z \cos 30^0$ or $0.87F_z$ and another component is towards x_{b1} which is $-F_z \sin 30^0$ or $-0.5F_z$.
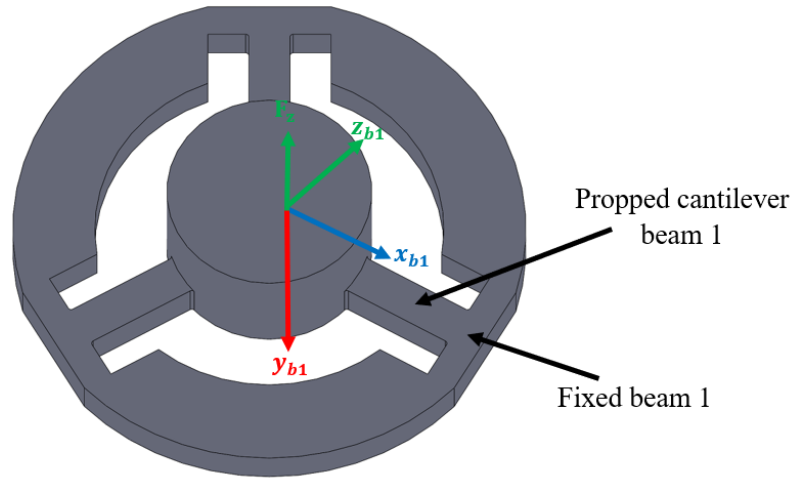
Figure 2.5: Propped cantilever beam 1 under the shear force F_z

Figure 2.6 shows the reference axes for the propped cantilever beam 2 and the shear force F_x. The reference axes for the propped cantilever beam 2 is denoted by x_{b2}, y_{b2}, and z_{b2}. The propped cantilever beam 2's xz – plane is parallel to the sensor's xz – plane. That means the y – axis of the main sensor and the propped cantilever beam 2 are parallel. But the x – axis of the propped cantilever beam 2 is at angle of 210^0 from the

main sensor's x – axis. So, the shear force F_x will be divided into two parts. One part is along the x_{b2} – axis and another part is along the z_{b2} – axis. As the angle between x – axis and x_{b2} – axis is 210^0, the force along x_{b2} – axis is $F_x cos210^0$ or $-0.87F_x$ and as the angle between x – axis and z_{b2} – axis is 60^0, the force along z_{b2} – axis is $F_x cos60^0$ or $0.5F_x$. The force along x_{b2} – axis will create bending moment, and the force along z_{b2} – axis will create torsion. Figure 2.7 shows the shear force F_z. The angle between z – axis and x_{b2} – axis is 120^0 so the force along x_{b2} – axis is $F_z cos120^0$ or $-0.5F_z$. The angle between z – axis and z_{b2} – axis is 210^0 so the force along z_{b2} – axis is $F_z cos210^0$ or $-0.87F_z$. The force along x_{b2} – axis will create bending moment, and the force along z_{b2} – axis will create torsion.
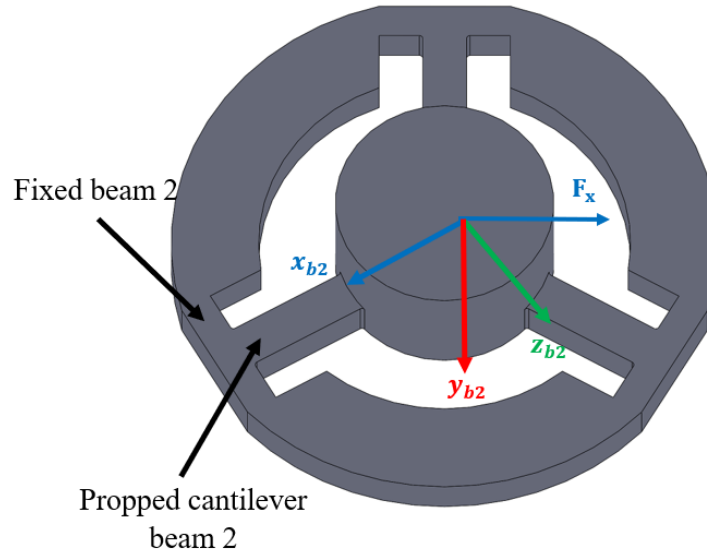
Figure 2.6: Propped cantilever beam 2 under the shear force F_x
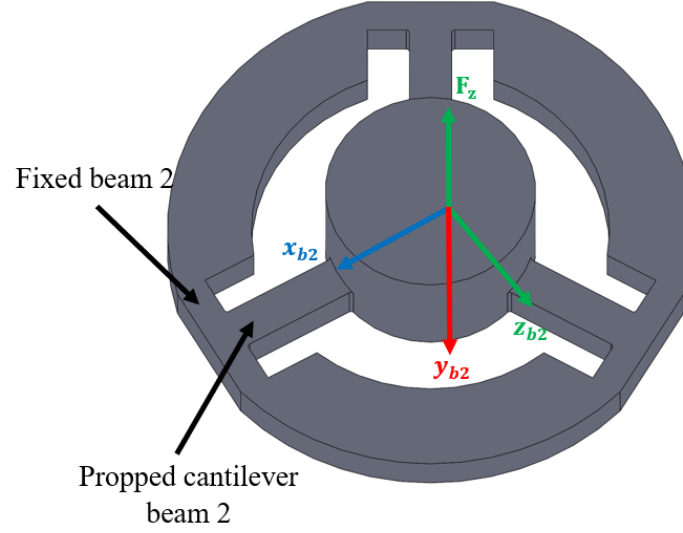
Figure 2.7: Propped cantilever beam 2 under the shear force F_z

For the propped cantilever beam 3, the analysis is done considering the sensor's axes. The shear force F_x will create a torsion and the shear force F_z will create a bending moment.

2.2.2 Effect of Dimension of the Beam on Displacement of the Central Solid Cylinder

For the propped cantilever beam 1, the shear force components towards x_{b1} will create a bending moment in the propped cantilever beam 1. For the propped cantilever beam 2, the shear force components towards x_{b2} will create a bending moment in the propped cantilever beam 2. Similarly, for the propped cantilever beam 3, the shear force components towards x_{b3} will create a bending moment in the propped cantilever beam 3.

The maximum deflection $\delta_{pb.max}$ of the propped cantilever beams due to the bending moment can be expressed as

$$\delta_{\text{pb.max}} = \frac{ML^2}{2EI}$$ (2.1)

Here,

M = bending moment which can be expressed as

for beam 1, $M = (0.87F_x - 0.5F_z)\, r$ (2.2)

for beam 2, $M = (-0.87F_x - 0.5F_z)\, r$ (2.3)

for beam 3, $M = (F_z)\, r$ (2.4)

where,

r = the perpendicular distance between the line of action of force and the axis of rotation. This is the distance between the top surface of the central solid cylinder and the position where the propped cantilever beam connects with the central solid cylinder.

L = length of the propped cantilever beam

E = modulus of elasticity (N/mm^2)

I = moment of inertia of the cross section of the beam which can be expressed as

$$I = \frac{BH^3}{12}$$ (2.5)

where,

B = width of the propped cantilever beam

H = height of the propped cantilever beam

And, the maximum bending stress of the propped cantilever beam $\sigma_{pb1.max}$ can be expressed as

$$\sigma_{pb.max} = \frac{Mc}{I}$$
(2.6)

Here,

c = the distance of the extreme surface from the centroid which can be expressed as

$$c = \frac{H}{2}$$
(2.7)
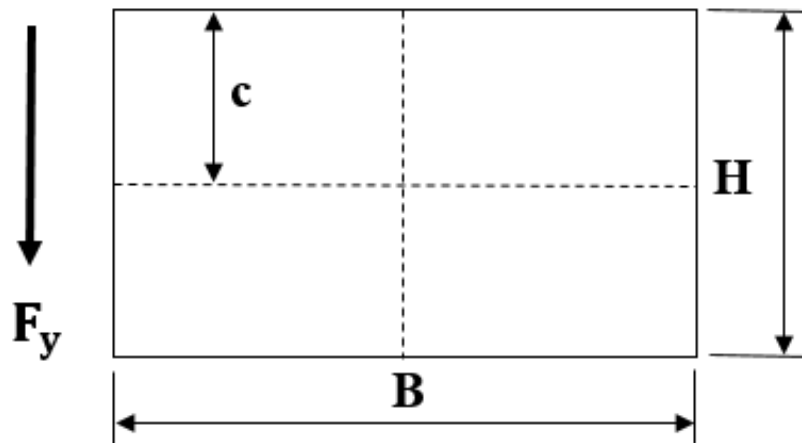
Figure 2.8: Cross-section of the propped cantilever beam

From eqn. (2.1), (2.6), and (2.7), the ratio of maximum deflection and the maximum bending stress can be expressed as

$$\frac{\delta_{pb.max}}{\sigma_{pb.max}} = \frac{L^2}{EH}$$

(2.8)

The shear force components towards z_{b1}, z_{b2}, and z_{b3} will create torsion in their respective beams. The angle of twist θ can be expressed as

$$\theta = \frac{\tau L}{\beta BH^3 G}$$

(2.9)

Here,

τ = torque which can be expressed as

for beam 1, $\qquad \tau = (0.5F_x + 0.87F_z)\, r$ (2.10)

for beam 2, $\qquad \tau = (0.5F_x - 0.87F_z)\, r$ (2.11)

for beam 3, $\qquad \tau = (F_x)\, r$ (2.12)

β = constant which can be found from Table 2.1

G = shear modulus of elasticity (N/mm^2)

Table 2.1: Constants for equation

b/t	1.00	1.50	1.75	2.00	2.50	3.00	4	6	8	10	∞
α	0.20	0.23	0.23	0.24	0.25	0.26	0.28	0.29	0.307	0.313	0.333
β	0.14	0.19	0.214	0.229	0.249	0.263	0.281	0.299	0.307	0.313	0.333

The maximum stress is induced at the center of the long side and is given by

$$\sigma_{max} = \frac{\tau}{\alpha BH^2} \qquad (2.13)$$

From eqn. (2.9) and (2.13), the ratio of angle of twist and maximum stress can be expressed as

$$\frac{\theta}{\sigma_{max}} = \frac{\alpha L}{\beta GH} \qquad (2.14)$$

From the previous section, under the normal force F_y, the scenario is similar to cantilever beam – single load at the End. For a single beam, if the normal force is $F_y/3$,

then the maximum deflection δ_{ymax} of a cantilever beam occurs at the end of the

cantilever beam and can be expressed as,

$$\delta_{ymax} = \frac{F_y L^3}{9EI} \qquad (2.15)$$

The maximum stress induced in a cantilever beam is at the fixed point and the maximum

stress can be calculated by

$$\sigma_{max} = \frac{cF_y L}{3I} \qquad (2.16)$$

So, eqn. (2.16)can be written as,

$$\sigma_{max} = \frac{HF_y L}{6I} \qquad (2.17)$$

From eqn. (2.15) and (2.17)

$$\frac{\delta_{ymax}}{\sigma_{max}} = \frac{2L^2}{3EH} \qquad (2.18)$$

2.2.2.1 Effect of Length of the Propped Cantilever Beam

For all the three propped cantilever beams have same deflection and stress under

the normal force F_y. From eqn.(2.18), if the height of the propped cantilever beam is

constant then the deflection is proportional to the square of length of the propped

cantilever beam.

$$\frac{\delta_{ymax}}{\sigma_{max}} \propto L^2 \qquad\qquad (2.19)$$

So, during the normal force F_y, if the length of the propped cantilever beam is

increased, the deflection is also increased compared to the stress induced in the propped

cantilever beam. From eqn. 2.5, the angle of twist of the propped cantilever beams is

proportional to the length of the beams. So, if the length of the propped cantilever beams

is increased, the central solid cylinder has more displacement.

For the shear forces, the propped cantilever beams experience twisting and

bending. From eqn.(2.14), if the width and height of the propped cantilever beams are

constant, then α and β are constant and the ratio between angle of twist and the maximum

stress is proportional to the length of the propped cantilever beam. So, when the shear

forces are applied, for a constant shear force, as the length of the propped cantilever beam

is increased, the angle of twist is increased compared to the maximum stress.

$$\frac{\theta}{\sigma_{max}} \propto L \qquad\qquad (2.20)$$

Also, from eqn. (2.8), for the bending moment due to the shear forces, the ratio

of maximum deflection and the maximum bending stress is proportional to the square of

the beam length when width and height are constant.

$$\frac{\delta_{pb.max}}{\sigma_{pb.max}} \propto L^2 \qquad\qquad (2.21)$$

So, for both the normal forces and the shear forces, the displacement of the ground electrode is increased as the length of the propped cantilever beam is increased.

2.2.2.1 Effect of Width and Height of the Propped Cantilever Beam

From eqn.(2.18), if the length of the beam is constant, then the ratio of maximum deflection and maximum stress is inversely proportional to the height of the propped cantilever beam. That means if the height of the propped cantilever beam is increased, the maximum deflection will be decreased compared to the maximum stress induced in the propped cantilever beam.

$$\frac{\delta_{ymax}}{\sigma_{max}} \propto \frac{1}{H} \qquad\qquad (2.22)$$

If the length of the propped cantilever beam is constant, then the ratio between angle of twist and maximum shear stress is inversely proportional to the height of the beam. The change of α and β are very small for the height change. So, the ratio can be expressed as

$$\frac{\theta}{\sigma_{max}} \propto \frac{1}{H} \qquad\qquad (2.23)$$

Similarly, for the bending moment due to the shear force, the ratio of maximum deflection and the maximum stress is inversely proportional to the beam height when length is constant.

$$\frac{\delta_{pb.max}}{\sigma_{pb.max}} \propto \frac{1}{H} \qquad\qquad (\ 2.24\ )$$

2.3 Measuring Element

The physical change of the elastic element will be converted into electrical signal by the measuring element. In this sensor, three parallel plate capacitors are used to convert the physical change into electrical signal and measure the three components of the applied forces. These three parallel plate capacitors will have a common ground electrode and three separate charged electrodes. These three separate charged electrodes will sit on a plane and connected with the bottom plate. As the bottom plate does not move under applied force, these three electrodes will not move under any applied force. On the other hand, the ground electrode is attached to the elastic element. And, as the elastic element moves under applied force, the ground electrode also moves. Thus, the distance between the ground electrode and the charged electrode plates are changed, and the capacitance of these capacitors are also changed. Figure 2.9 shows the CAD model of the measuring element, and the displacement of the ground electrode under each of three directional forces.

According to the theoretical analysis in section 2.2, when the shear force is applied in x-axis direction, the ground electrode will have translational displacement in x-axis and rotational displacement along z-axis. From Fig. 2.9 (b), the distance between the

electrodes for capacitor two is decreased so that its capacitance is increased, the distance

between the electrodes for capacitor three is increased so that its capacitance is decreased,

and the distance between the electrodes for capacitor one has small change so that its

capacitance is not changed significantly. From the section 2.2, under the normal force

along y-axis, the ground electrode will have translational movement only along y-axis. It

will not move in any other directions and it will not have any rotational movement. So,

from Fig. 2.9 (c). under the normal force towards positive y-axis, the distance between

electrodes for all three capacitors will be decreased so that the capacitance of all the three

capacitors' will be increased. Also, for the shear force along z-axis, the ground electrode

will have translation displacement along z-axis and rotation along x-axis. So, from Fig.

2.9 (d), for the shear force in the positive z-axis direction, the distance between the

electrodes for capacitor 1 will decrease so that its capacitance will increase, and the

distance between the electrodes for capacitor 2 and 3 will increase so that the capacitance

of capacitor two and three will decrease.
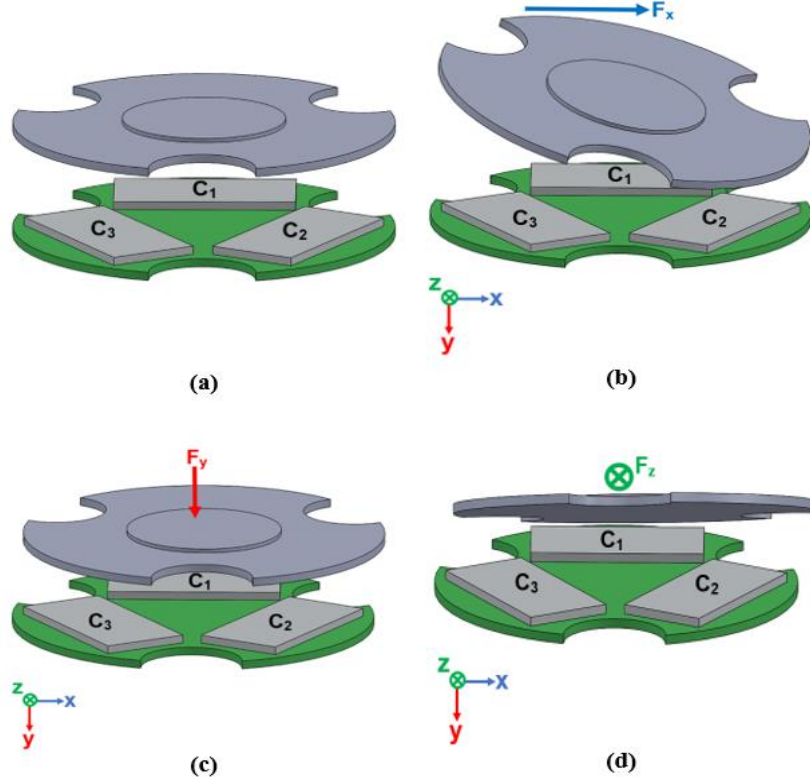
Figure 2.9: Measuring element under (a) zero force condition, (b) shear force, F_x, (c) normal force, F_y, and (d) shear force, F_z

2.4 Calibration Matrix

The capacitance changes in three capacitors can be expressed in terms of applied force. Assuming the relationship between applied force and capacitance change as linear, when the shear force F_x is applied, the capacitance change in capacitor 1,2, and 3 can be expressed as $\Delta c_{1x} F_x$, $\Delta c_{2x} F_x$, and $\Delta c_{3x} F_x$, respectively. Here, Δc_{1x} Δc_{2x}, and Δc_{3x} are the coefficient of capacitance changes of capacitor 1, 2, and 3 under F_x. Similarly, the capacitance changes in three capacitors due to F_y can be expressed as $\Delta c_{1y} F_y$, $\Delta c_{2y} F_y$, and $\Delta c_{3y} F_y$. And the capacitance changes in three capacitors due to F_z can be expressed as $\Delta c_{1z} F_z$, $\Delta c_{2z} F_z$, and $\Delta c_{3z} F_z$.

So, the total capacitance changes in capacitor 1,2, and 3 for all three directional forces can be expressed as

$$\Delta C_1 = \Delta c_{1x} F_x + \Delta c_{1y} F_y + \Delta c_{1z} F_z \qquad (2.25)$$

$$\Delta C_2 = \Delta c_{2x} F_x + \Delta c_{2y} F_y + \Delta c_{2z} F_z \qquad (2.26)$$

$$\Delta C_3 = \Delta c_{3x} F_x + \Delta c_{3y} F_y + \Delta c_{3z} F_z \qquad (2.27)$$

Equation (2.25), (2.26), and (2.27) can be expressed as

$$\begin{bmatrix} \Delta C_1 \\ \Delta C_2 \\ \Delta C_3 \end{bmatrix} = \begin{bmatrix} \Delta c_{1x} & \Delta c_{1y} & \Delta c_{1z} \\ \Delta c_{2x} & \Delta c_{2y} & \Delta c_{2z} \\ \Delta c_{3x} & \Delta c_{3y} & \Delta c_{3z} \end{bmatrix} \begin{bmatrix} F_x \\ F_y \\ F_z \end{bmatrix}$$

or,
$$\overrightarrow{\Delta c} = \mathbf{C}.\vec{f} \qquad (2.28)$$

or,
$$\vec{f} = \mathbf{C}^{-1}.\overrightarrow{\Delta c} \qquad (2.29)$$

Here, **C** is the calibration matrix. If we know the calibration matrix, the from the capacitance change data, the applied force can be measured.

Linear least-squares method can be used to find the calibration matrix. To find the calibration matrix, forces will be only applied in one direction at the time. First, when the forces are only applied in x – direction only, then F_y and F_z will be zero. So, eqn. (2.25), (2.26), and (2.27) will be

$$\Delta C_1 = \Delta c_{1x} F_x \qquad (2.30)$$

$$\Delta C_2 = \Delta c_{2x} F_x \qquad (2.31)$$

$$\Delta C_3 = \Delta c_{3x} F_x \qquad\qquad (2.32)$$

Using the linear least-squares method, from the capacitance changes and forces Δc_{1x}, Δc_{2x}, and Δc_{3x} can be found. Similarly, when forces are only applied in $y-$ direction, then F_x and F_z will be zero and Δc_{1y}, Δc_{2y}, and Δc_{3y} can be found. Again, by applying forces in $z-$ axis only, Δc_{1z}, Δc_{2z}, and Δc_{3z} can be found.

CHAPTER 3

COMPUTATIONAL ANALYSIS

COMSOL Multiphysics® modeling software was used to do both structural analysis and capacitance analysis. First, the structural analyses were done to see the effect of different dimension change of the elastic element on the displacement of the ground electrode under different forces. Then capacitance analyses were done to see the whether the theoretical analyses were correct. Then combined structural and computational analyses were done to design the sensor.

3.1 Structural Analyses:

The design of elastic element is divided into two types. In type 1, the propped cantilever beams are thicker than the fixed beam and the type 2 is opposite of type 1. That means, in type 2, the fixed beams are thicker than the propped cantilever beams.

3.1.1 Displacement Behavior for Type 1 and Type 2

The type 1 and type 2 have equal size of hollow cylinder. The difference between type 1 and type 2 is in the size of propped cantilever beams and fixed beams. Figure 3.1 shows the CAD model of a propped cantilever beam and a fixed beam. In type 1, the propped cantilever beams are thick, and the fixed beams are thin. The thick propped cantilever beams have a length of 12 mm, width of 3 mm, and height of 4 mm. the thin fixed beams have equal length and height, but the width is 1 mm.
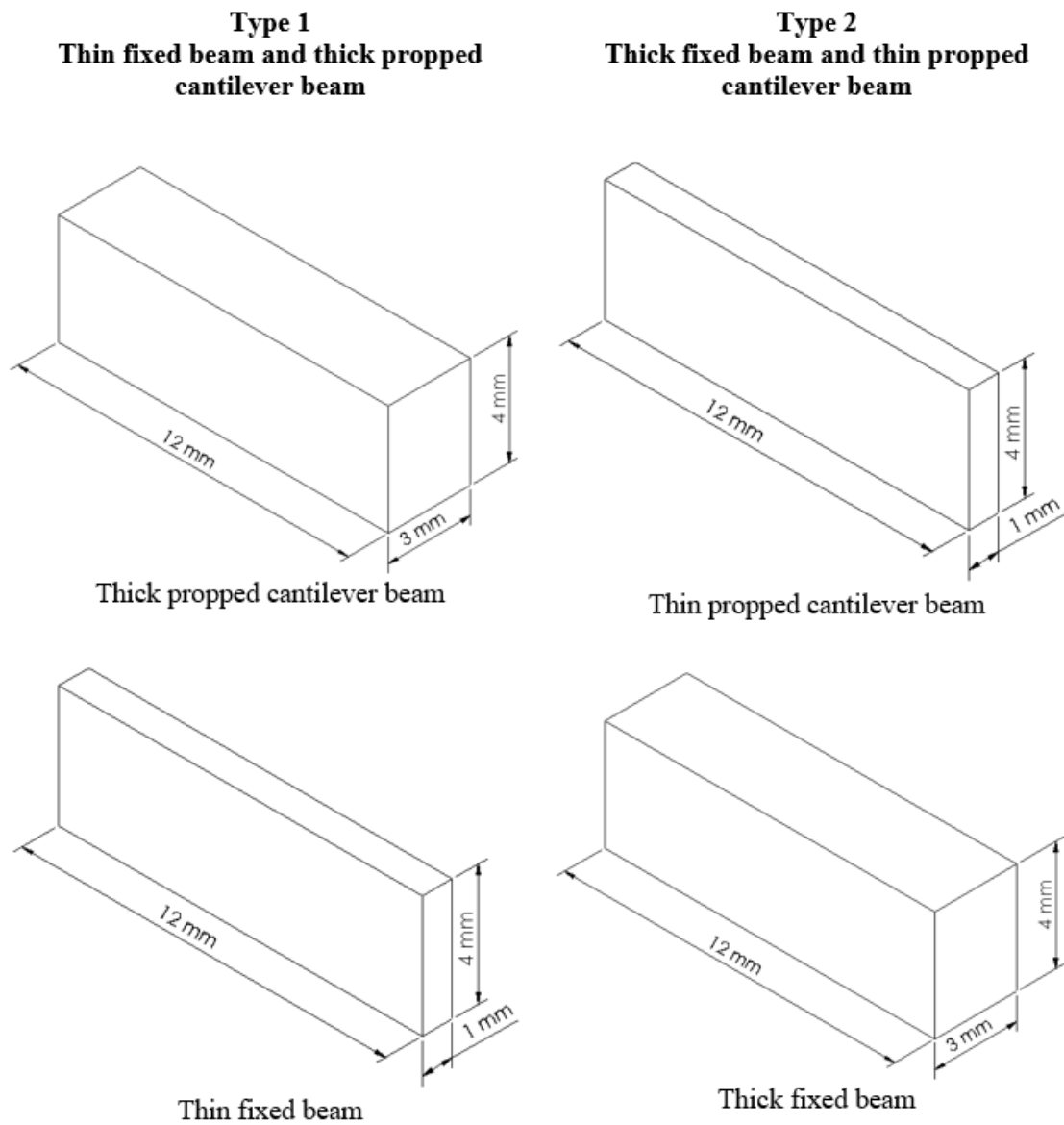
Figure 3.1: CAD model of the propped cantilever beam and fixed beam for type 1 and

type 2 with dimensions

The type 2 is opposite of type 1. In type 2, the propped cantilever beams are thin, and the fixed beams are thick. The dimensions of the fixed beams of type 2 are same as propped cantilever beams of type 1, and the dimensions of the propped cantilever beams of type 2 are same as fixed beams of type 1, but the beam is placed horizontally. So, this time the width of the propped cantilever beam is 4 mm, and height is 1 mm.

Figure 3.2, 3.3, and 3.4 show the displacement variation of the ground electrode and Fig. 3.5 shows the stress distribution induced in the elastic element for type 1 and type 2 design. For the shear force $F_x = 100$ N, the ground electrode has x-axis displacement in positive x-axis direction for type 1 (Fig. 3.2 a) and in negative x-axis direction for type 2 (Fig. 3.2 b). The displacement is 0.01 mm for type 1 and -0.04 mm for type 2. So, the magnitude of displacement is higher in type 2 than type 1. For both type 1 and type 2, the positive x-axis side of the ground electrode has displacement in negative y-axis direction and the negative x-axis side has displacement in positive y-axis direction. That means the ground electrode has a rotational displacement around z-axis. At the edges of the ground electrode in x-axis direction, the magnitude of the displacement is 0.02 mm for type 1 (Fig. 3.2 c) and 0.2 mm for type 2 (Fig. 3.2 d). So, the ground electrode has more rotational displacement for type 2 than type 1. For both types, the ground electrode does not have significant displacement in z-axis direction (Fig. 3.2 e and Fig. 3.2 f). The maximum stress induced in type 2 beam is 1.6 times of the stress induced in type 1 beam. But the rotational displacement in type 2 is 10 times of the type 1. So, with the type 2, more rotational displacement can be obtained for same stress.
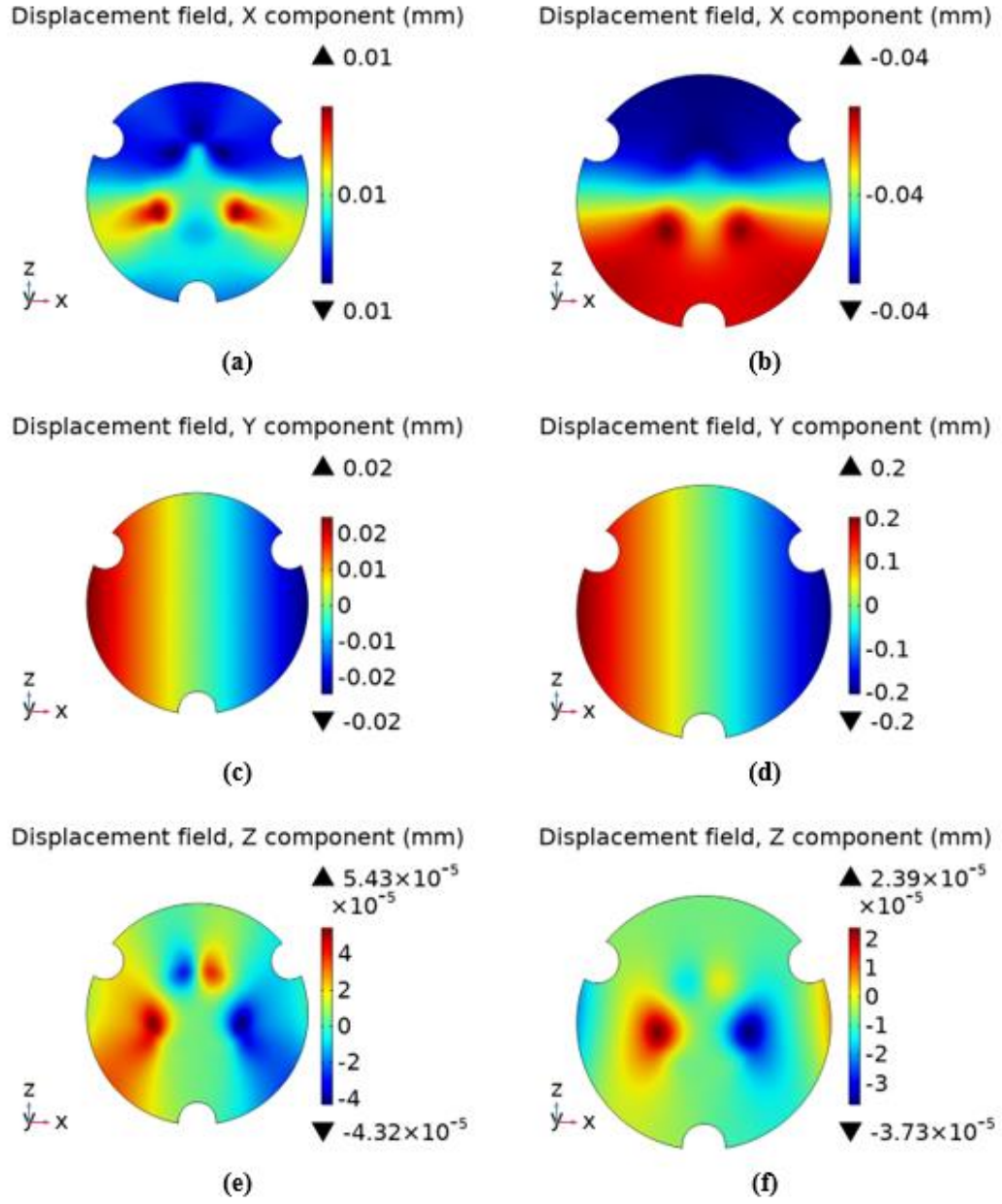
Figure 3.2: Displacement of the ground electrode under $F_x = 100\text{N}$ force (a) x-axis Type 1, (b) x-axis Type 2, (c) y-axis Type 1, (d) y-axis Type 2, (e) z-axis Type 1, and (f) z-axis Type 2
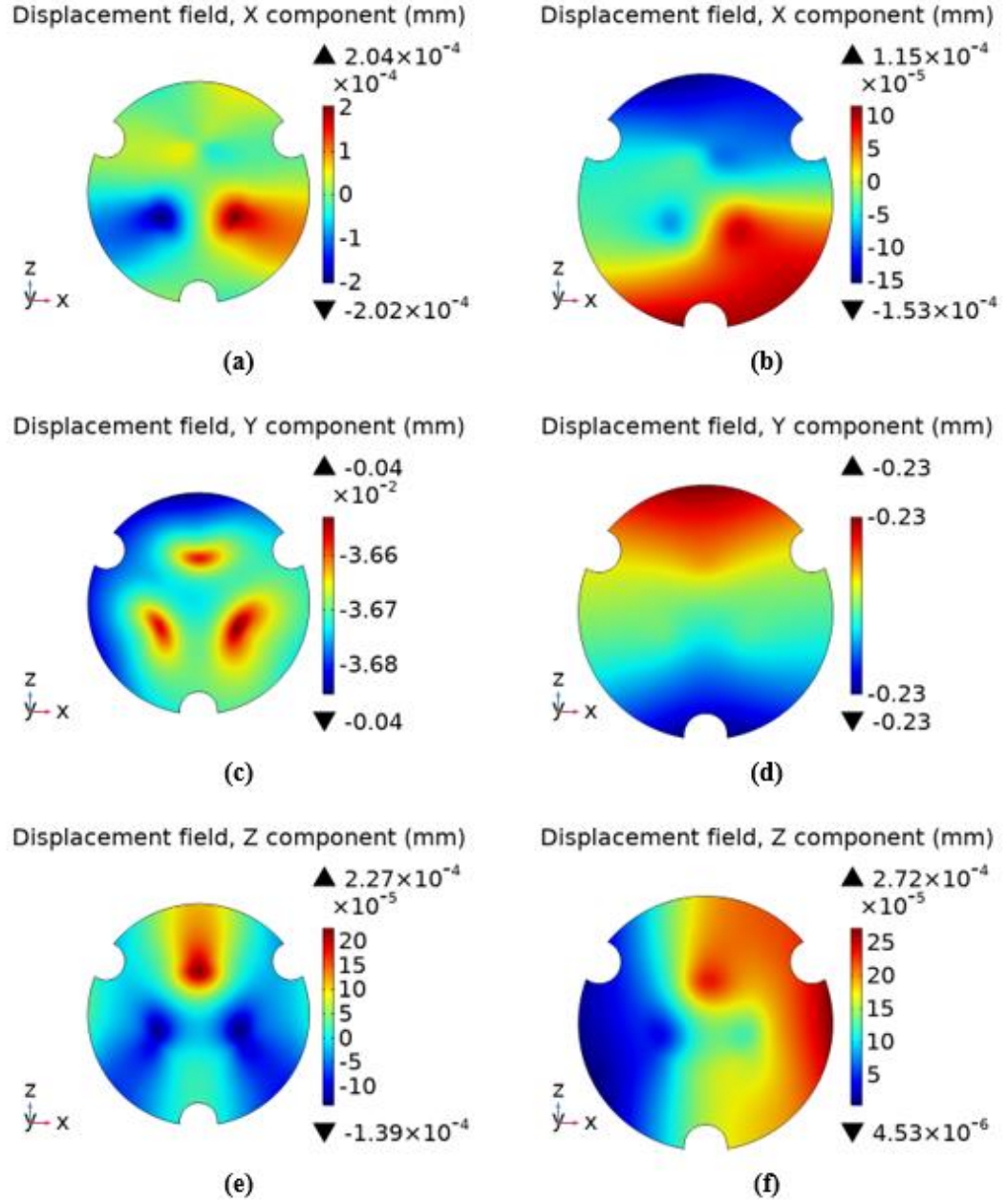
Figure 3.3: Displacement of the ground electrode under F_y = -100N force (a) x-axis Type 1, (b) x-axis Type 2, (c) y-axis Type 1, (d) y-axis Type 2, (e) z-axis Type 1, and (f) z-axis Type 2
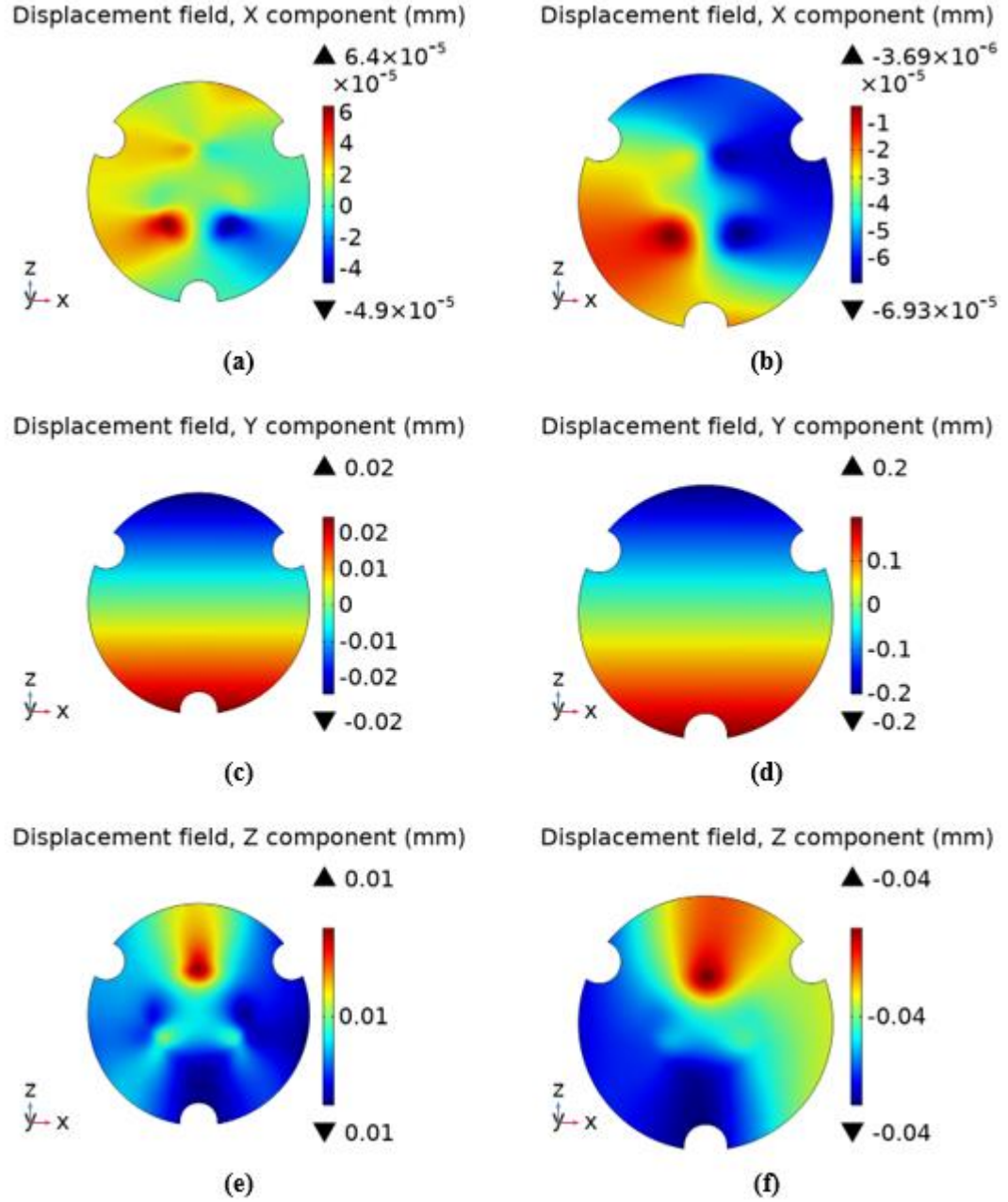
Figure 3.4: Displacement of the ground electrode under $F_z = 100N$ force (a) x-axis Type 1, (b) x-axis Type 2, (c) y-axis Type 1, (d) y-axis Type 2, (e) z-axis Type 1, and (f) z-axis Type 2
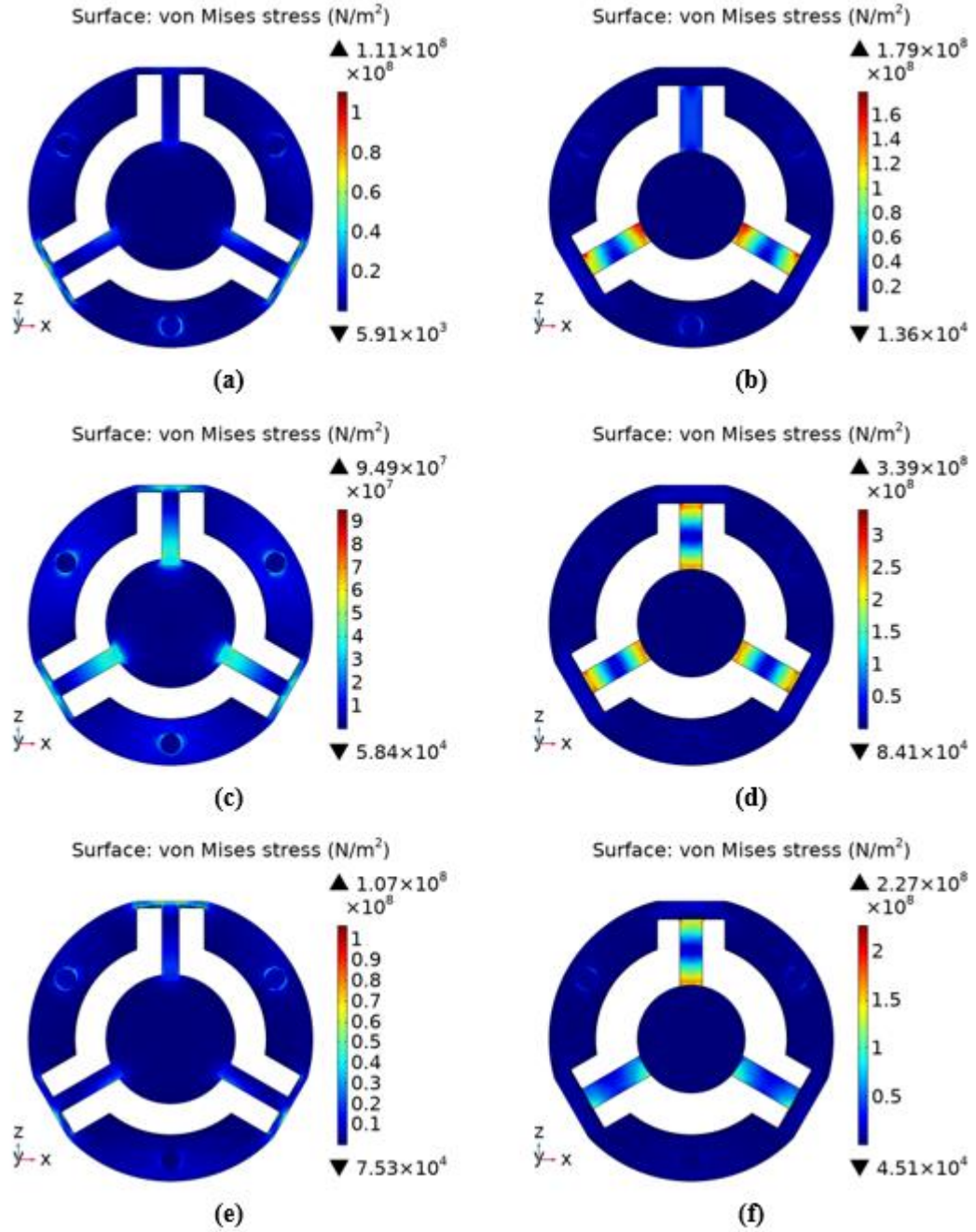
Figure 3.5: Stress distribution for type 1 and type 2 beam (a) F_x = 100N type 1, (b) F_x = 100N type 2, (c) F_y = - 100N type 1, (d) F_y = - 100N type 2, (e) F_z = 100N type 1, and (f) F_z = 100N type 2

So, under the normal force F_y, for both type 1 and type 2, the ground electrode has significant displacement in only y-axis direction. The ground electrode experiences more displacement for type 2 than type 1. There is a slight variation in the displacement, but the variation is too small. So, the displacement can be considered as symmetric. Under the shear force F_x and F_z, the ground electrode has more displacement along x-axis and z-axis respectively for type 2 than type 1 but for type 1 the displacement is in positive direction and for type 2 is in negative direction. For both types, the ground electrode has rotational displacement under the shear forces. The rotational displacement is along z-axis for the shear force F_x and is along x-axis for the shear force F_z. The magnitude of rotational displacement is higher in type 2. The ground electrode has no significant displacement along the perpendicular direction on the same plane under the shear forces.

3.1.2 Displacement Behavior for Type 2.1, 2.2, and 2.3 Beam

In section 3.1.1, it is seen that the ground electrode has more displacement for type 2 beam, which is the thin propped cantilever beam and thick fixed beam design. In this section, simulations were done to see the effects of the width and height of the propped cantilever beams on the displacement behavior of the ground electrode for the same cross-sectional area of the propped cantilever beams. The simulations were done for 4 mm^2 of cross-sectional area of the propped cantilever beams. That means the product of width and height is 4 mm^2. For analyzing the displacement behavior, three designs have been analyzed. Figure 3.6 shows the dimensions of these three designs.

In type 2.1, the width of the propped cantilever beam is 1 mm, and height is 4 mm. The type 2.3 has opposite dimensions. Its width is 4 mm, and height is 1 mm. The type 2.2 has equal width and height of 2 mm. So, the propped cantilever beams in type
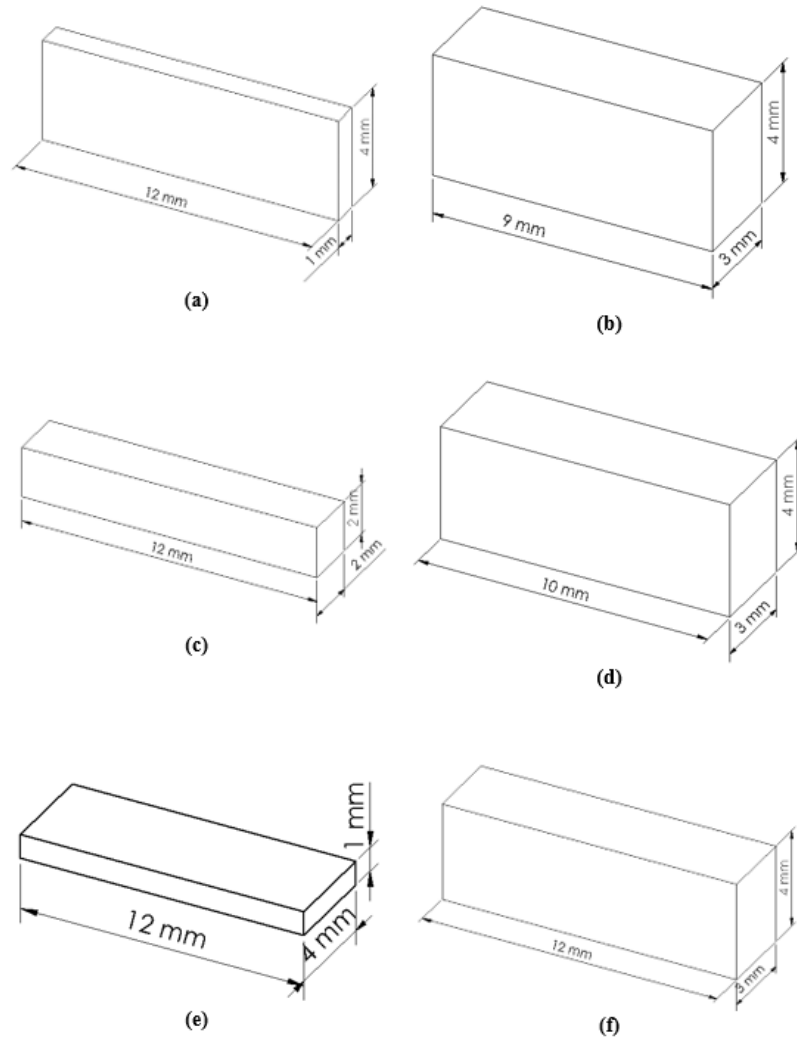
Figure 3.6: Dimensions of the propped cantilever beam and fixed beam (a) propped cantilever beam type 2.1, (b) fixed beam type 2.1, (c) propped cantilever beam type 2.2, (d) fixed beam type 2.2, (e) propped cantilever beam type 2.1, and (f) fixed beam type 2.1

2.1 and 2.3 is rectangular in shape and type 2.2 is square. The length of the propped cantilever beams is same for all the three types. The width and height of the fixed beams are also same in all three types, but the length is different. The width varies in these three types of propped cantilever beams, and 4 mm gap is maintained (Fig. 3.7) in each side between the hollow cylinder and the propped cantilever beams. So, in type 2.1 the length is 1+4+4 = 9 mm, in type 2.2 the length is 2+4+4 = 10 mm, and in type 2.3, the length is 4+4+4 = 12 mm.
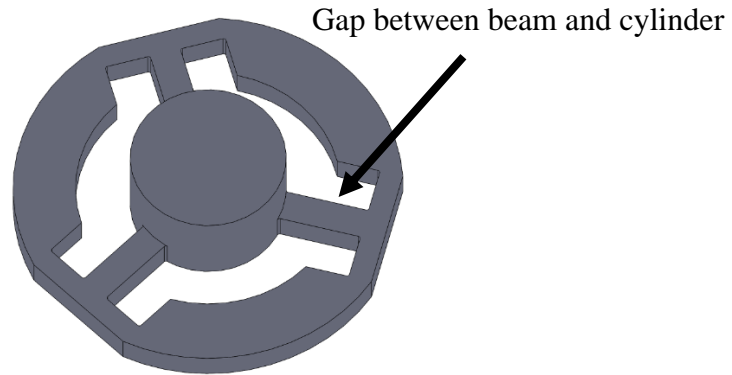
Figure 3.7: Gap between the propped cantilever beam and the hollow cylinder

3.1.2.1 Comparison between Type 2.1 and Type 2.2

Under the shear force F_x, the stress induced in type 2.2 is 1.4 times than type 2.1 (Fig. 3.8 k and j). But the rotational displacement of the ground electrode for type 2.2 is 0.11 mm (Fig. 3.8 e), and for type 2.1 is 0.05 mm (Fig. 3.8 d). So, the rotational displacement in type 2.2 is 2 times of rotational displacement of type 2.1. Also, the displacement in the x – axis direction for type 2.2 is -0.02 mm (Fig. 3.8 b), and negligible displacement in x – axis direction for type 2.1 (Fig. 3.8 a). For both the type, the ground

electrode does not have any significant displacement in z – direction for the shear force F_x. So, with the type 2.2, the ground electrode experiences more displacement for equal stress in the elastic element.

Under the normal force F_y, the stress induced in type 2.2 is 2 times than type 2.1 (Fig. 3.9 k and j), and the displacement of the ground electrode in y-direction is more than 2 times for type 2.2 than type 2.1. The displacement of ground electrode for type 2.1 is – 0.03 mm (Fig. 3.9 d), and for type 2.2 is – 0.07 mm (Fig. 3.9). The ground electrode does not have any significant displacement in x – axis and z – axis direction for both types.

Figure 3.10 j and k show the stress distribution in the elastic element under the shear force F_z. The stress induced in type 2.2 is 1.3 times of type 2. But the rotational displacement of ground electrode for type 2.2 is more than 2 times of type 2.1. Maximum displacement of the ground electrode for type 2.1 is 0.05mm (Fig. 3.10 d), and for type 2.2 is 0.1 mm (Fig. 3.10 e). The ground electrode does not have any significant displacement in x – axis direction for the shear force F_z.

So, type 2.2 has more displacement than type 2.1 for all force component.

3.1.2.2 Comparison between Type 2.2 and Type 2.3

Under the shear force F_x, the stress induced in type 2.2 is close to type 2.3 (Fig. 3.8 k and l). But the rotational displacement of the ground electrode for type 2.3 is 0.27 mm which is 2.5 times of rotational displacement of type 2.2 (Fig. 3.8 e and f). Also, the displacement in x – axis direction for type 2.3 is 0.06 mm (Fig. 3.2 c). So, the ground electrode has 3 times displacement in the x – axis direction for type 2.3 than type 2.2. The

ground electrode does not have any significant displacement in z – axis direction for the shear force F_x. So, the ground electrode has more displacement for type 2.3.

Under the normal force F_y, the stress induced in type 2.3 is 1.15 times than type 2.2 (Fig. 3.9 k and l), but the displacement of the ground electrode in y – direction for type 2.3 is – 0.2 mm (Fig. 3.9 f) which is almost 3 times of the displacement for type 2.2. The ground electrode has no significant displacement in x – and z – direction for the normal force.

Under the shear force F_z, the stress induced in type 2.2 is close to type 2.3 (Fig. 3.10 k and l). But the rotational displacement of ground electrode for type 2.3 is 0.27 mm (Fig. 3.10 i) which is 2.7 times of the displacement of type 2.2. Similar to the shear force F_x, the ground electrode moves 3 times with the type 2.3 than 2.2 to the shear force direction during the shear force F_z (Fig. 3.10 i). Also, for both types, the ground electrode does not have any significant displacement in x – direction for the shear force F_z. So, type 2.3 has more displacement than type 2.2 for all force component.
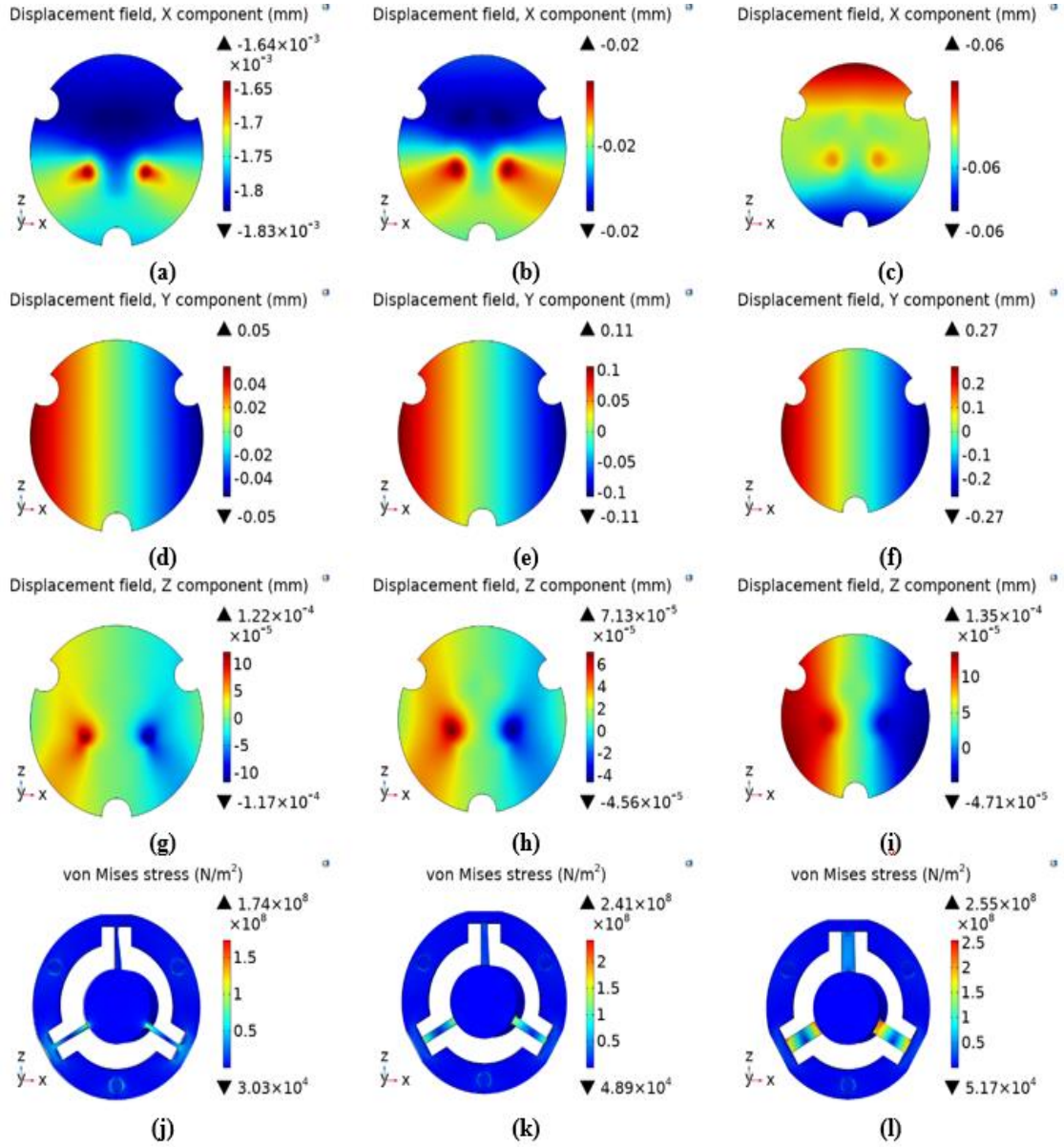
Figure 3.8: Displacement of the ground electrode and the stress distribution in the elastic element for type 2.1, 2.2, and 2.3 under the shear force $F_x = 100N$ (a)-(c) x – axis displacement for type 2.1, 2.2, and 2.3, respectively. (d)-(f) y – axis displacement for type 2.1, 2.2, and 2.3, respectively. (g)-(i) z – axis displacement for type 2.1, 2.2, and 2.3, respectively. Stress distribution for type (j) 2.1, (k) 2.2, and (l) 2.3
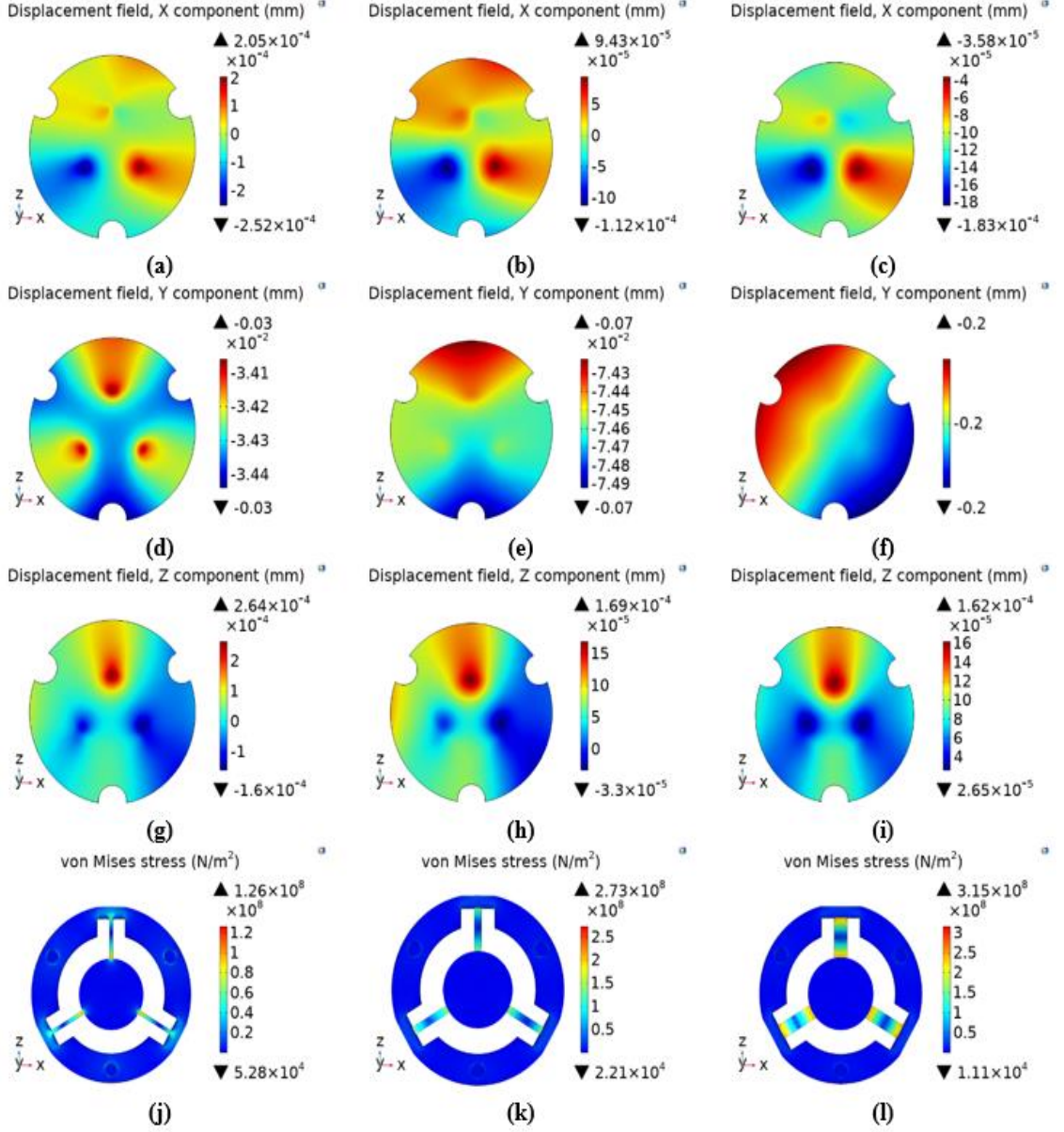
Figure 3.9: Displacement of the ground electrode and the stress distribution in the elastic element for type 2.1, 2.2, and 2.3 under the normal force $F_y = -100N$ (a)-(c) x – axis displacement for type 2.1, 2.2, and 2.3, respectively. (d)-(f) y – axis displacement for type 2.1, 2.2, and 2.3, respectively. (g)-(i) z – axis displacement for type 2.1, 2.2, and 2.3, respectively. Stress distribution for type (j) 2.1, (k) 2.2, and (l) 2.3
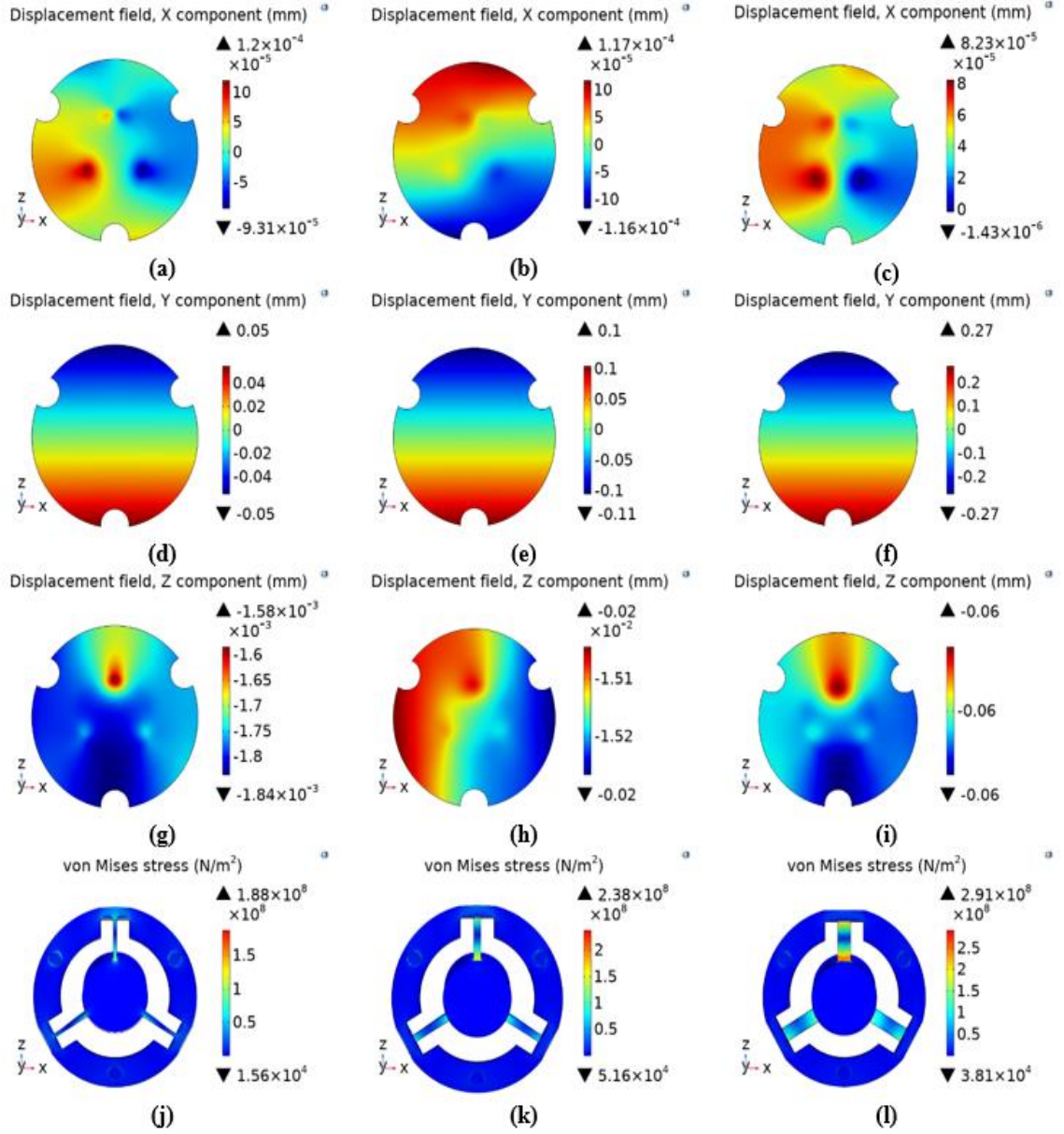
Figure 3.10: Displacement of the ground electrode and the stress distribution in the elastic element for type 2.1, 2.2, and 2.3 under the shear force $F_z = 100N$ (a)-(c) x – axis displacement for type 2.1, 2.2, and 2.3, respectively. (d)-(f) y – axis displacement for type 2.1, 2.2, and 2.3, respectively. (g)-(i) z – axis displacement for type 2.1, 2.2, and 2.3, respectively. Stress distribution for type (j) 2.1, (k) 2.2, and (l) 2.3

So, considering the stress distribution in the elastic element and displacement of the ground electrodes, among the three types, type 2.3 has more displacement for all force components than type 2.1 and type 2.2. Thus, for constant cross-sectional area of the propped cantilever beam, if the ratio of the width and height increases, the ground electrode has more displacement.

3.1.3 Effect of Length of the Propped Cantilever Beam

The effect of length of the propped cantilever beam on the displacement of the ground electrode is observed by doing simulation for two different length of the propped cantilever beam. Figure 3.11, 3.12, and 3.13 show the displacement behavior of the ground electrode, and Fig. 3.14 shows the stress distribution on the elastic element for longer and shorter propped cantilever beam for all three component of forces (Normal force F_y, and Shear force F_x and F_z).

From Fig. 3.14 (a), and (b), the maximum stress on the elastic element for longer propped cantilever beam is 23% higher than the shorter beam. And the ground electrode has 0.07 mm displacement (Fig. 3.11 a) for longer beam and 0.02 mm displacement (Fig. 3.11 b) for shorter beam in the negative x-axis direction. That means, the displacement of the ground electrode for longer propped cantilever beam is 2.5 times or 250% higher than the shorter propped cantilever beam. So, as the length of the propped cantilever beam decreases, the displacement of the ground electrode in the negative x-axis direction decreases much comparatively to the stress reduction.
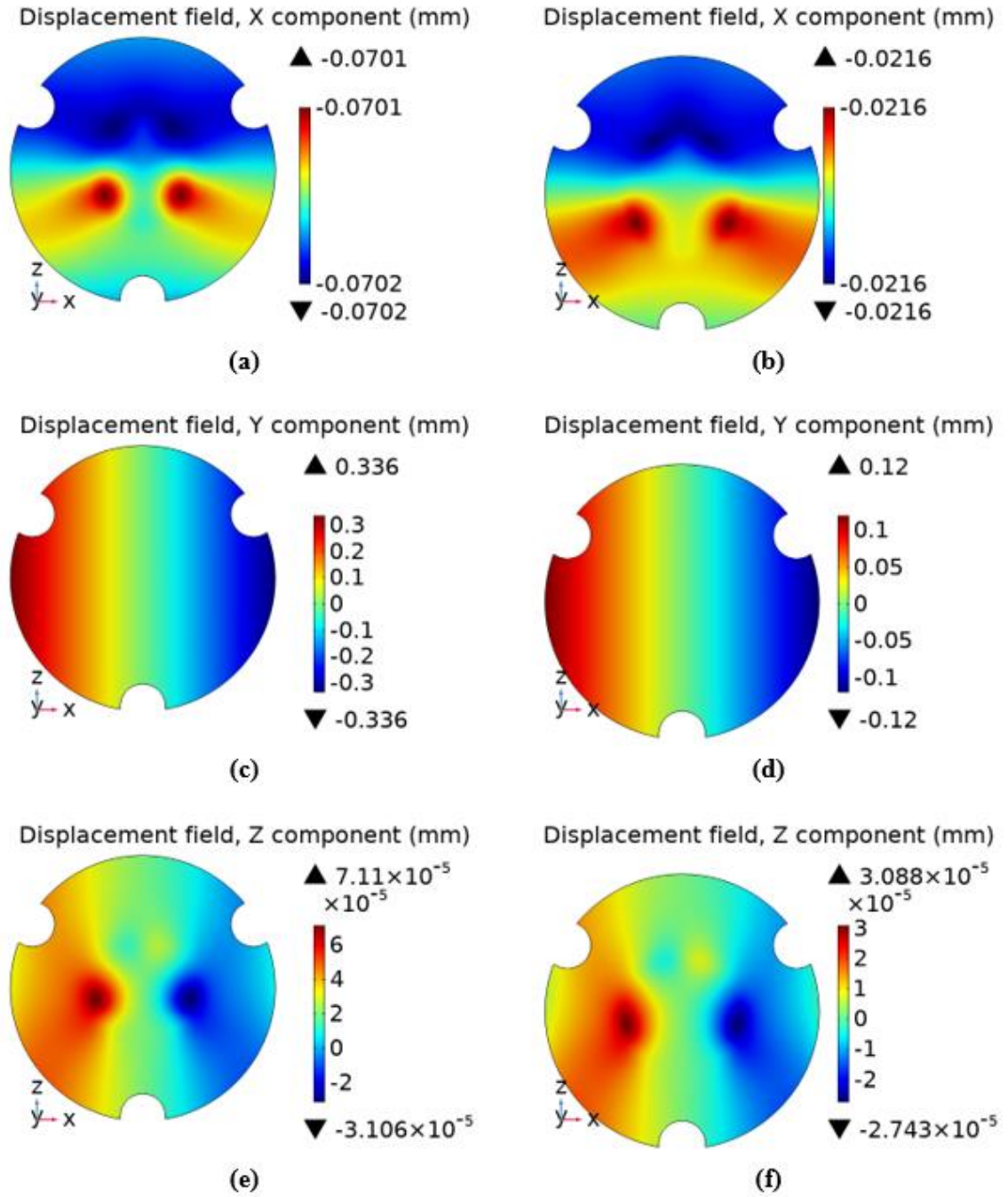
Figure 3.11: Variation of displacement of the ground electrode due to the length difference of propped cantilever beam for type 2 elastic element for the shear force $(F_x) = 100N$ (a), (c), and (e) for longer beam in x-axis, y-axis, and z-axis, respectively. (b), (d), and (f) for x-axis, y-axis, and z-axis respectively for shorter beam
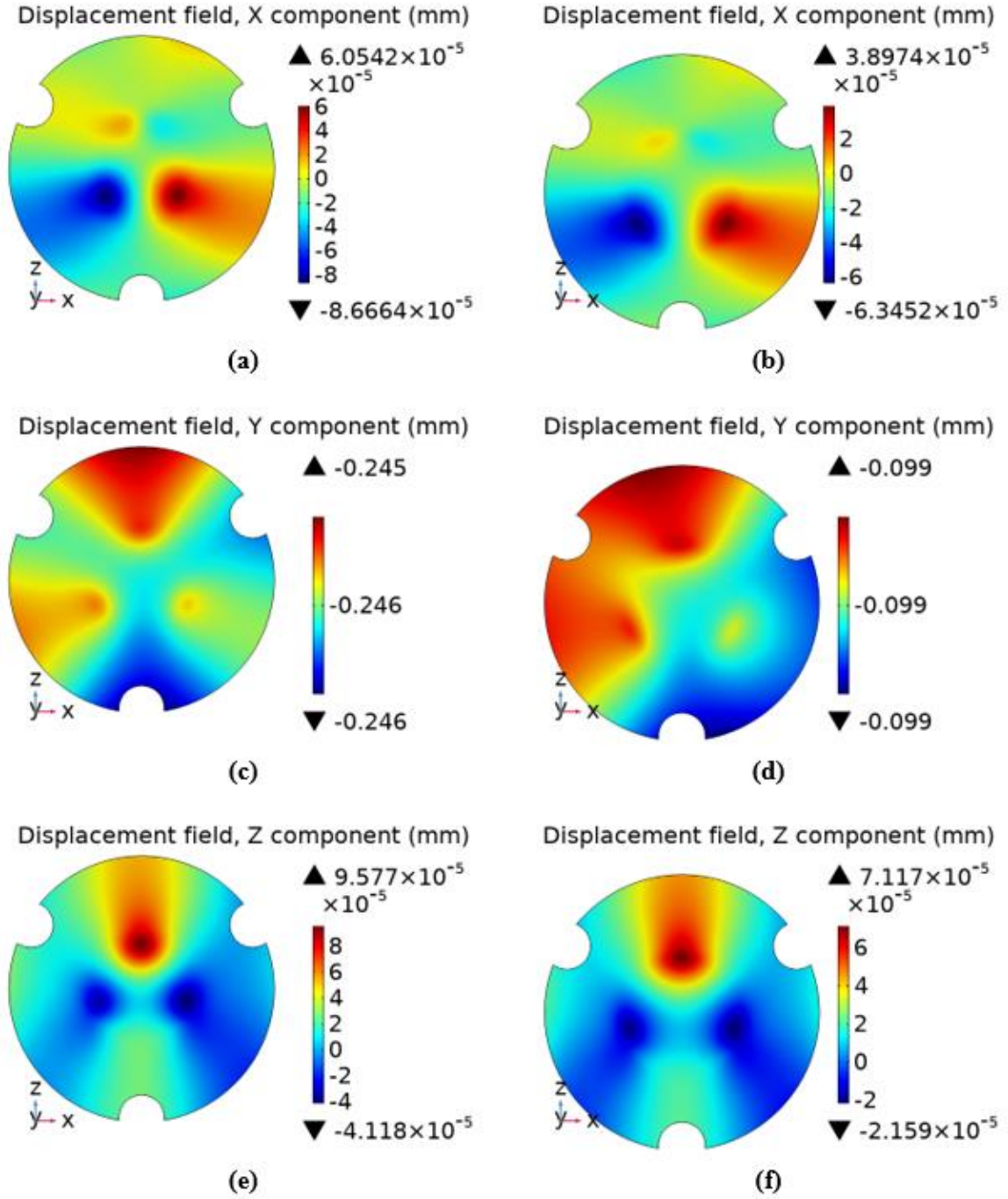
Figure 3.12: Variation of displacement of the ground electrode due to the length

difference of propped cantilever beam for type 2 elastic element for the normal force

$(F_y) = -100N$ (a), (c), and (e) for longer beam in x-axis, y-axis, and z-axis,

respectively. (b), (d), and (f) for x-axis, y-axis, and z-axis respectively for shorter beam
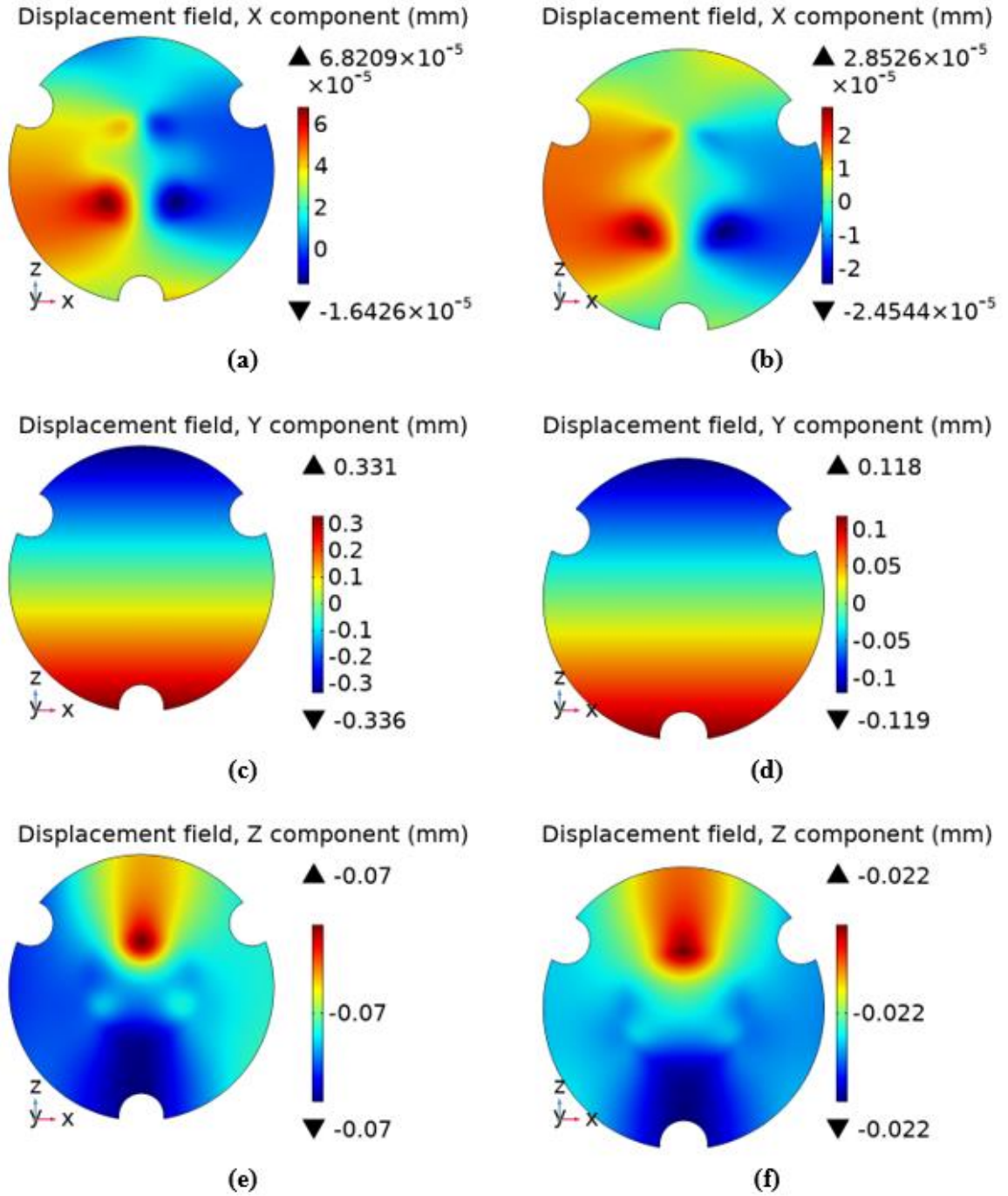
Figure 3.13: Variation of displacement of the ground electrode due to the length difference of propped cantilever beam for type 2 elastic element for the shear force $(F_z) = 100N$ (a), (c), and (e) for longer beam in x-axis, y-axis, and z-axis, respectively. (b), (d), and (f) for x-axis, y-axis, and z-axis, respectively for shorter beam
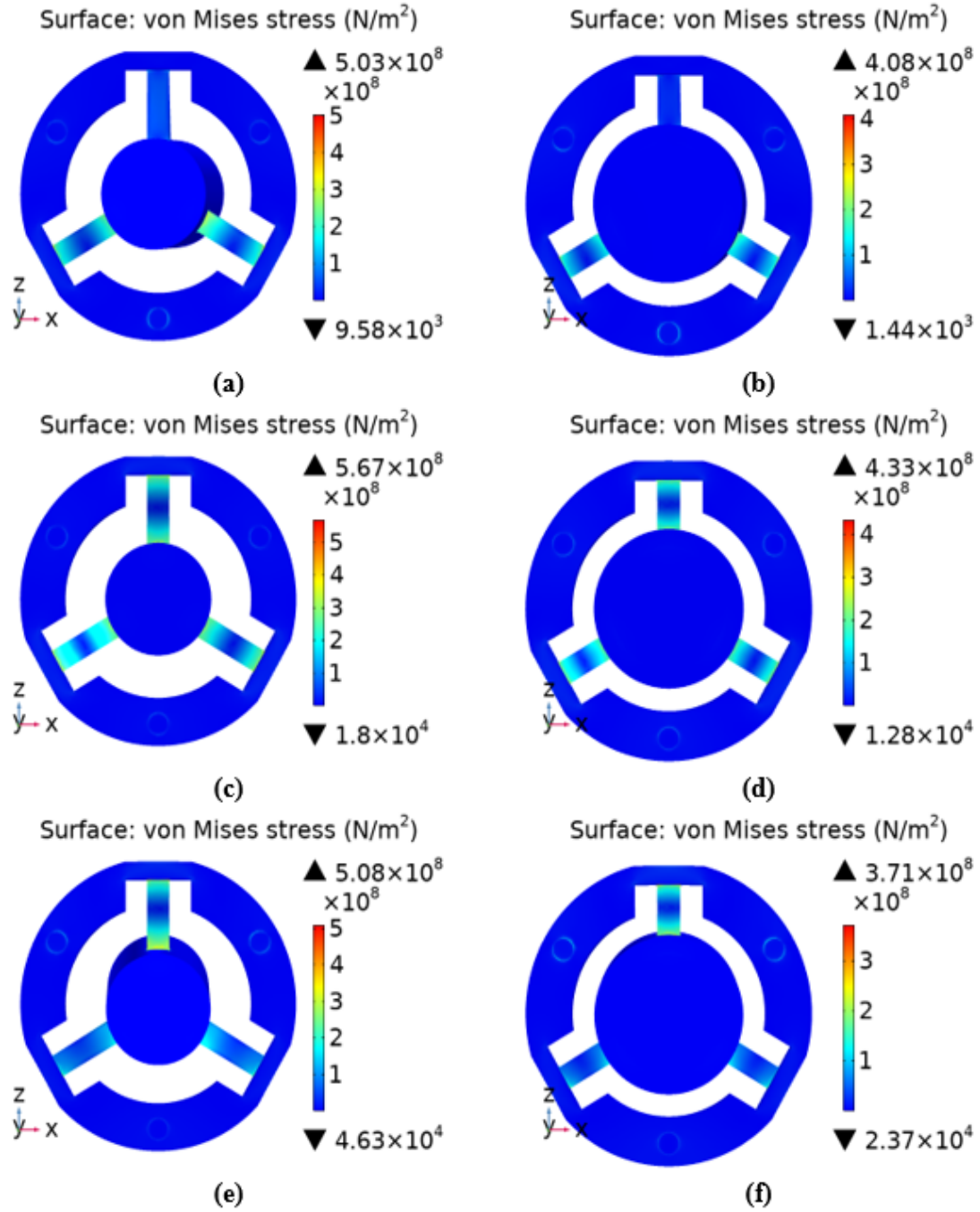
Figure 3.14: Stress distribution on the elastic element for longer and shorter propped cantilever beam. (a), (c), and (e) for longer beam for shear force F_x, normal force F_y, and shear force F_z, respectively (b), (d), and (f) for shorter beam for shear force F_x, normal force F_y, and shear force F_z, respectively

From Fig. 3.11(c), y-axis displacement is 0.336 mm for longer beam and from

Fig. 3.11 (d), y-axis displacement is 0.12 mm for shorter beam. So, the rotational

displacement of the ground electrode is 1.8 times or 180% higher for the longer beam

than the shorter beam. Thus, the rotational displacement increases much as the length of

the propped cantilever beam increases comparatively to the how much stress is induced

in the elastic element. For both the longer and shorter propped cantilever beam, no

significant displacement in the z-axis direction. So, comparatively to the stress increase

due to the increase in length of the propped cantilever beam, the displacement of the

ground electrode increases much for the increase in length.

From Fig. 3.14 (c) and (d), the maximum stress in the elastic element for longer

propped cantilever beam is 30% higher than the shorter propped cantilever beam. Figure

3.12 shows the difference of displacement of the ground electrode due to length change

of the propped cantilever beam for the normal force $F_y = -100N$. From Fig. 3.12 (c),

the y-axis displacement is – 0.245 mm for longer beam and from Fig. 3.12 (d), the y-axis

displacement is – 0.099 mm for shorter beam. So, the displacement in y-axis direction for

longer beam is 1.47 times higher or 147% higher than the shorter beam. Thus, the

displacement in y-axis increases much higher comparatively to the stress increment if the

length of the beam is increased.

From Fig. 3.14(e) and (f), the maximum stress in the elastic element is 37%

higher for the longer beam. Figure 3.13 shows the difference of displacement for the

shear force $F_z = 100N$. Figure 3.13 (e) and (f) show that the ground electrode has 0.07

mm displacement for longer beam and 0.02 mm displacement for shorter beam in the

negative z-axis direction. That means, the displacement is increased by 250% due to

increase in length of the propped cantilever beams. So, the ground electrode has less displacement in negative z-axis for the shorter propped cantilever beam. Also, Fig. 3.13 (c) and (d) show that the ground electrode has 180% increase in rotational displacement due to the increase in length. For both the longer and shorter beam, the ground electrode does not have any significant displacement in x-axis direction.

So, from the above discussion, the length of the cantilever beam has significant effect on the displacement of the ground electrode. As the length of the propped cantilever beam increases, the ground electrode has more displacement in the opposite of the shear force direction and more rotational displacement for the shear force. And, also for the normal force, the ground electrode has more displacement in the normal force direction if the length of the propped cantilever beam is increased.

3.2 Capacitance Analyses

To do the capacitance analyses, the whole sensor is modeled in the SolidWorks. Figure 3.15, shows the CAD model of the whole sensor with all the parts. Three parallel plate capacitors are made of one common ground electrode and three charged electrode plates. The three charged electrode plates are housed on a plate. The ground electrode is attached to the central solid cylinder of the elastic element and the charge electrode plate is attached to bottom plate. The elastic element sits on top of the bottom plate. The ground electrode does not have any connection with any fixed element. So, as the central solid cylinder moves under applied forces, the ground electrode also moves. Thus, the distances between the charged electrodes and the common ground electrode are changed and the capacitances are also changed.
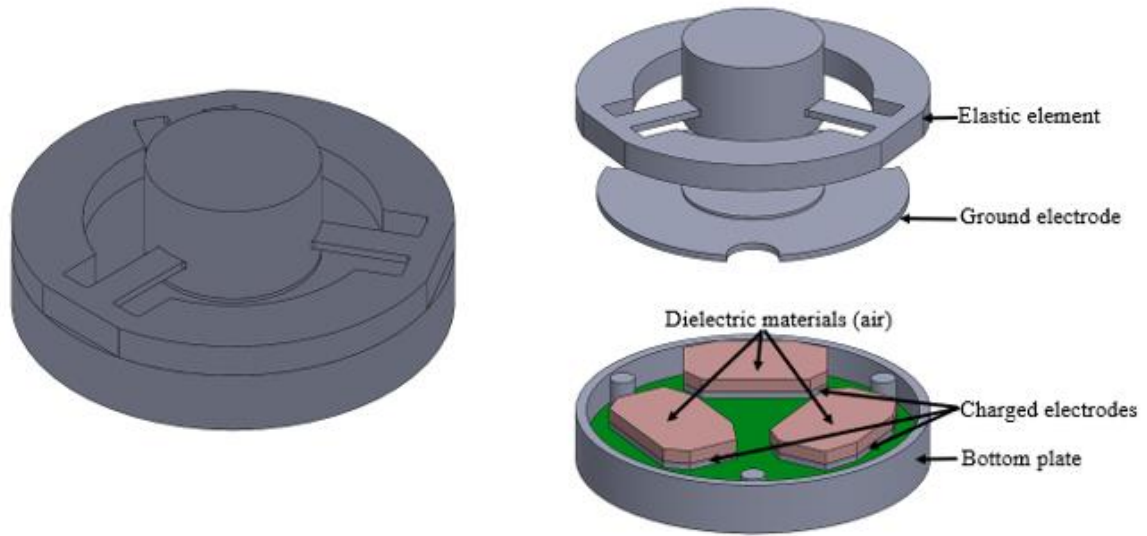
Figure 3.15: CAD model of the capacitive based sensor

The capacitance simulations are done in COMSOL using its 3D model wizard. Electromechanics physics module is used to do the capacitance analyses. This electromechanics module contains both the solid mechanics module and electrostatics module. The solid mechanics module is necessary to integrate the displacement analysis of the ground electrode under applied forces into the electrostatics module to do the capacitance analysis. The electromechanics module also contains the deforming domain space in the physics definition. As, the distance between the ground electrode and the charged electrodes change, the dimensions of the dielectric material change. The deforming domain space helps to automatically change the dielectric material as the ground electrode moves under applied force. So, it is possible to calculate the capacitance change simultaneously under applied forces.

Except the dielectric material, the elastic element, ground electrode, charged electrodes, and bottom plate is included in the solid mechanics physics. Only the ground electrode, three charged electrodes, and the dielectric material are included in the electrostatics physics. LiveLink for SolidWorks module is used to import the CAD model of the sensor in the COMSOL. The forces are applied on the top of the central solid cylinder of the elastic element. So, the top boundary of the central solid cylinder is included in the boundary load definition. Among the three load type options, the total force option is chosen. All the three components of forces can be applied both individually and in a combined manner. The bottom plate and three charged electrodes domain are included in the fixed constraint definition. The charged electrodes domains are selected as the terminal in the electrostatics module, and the terminal type is chosen as voltage. In the charge conversion physics definition, the dielectric material domain is chosen. It is necessary to choose the material type of the dielectric material as nonsolid type as we used air as the dielectric material. If we do not choose the nonsolid type, then the simulation results are not good. The dielectric domain is also included in the deforming domain definition and this deforming domain definition is included in the moving mesh physics. Aluminum 7075 T6 is chosen as the material of the sensor. Free tetrahedral mesh is used to do the mesh. The maximum element size is 1 mm, and the minimum element size is 0.01 mm, maximum element growth rate is 1.3, curvature factor is 0.2, the resolution of narrow regions is 1, and high element quality optimization is used. The completed mesh consists of 834421 domain elements, 94219 boundary elements, and 5865 edge elements.

The simulations are done for the shear force $F_x = 100N$, normal force $F_y = -100N$, and the shear force $F_z = 100N$ individually. Auxiliary sweep is used to do the simulation from 0N to 100N with an increment of 10N for the shear forces, and from 0N to $-100N$ with an increment of $-10N$ for the normal force. In this capacitance change study under different applied forces, the spatial mesh displacement, displacement field and electric potential are dependent variables. These three dependent variables are segregated in the stationary solver. The capacitances of each capacitors are calculated separately for all the forces. From the capacitance data, capacitance changes are calculated for each applied force. Then, three separate plots for each F_x, F_y, and F_z are drawn of capacitance changes vs. applied forces.

3.2.1 Capacitance Analysis for Type 1 and Type 2

In this section, the capacitance change behaviors for the type 1 and type 2 are discussed and compared. All the dimensions of the elastic element are same as the section 3.1.1.

3.2.1.1 For Shear Force F_x

Figure 3.16 shows the capacitance change behavior of the three capacitors for both type 1 and type 2 under the shear force $F_x = 100N$. From Fig. 3.16 (a), the capacitance changes in capacitor 1 for both type 1 and type 2 is negligible but the rate of change of capacitance for type 2 is higher than the type 1. For both type 1 and type 2, as the force is increased, the capacitance of the capacitor 2 is increased and the capacitance of the capacitor 3 is decreased (Fig. 3.16 b and c). So, the capacitance change behavior of all three capacitors match with the theoretical analysis in section 2.3 for the shear force

$F_x = 100N$. The capacitance changes in capacitor 1 for type 2 is nonlinear but as the capacitance change is very small, we can assume it as linear during calibration.

Figure 3.16: Capacitance change of the three capacitors under the shear force $F_x = 100N$

(a) capacitor 1, (b) capacitor 2, and (c) capacitor 3

Also, for capacitor 2 and 3, the rates of capacitance changes are higher for type 2 than type 1. For type 1, the capacitance changes in capacitor 2 is 1.22×10^{-4} pF per newton and in capacitor 3 is -1.19×10^{-4} pF per newton. For type 2, the capacitance changes in capacitor 2 is 1.67×10^{-3} pF per newton and in capacitor 3 is -1.15×10^{-3}

pF per newton. So, for all three capacitors, the capacitance changes are higher in type 2 than type 1 for the shear force $F_x = 100N$.

3.2.1.2 For Normal Force F_y

Figure 3.17 shows the capacitance change behavior of the capacitors under the normal force F_y. For both type 1 and type 2, the capacitors have increase in capacitance as the force is increased. All the three capacitor's capacitances are increased equally. Thus, the capacitance change behavior for the normal force F_y match with the theoretical analysis. For type 1, the capacitance increase is 2.65×10^{-4} pF/N, and for type 2, the capacitance increase is 2.402×10^{-3} pF/N. So, for the type 2, the capacitances are increased at much higher rate.

3.2.1.3 For Shear Force F_z

Figure 3.18 shows the capacitance change behavior of the capacitors under the shear force F_z. For both type 1 and type 2, as the force increased, the capacitance of the capacitor 1 is increased, the capacitances of the capacitor 2 and 3 are decreased equally. So, the capacitance change behavior match with the theoretical analysis. Similar to the shear force F_x and the normal force F_y, the capacitance changes are much higher in all the three capacitors for type 2. For type 1, the capacitance is change at a rate of 1.44×10^{-4} pF/N for capacitor 1, 6.99×10^{-5} pF/N for capacitor 2 and 3. For type 2, the capacitance is change at a rate of 2×10^{-3} pF/N for capacitor 1, 6.64×10^{-4} pF/N for capacitor 2 and 3.
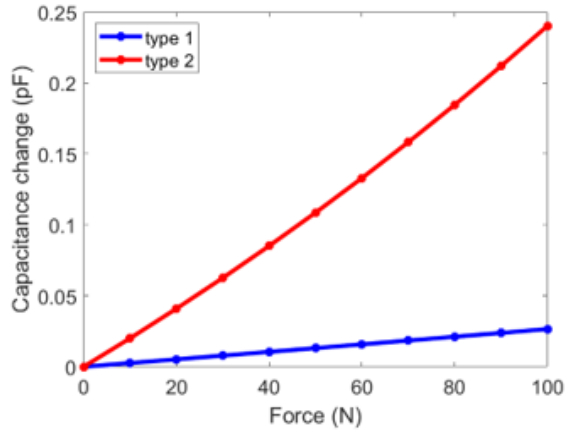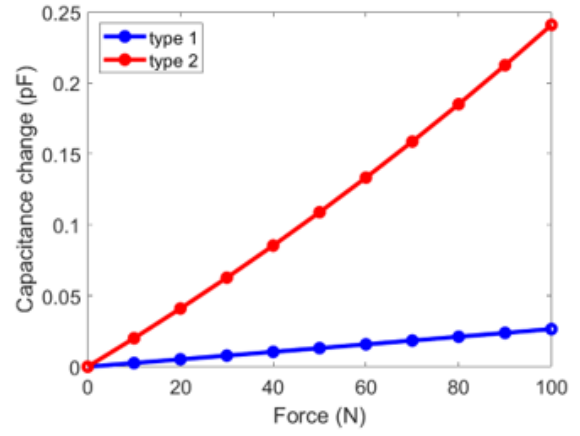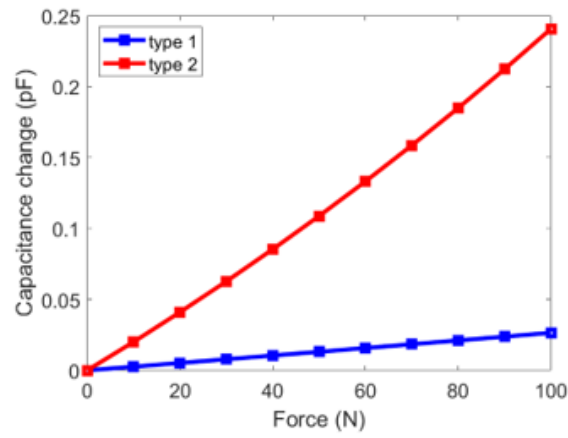
Figure 3.17: Capacitance change of the three capacitors under the normal force $F_y =$
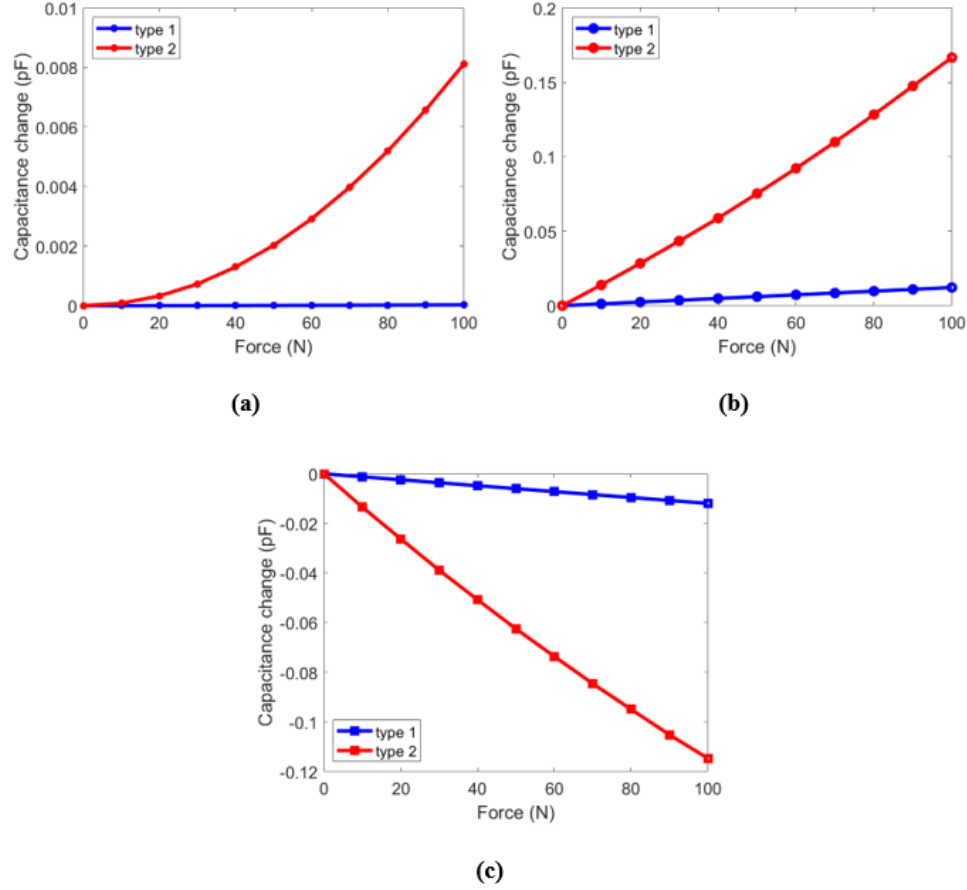
$-100N$ (a) capacitor 1, (b) capacitor 2, and (c) capacitor 3

Figure 3.18: Capacitance change of the three capacitors under the shear force $F_z = 100N$

(a) capacitor 1, (b) capacitor 2, and (c) capacitor 3

From the above discussion, if the elastic element has thick propped cantilever beams and thin fixed beams then the rate of capacitance change is lower, and if the elastic element

has thin propped cantilever beams and thick fixed beam then the rate of capacitance change is higher.

3.2.2 Capacitance Analysis for Type 2.1, 2.2, 2.3

Similar to the displacement analysis in section 3.1.2, capacitance analysis is done for type 2.1, 2.2, and 2.3. Figure 3.19 shows the capacitance analysis for the x – directional forces. The capacitor 1 does not have any significant change for all three types. The capacitance of the capacitor 2 is increased for all three types but the rate of capacitance change is higher for type 2.3. For type 2.1, the rate of capacitance change is 2.5×10^{-4} pF/N, 5.35×10^{-4} pF/N for type 2.2, and 1.7×10^{-3} pF/N for type 2.3. And the capacitance of the capacitor 3 is decreased for all three types. For type 2.1, the rate of capacitance change is -2.37×10^{-4} pF/N, -4.7×10^{-4} pF/N for type 2.2, and -1.15×10^{-3} pF/N for type 2.3. So, the rate of capacitance decrease is higher in type 2.3.

Similarly, for force in y – axis direction, all three capacitor's capacitances are increased for all three types (Fig. 3.20). The rate of capacitance changes for type 2.1 is 3.05×10^{-4} pF/N, 7.24×10^{-4} pF/N for type 2.2, and 2.4×10^{-3} pF/N for type 2.3. So, for force in y – axis also, the rate of capacitance change is higher for type 2.3.

Figure 3.21 shows the capacitance change behavior for z – directional force. For forces in z – axis direction, the capacitance of capacitor 1 is increased for all three capacitors. But the rate of capacitance changes for type 2.1 is 2.94×10^{-4} pF/N, for type 2.2 is 6.3×10^{-4} pF/N, and for type 2.3 is 2×10^{-3} pF/N. So, the capacitance change is higher in type 2.3. The capacitance is decreased for capacitor 2 and 3 for all three types.

The rate of capacitance change is -1.37×10^{-4} pF/N for type 2.1, 2.7×10^{-4} pF/N for type 2.2, and -6.6×10^{-4} pF/N for type 2.3. So, the rate of capacitance change is higher for type 2.3. So, for all three directional forces, the capacitance changes are higher for type 2.3.
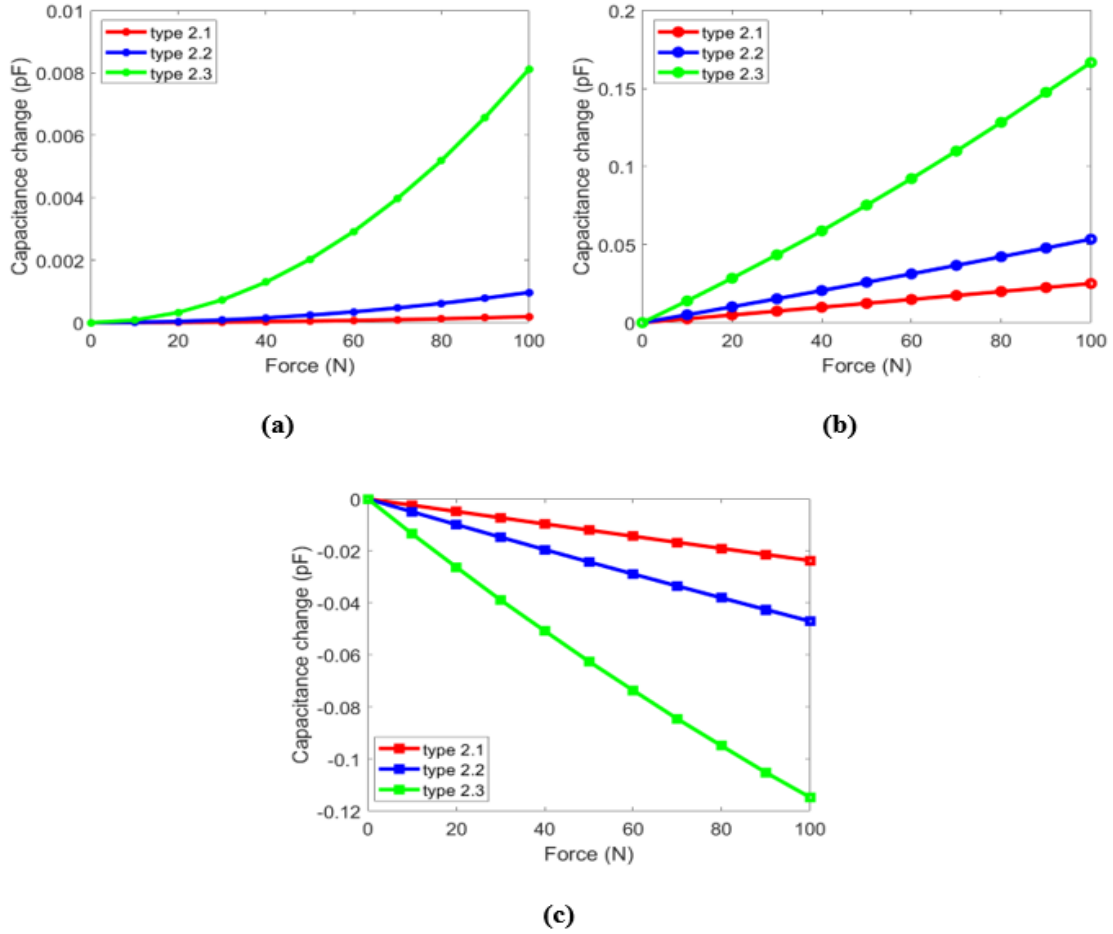
Figure 3.19: Capacitance change of the three capacitors under the shear force $F_x = 100N$

(a) capacitor 1, (b) capacitor 2, and (c) capacitor 3
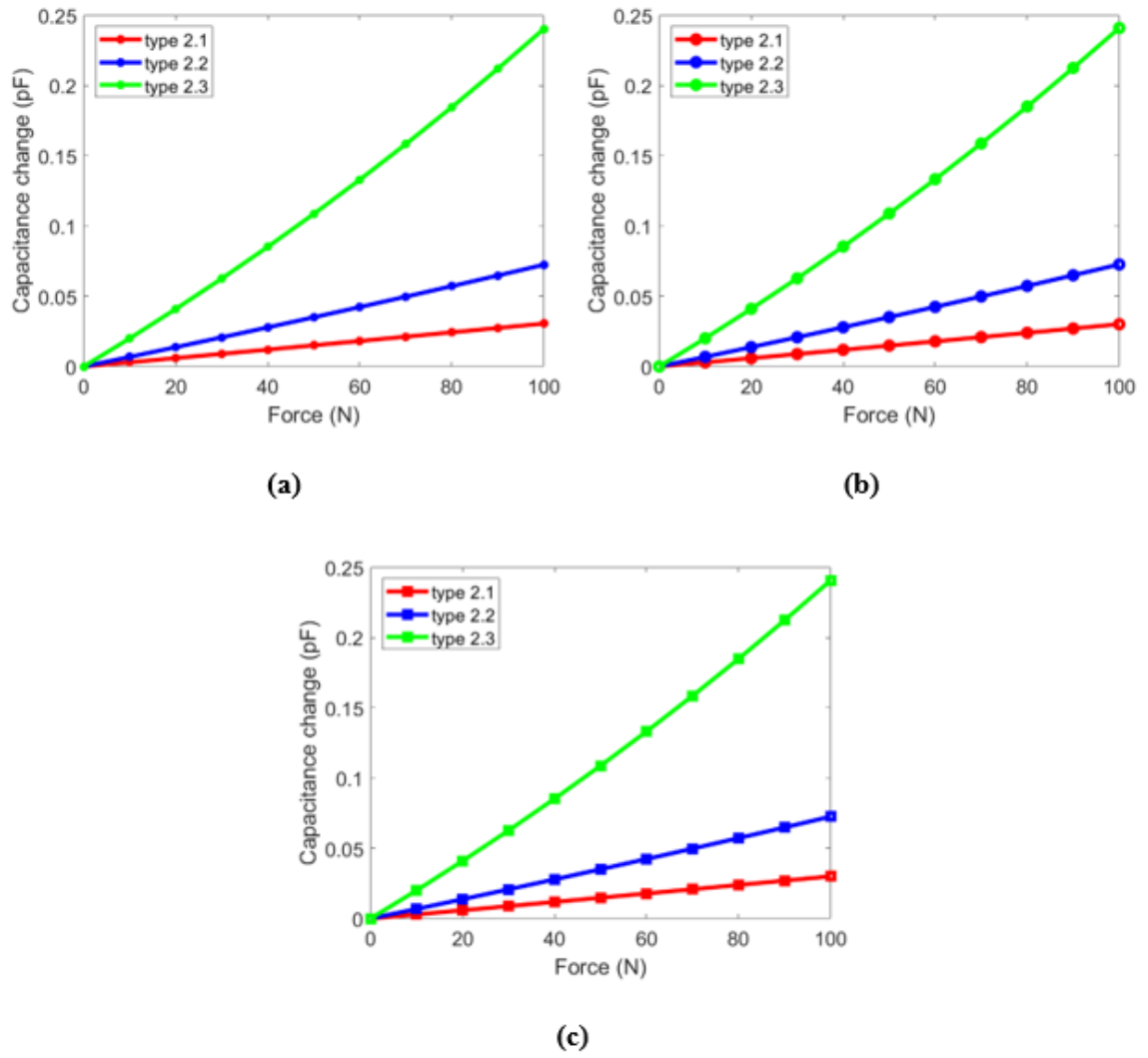
Figure 3.20: Capacitance change of the three capacitors under the normal force $F_y = -100N$ (a) capacitor 1, (b) capacitor 2, and (c) capacitor 3
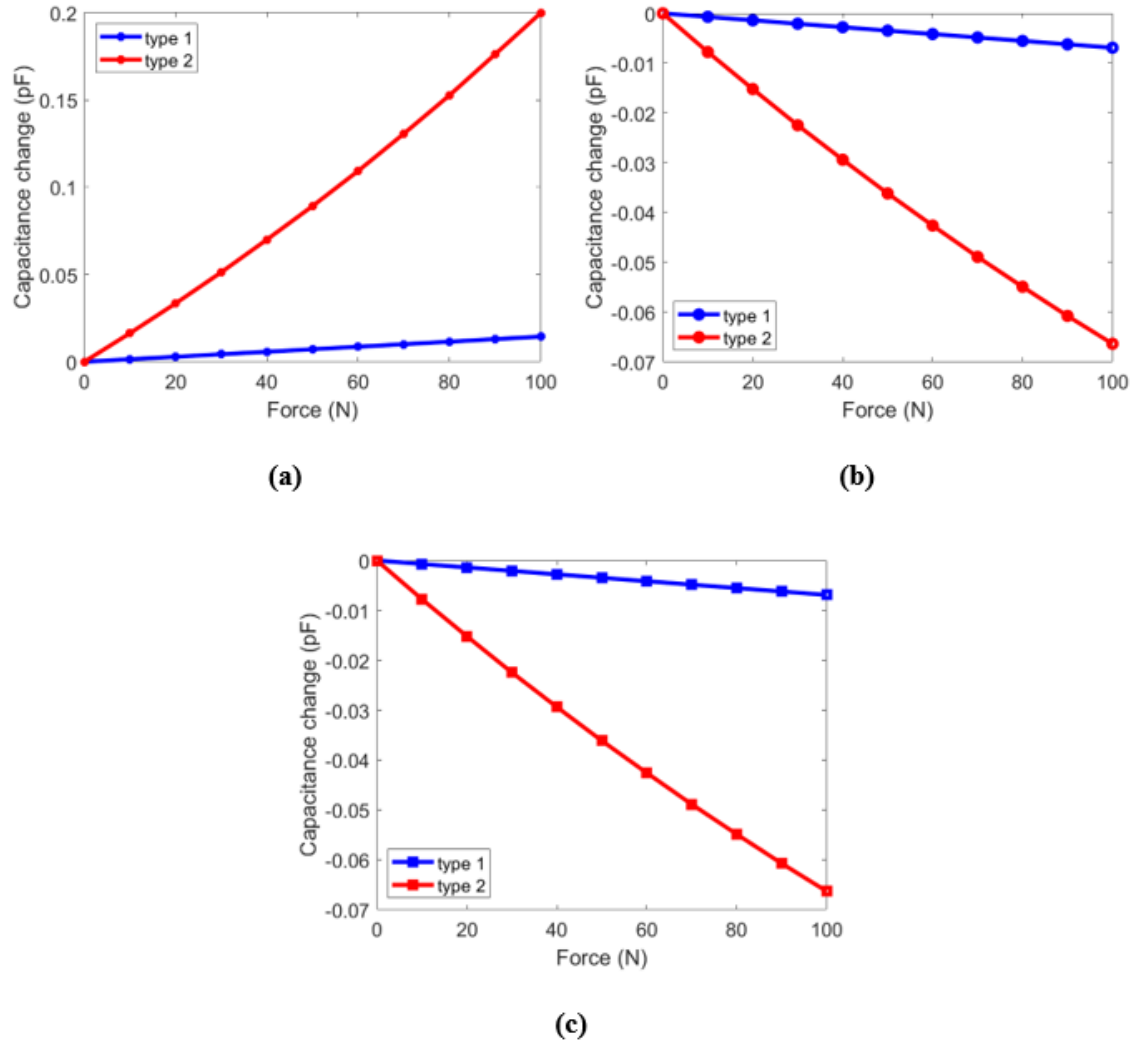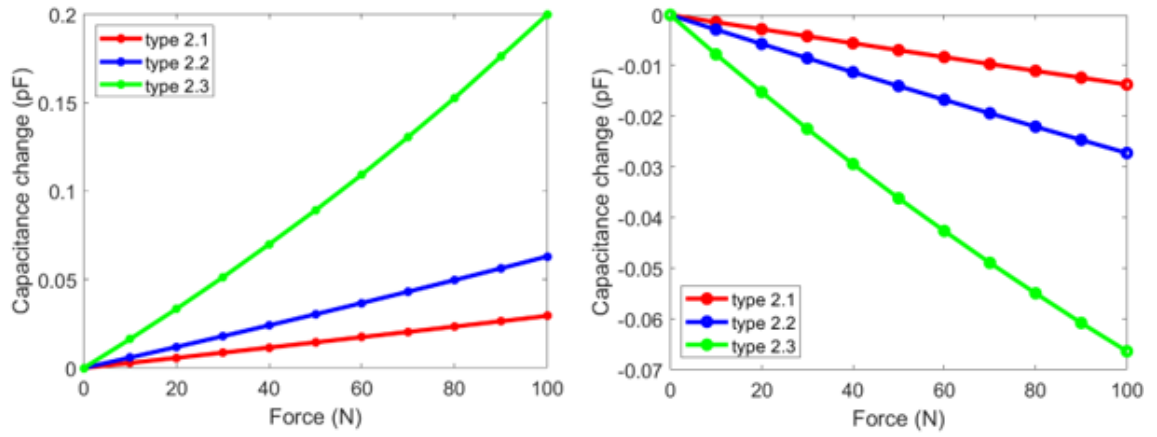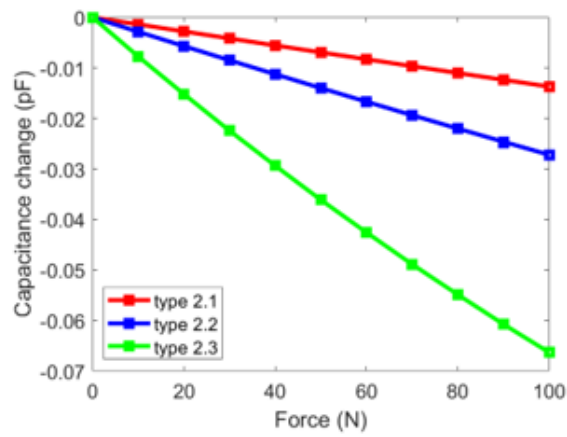
Figure 3.21: Capacitance change of the three capacitors under the shear force $F_z = 100N$

(a) capacitor 1, (b) capacitor 2, and (c) capacitor 3

CHAPTER 4

DESIGN

In this chapter, the design of the developed sensor is discussed. In this capacitive based sensor, under applied forces, only the elastic element has physical change. No other parts have any physical change. The physical change of the elastic element is measured by the capacitors. The capacitors and the capacitance measuring circuits are inside a bottom plate. The elastic element sits on top of the bottom plate.

4.1 Elastic Element

The elastic element consists of a hollow cylinder, a solid cylinder, three propped cantilever beams, three fixed beams (Fig. 4.1). The radius of the solid cylinder is smaller than the hollow cylinder and stays inside the hollow cylinder. These two cylinders are concentric and are connected to each other by the beams.

The outer radius of the hollow cylinder is 25 mm, and the inner radius is 17 mm. The height of this hollow cylinder is 4 mm. The radius of the central solid cylinder is 10 mm, and height is 12.50 mm. As the discussion in section 3.2.2, thin rectangular horizontal propped cantilever beams have been used. The length of the propped cantilever is 12.38 mm, width is 4 mm, and height is 1 mm. The length of the fixed beam is 16 mm, width is 1.50 mm, and height is 4 mm which is equal to the height of the hollow cylinder.
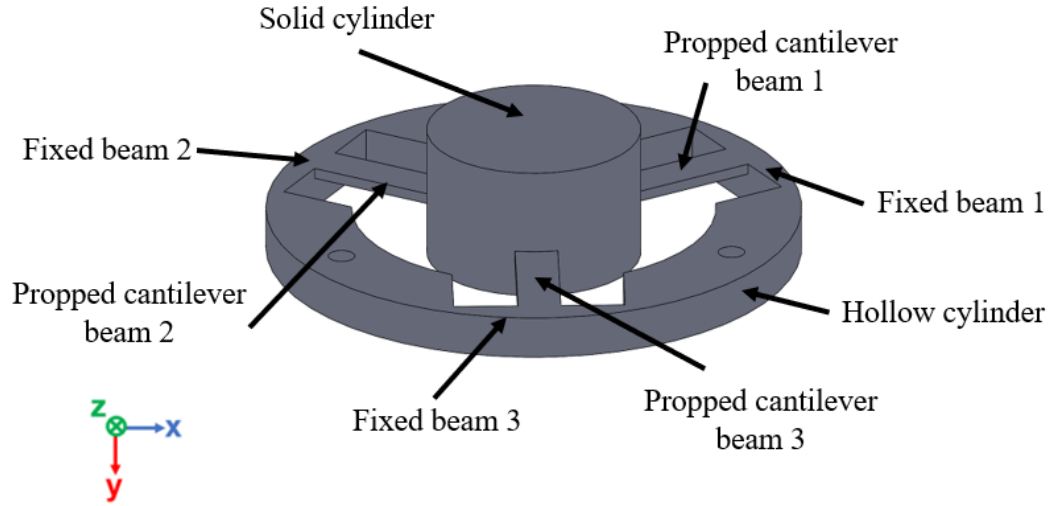
Figure 4.1: The CAD model of the elastic element

Figure 4.2 shows the stress distribution of the elastic element under the shear force $F_x = 100N$, normal force $F_y = -100N$, and the shear force $F_z = 100N$. The highest stress induced in the elastic element is 4.947×10^8 N/m² which is lower than the yield stress 5.05×10^8 N/m². So, after applying the maximum load, the displacement of the elastic element stays inside the elastic limit. It helps the sensor not to suffer from hysteresis and have good repeatability. The elastic element is attached to the bottom plate using three M3 screws. The center of the screw holes is at a distance of 21 mm from the center of the large cylinder.
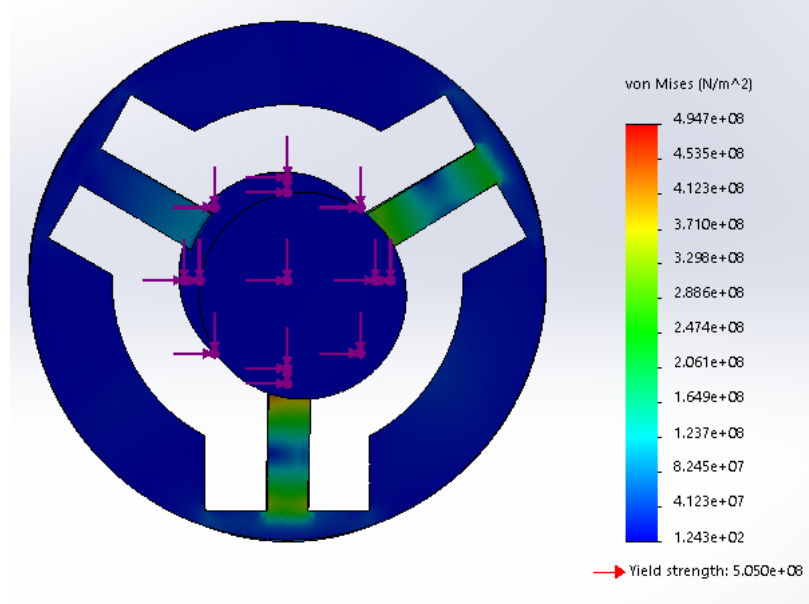
Figure 4.2: Stress distribution of the elastic element under the shear force $F_x = 100N$, normal force $F_y = -100N$, and the shear force $F_z = 100N$

4.2 Capacitors

Three capacitors are used in this capacitive based force sensor. Three charged electrodes are placed on a printed circuit board (PCB) and a common ground electrode make the three capacitors. The ground electrode does not touch the charged electrodes. Here, air works as a dielectric material. Figure 4.3 shows the ground electrode and the charged electrode PCB with the three charged electrodes.

Figure 4.3 (a) shows the ground electrode. The radius of the ground electrode is 21 mm. Materials are cut from the sides of the ground electrode to have space for the screws. A circular cut is done at the center of the ground electrode to fit the ground electrode to the elastic element's central solid cylinder. The radius of the circular cut is

10.10 mm. Figure 4.3 (b) shows the charged electrode PCB with the electrodes. The electrodes are at an angle of 120° from each other. The thickness of the PCB board is 1.60 mm. The electrodes are trapezoidal in shape. Figure 4.3 (c) shows the dimension of the charged electrodes. The height of the electrodes is negligible. 6 small holes are made at the center of the PCB board. These holes are used to connect the charged electrode PCB board to the capacitance measuring PCB board.

(a)

(b)

(c)
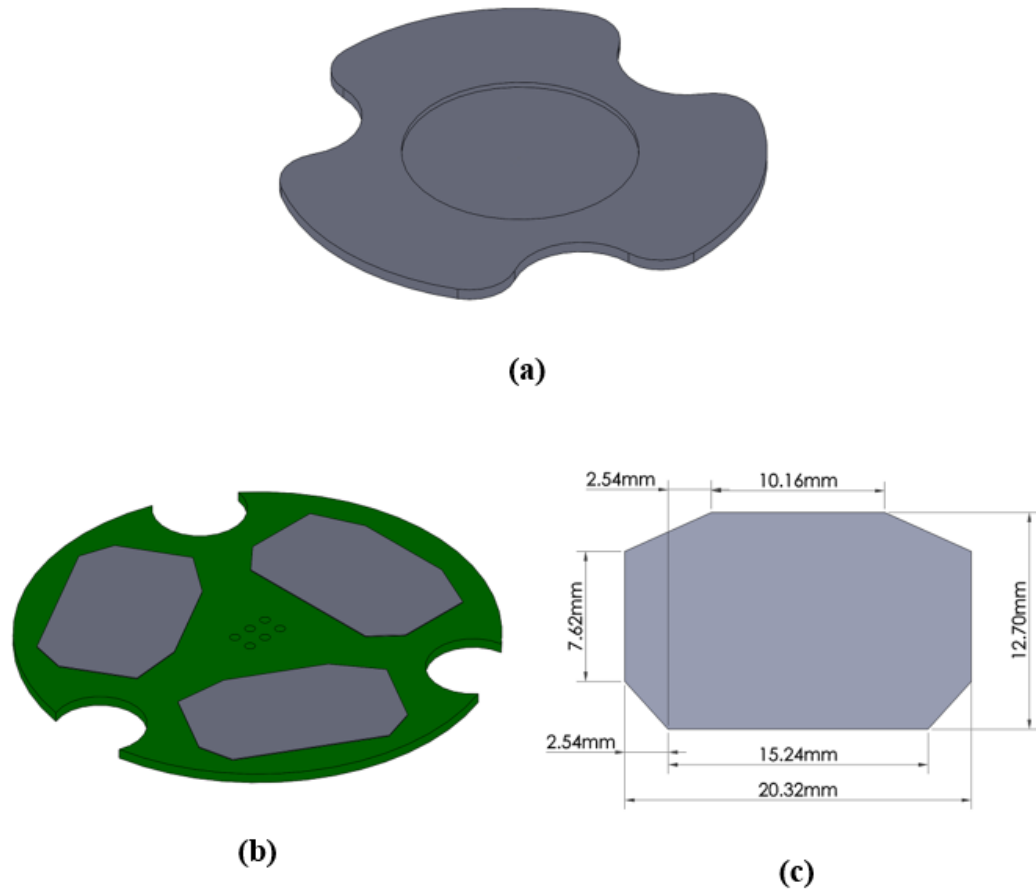
Figure 4.3: Measuring element of the sensor (a) ground electrode, (b) charged electrode printed circuit board, and (c) dimensions of the charged electrodes

4.3 Bottom Plate

The capacitors and the capacitance measuring PCB stays inside the bottom plate. For the ease of fabrication, the bottom plate is divided into two parts. The radius of the bottom plate is 25 mm, and the thickness of the wall is 2 mm. One is middle ring, and another is bottom part.

Figure 4.4 shows the CAD model of the middle ring. The middle ring is a simple hollow cylinder. One slot is cut on the wall of the middle ring to pass the wires for the programming of the PCB board. Figure 4.5 shows CAD model of the bottom part. The bottom part has two slots on the wall. One is for passing the data transfer wires and another is for the battery connection. Two small cylinders at the bottom of the bottom plate. The capacitance measuring PCB sits on top of these two cylinders and attached to the bottom plate using screws. These two cylinders help to maintain a gap between the PCB and the surface of the bottom plate.
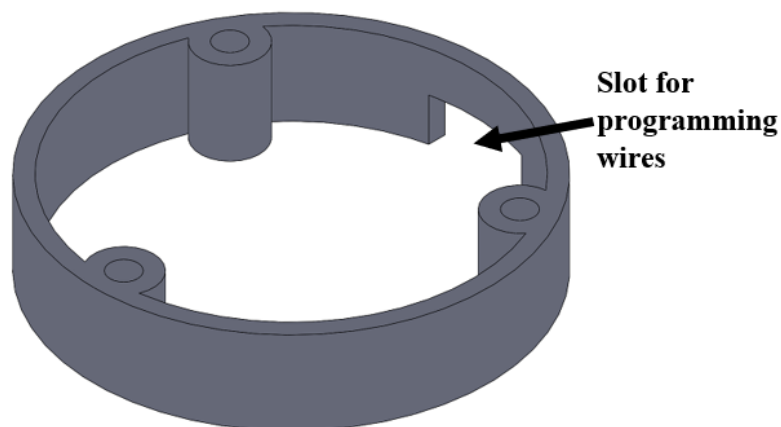
Figure 4.4: The CAD model of the middle ring
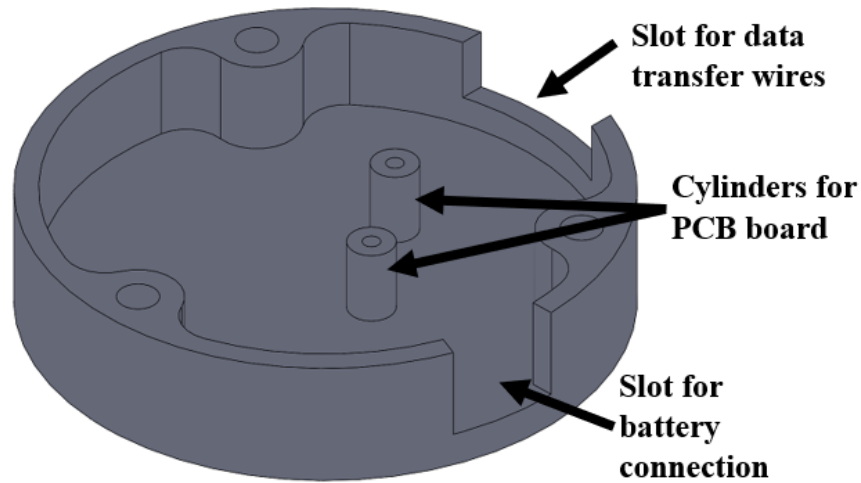
Figure 4.5: The CAD model of the bottom part

4.4 Full Sensor

Figure 4.6 (a) shows the CAD model of the developed sensor after assembly, and Fig. 4.6 (b) shows the exploded view of this sensor. After assembling all the parts, the height of the sensor is, and the radius of the sensor is 25 mm. The ground electrode is attached to the elastic element using glue. The charged electrode PCB board and the capacitance measuring PCB board are connected to each other by male connectors. The charged electrode PCB board stays on top of the capacitance measuring PCB board. The capacitance measuring PCB board is sits on top of the two small cylinders and attached to it using M2 screws. The elastic element sits on top of the bottom plate. They are connected to each other using three M3 screws.
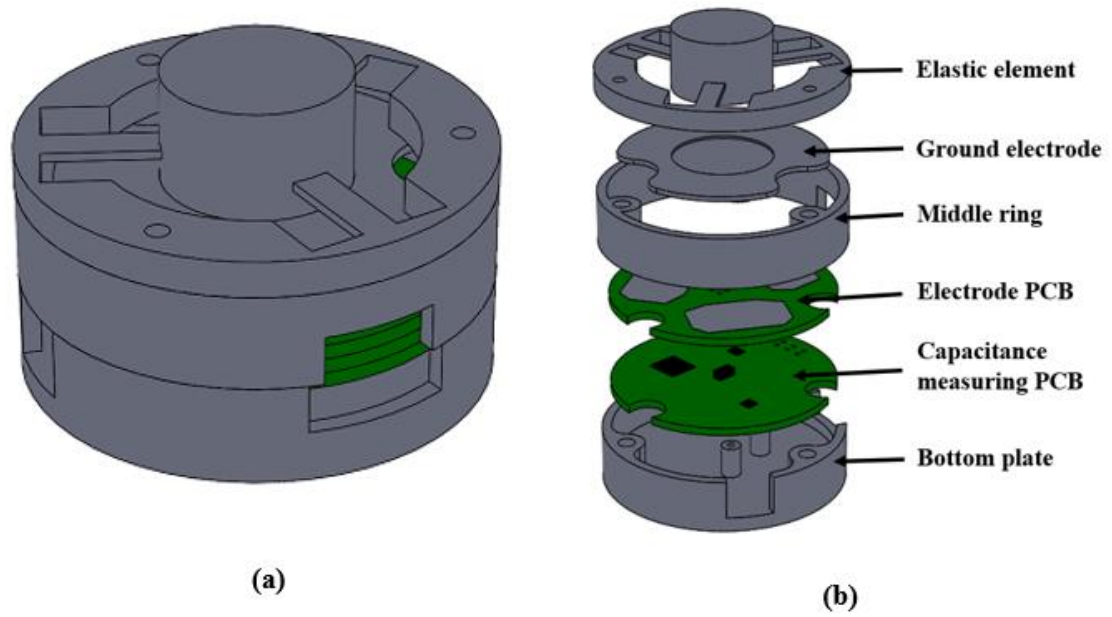
Figure 4.6: The full sensor (a) after assembling all the parts, and (b) its exploded view.

CHAPTER 5

FABRICATION

The fabrication of the sensor is divided into two parts. One part is making the mechanical parts, and another is the electronic parts. The mechanical parts are elastic element, ground electrode, middle ring, and bottom plate. The electronic parts are charged electrode PCB and capacitance measuring PCB.

All the mechanical parts were fabricated using a CNC machine. It is a desktop milling machine which is made by bantam tools. Autodesk® **Fusion 360™** was used to make the G-code for the CNC machining. This software works better with the STEP (Standard for the Exchange of Product Data) files which is an ISO standard exchange format. SolidWorks can convert the drawings into STEP file. But the axis orientation of Fusion 360 does not match with the SolidWorks. So, to match the axis orientation with the Fusion 360, the SolidWorks drawing files axes were converted using a software named PrusaSlicer (https://www.prusa3d.com/prusaslicer/). The SolidWorks drawing files were saved into STL (stereolithography) format. This STL files were imported into PrusaSlicer and then axes were converted to match the Fusion 360 format. Then this file was exported as STL file again. This STL file was then converted into STEP file using FreeCAD (https://www.freecadweb.org/).

In the FreeCAD, before creating STEP file, first the mesh of the STL file was evaluated and repaired if any error was found. This can be done using Mesh design tool. Mesh design tool can be activated from the top toolbar menu. After evaluating and repairing the mesh, we had to create shape from mesh. This shape was then converted into solid and this solid design file was exported as STEP file. This STEP file was used in Fusion 360 to make the G-code.

In the Fusion 360, the G-code was made in the manufacturing environment. Here, from the model tab, the coordinate system can be chosen. The origin of the coordinate system can be changed for ease of operation. The stock tab was used to set the dimension of the stock used to make the part. Here, the fixed size stocks were used, and the model was placed into the stock in desired position. Custom tool library was used to set the tool properties. This custom tool library can be found on the website of the Bantam tools. Depending on the operation, the cutting tool was selected from this custom library. Different speed and feed were chosen for each operation.

5.1 Elastic Element

Figure 5.1 shows the fabrication steps of the elastic element. Tight-Tolerance High-Strength 7075 Aluminum was used to make the elastic element. The stock length was 12 inches, width was 6 inches, and height was 0.625 inch. The temper of this aluminum is T651. As the stock size was much higher than the sensor size. So, first a bend saw was used to cut and to make a stock of square shape of 52 mm in length.

The diameter of the elastic element is 50 mm. So, first 2D contour operation was used to give the stock a square shape of 50 mm in length. As the height of the stock was higher than the height of the elastic element, 2D facing operating was done to make the
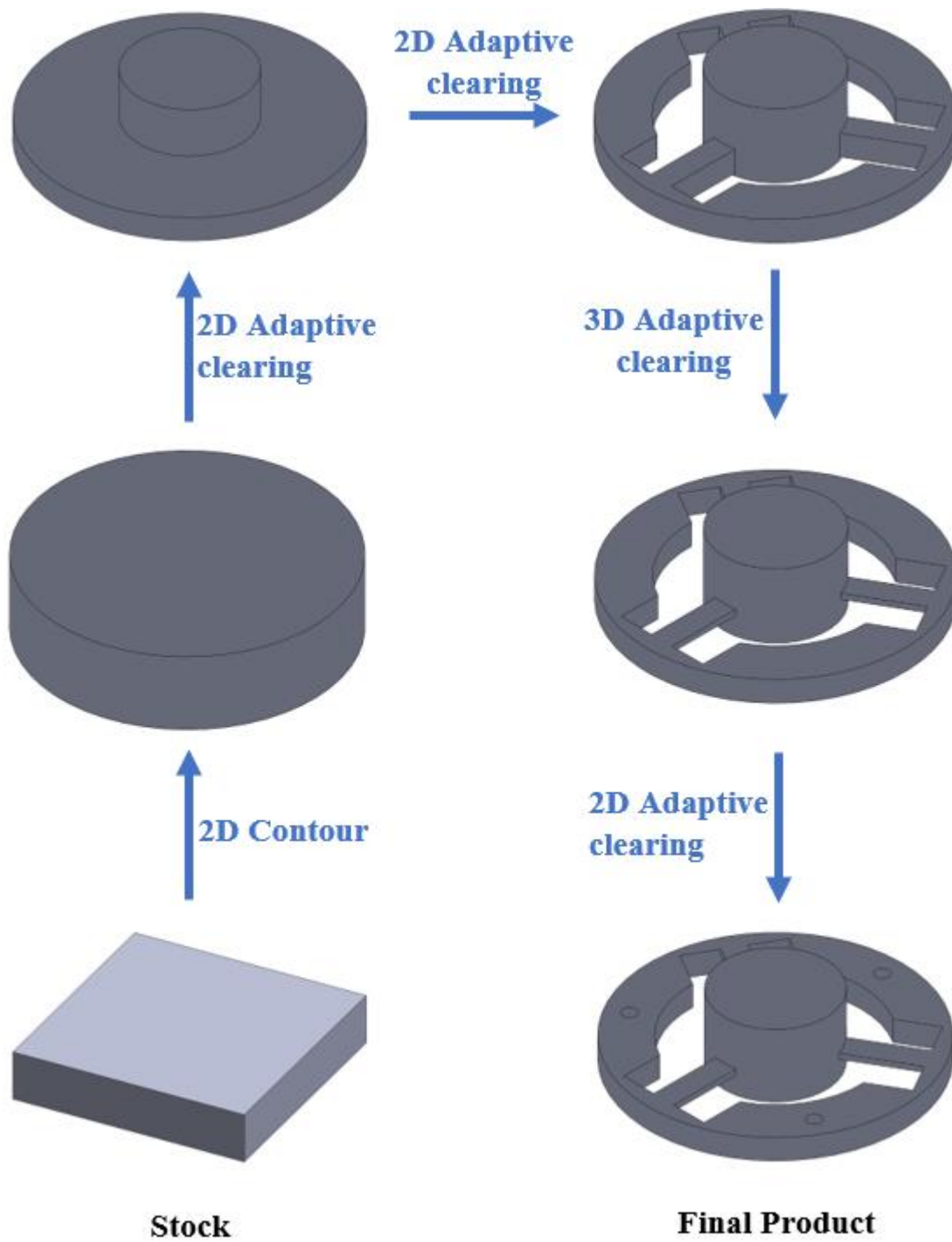
Figure 5.1: The fabrication process of the elastic element

stock's height 12.5 mm, same as the elastic element height. Then, 2D contour operation was used to get the shape of the large hollow cylinder. After that, 2D adaptive clearing operation was used to make cylindrical shape of the central solid cylinder. Then 2D adaptive clearing operation was used to cut the slots to make the propped cantilever beams. After this operation, the height of the propped cantilever beams was 4 mm. But according to the design the height of the propped cantilever beam is 1 mm. So, to make the height 1 mm, 3D pocket clearing operation was used. Then 2D adaptive clearing operation was used to make the holes for the screws. Only for this operation, 1/16-inch Flat end mill cutter was used. For all other operations, 1/8-inch Flat end mill cutter was used. Figure 5.2 shows the final fabricated part after all the operations.
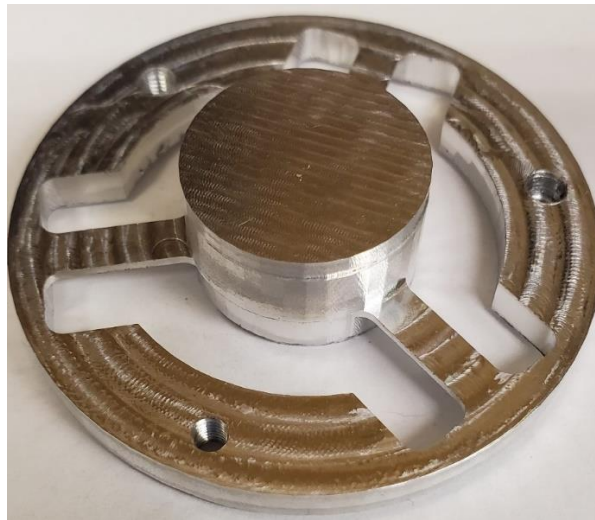
Figure 5.2: The elastic element after the fabrication

5.2 Middle Ring

Figure 5.3 shows the fabrication process of the middle ring. Same as the elastic element, 2D contour and 2D facing operation were done first to make correct size of the stock for the middle ring. First, 3D adaptive clearing operation was used to make the hollow shape of the middle ring. Then 2D contour operation was used to do the circular cut for making the cylindrical shape of the middle ring. Then, 2D adaptive clearing operation was used to make the holes for the screws. Finally, 3D pocket clearing operation was done to cut slots for the programming wires. All the operations were done using 1/8-inch flat end mill cutter. Figure 5.4 shows the final fabricated middle ring after completing all the operations.
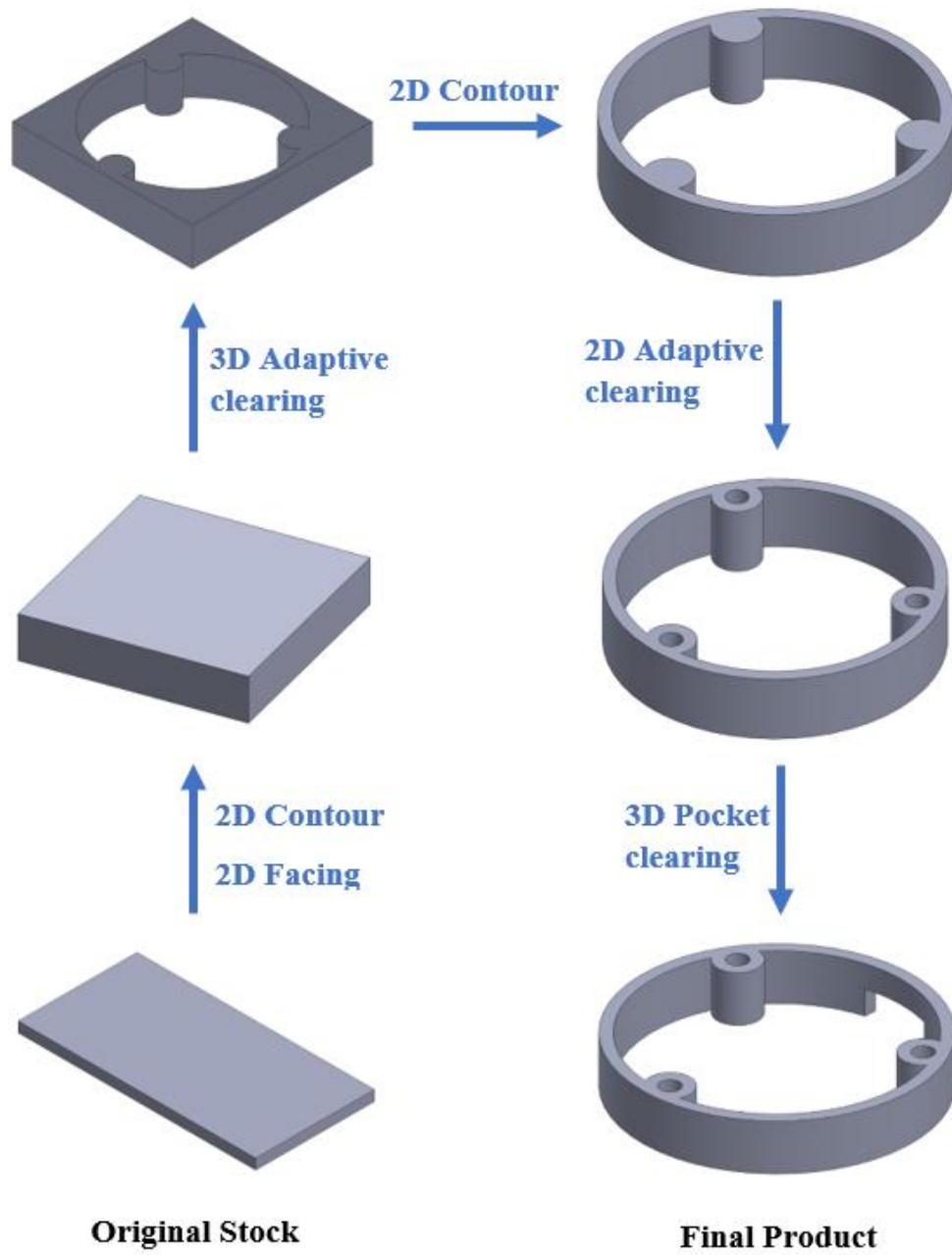
Figure 5.3: The fabrication process of the middle ring

Figure 5.4: The middle ring after fabrication

5.3 Bottom Plate

Figure 5.5 shows the fabrication steps of the bottom plate. After the 2D contour and 2D facing operation to make ready the stock same as before, again 2D contour operation was done to give the stock the cylindrical shape. Then 3D adaptive clearing operation was done to clear the material. Then 2D adaptive clearing was done to make screw holes. First 1/8-inch flat end mill was used to make the holes for the M3 screws. Then 1/16-inch flat end mill cutter was used to make the holes for the M2 screws. Then again, the 1/8-inch flat end mill cutter was used to cut the slots for the data transfer wires and the battery connection using 3D pocket clearing operation. Figure 5.6 shows the final fabricated part after completing all the operations.
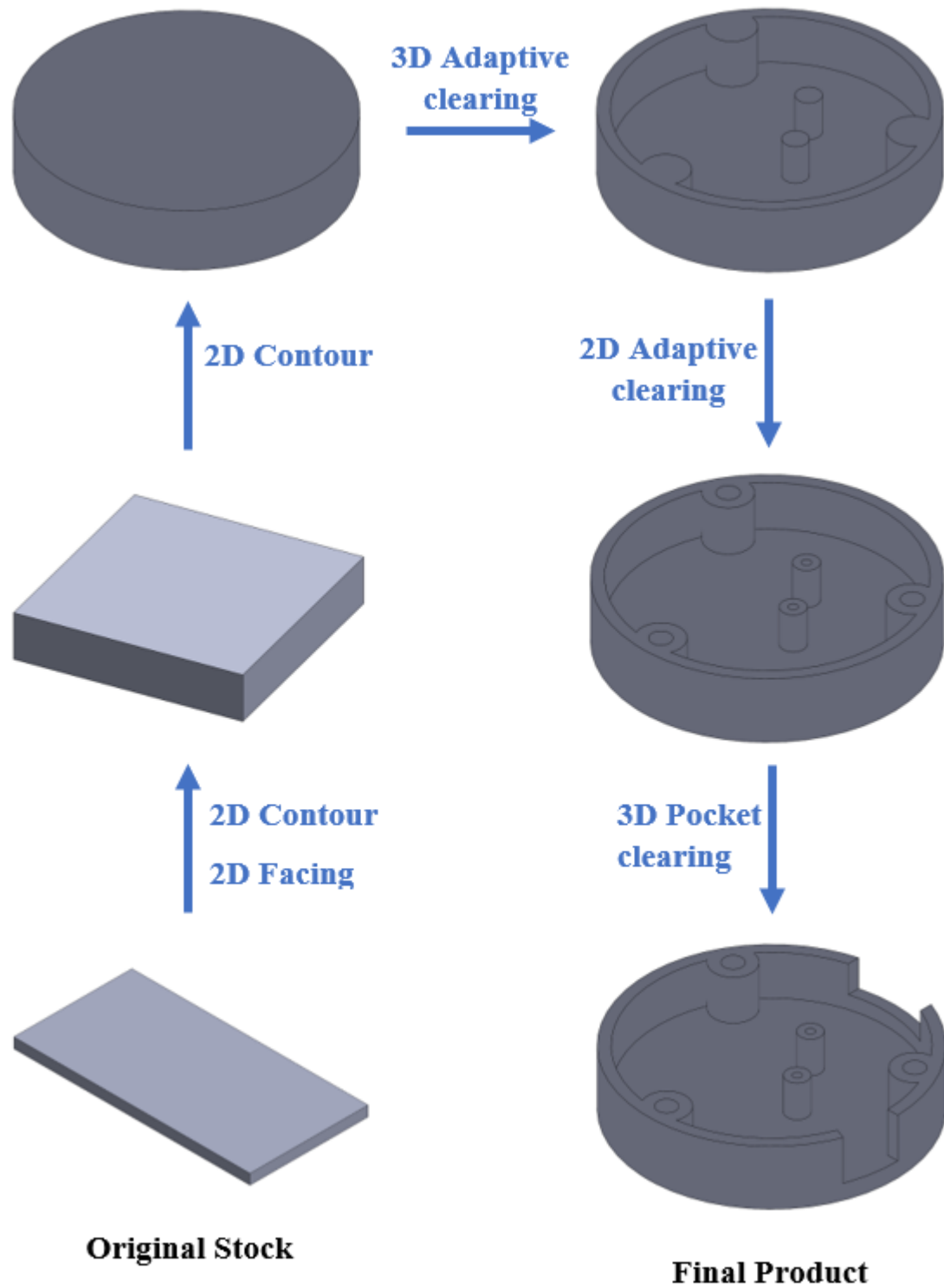
Figure 5.5: The fabrication process of the bottom plate

Figure 5.6: The bottom plate after fabrication

5.4 Ground Electrode

Figure 5.7 shows the fabrication steps of the ground electrode. After the main

stock was ready by doing the similar operations as before, 2d contour operation was done

to make the cylindrical shape. The 2D Adaptive clearing operation was done to cut the

corners. Then 2D pocket clearing operation was done to make the small hole which is

used to connect the ground electrode to the central solid cylinder of the elastic element.

Figure 5.8 shows the final fabricated part after all the operations.
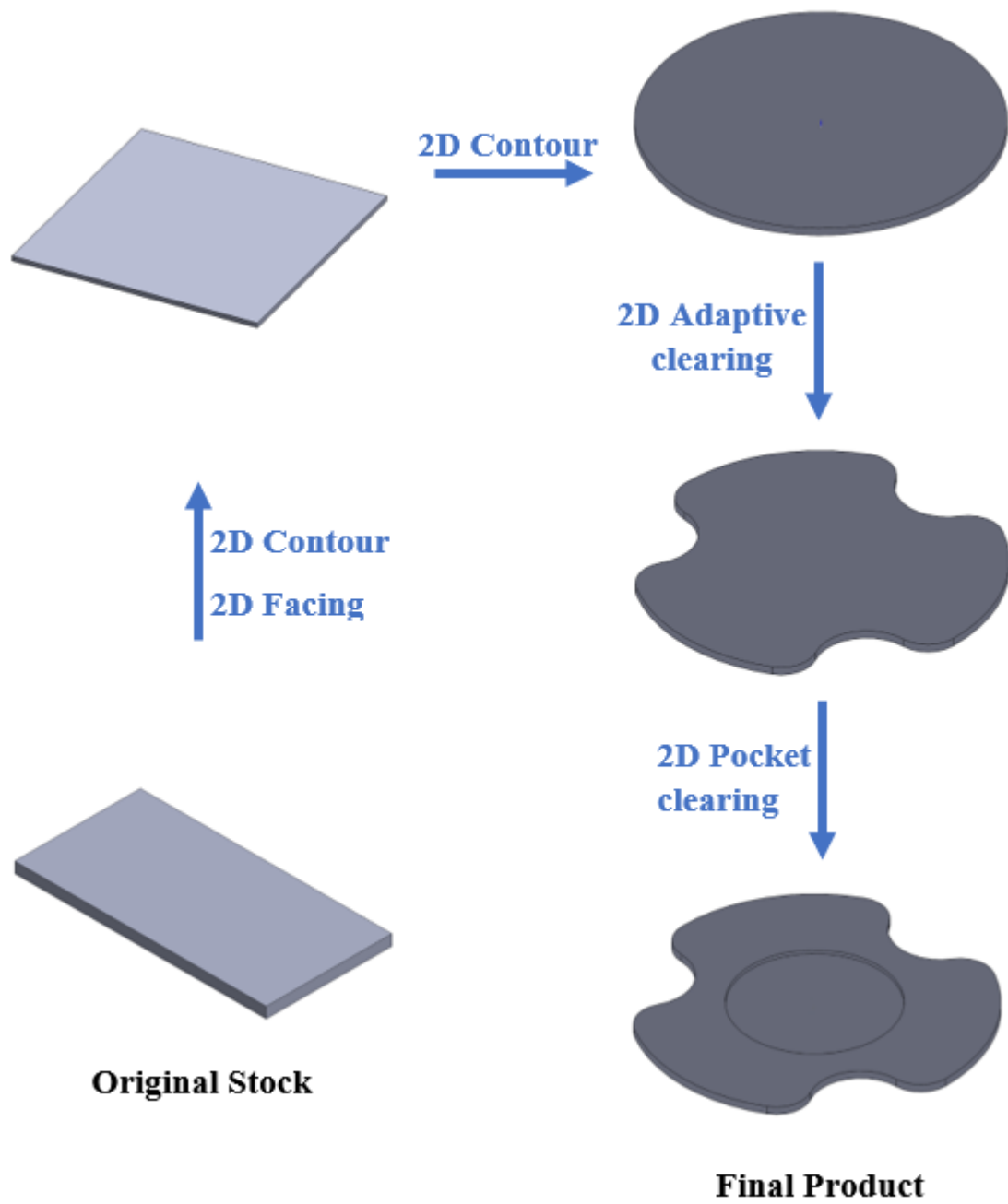
Figure 5.7: The fabrication process of the ground electrode

Figure 5.8: The ground electrode after fabrication

5.5 Capacitance Measuring PCB

The printed circuit board (PCB) for measuring the capacitance was designed using EasyEDA. The component lists are shown in converts the analog capacitance measurement into digital and send it to the microcontroller through I2C communication.

Table 5.1. AD7147-1 is used as the capacitance to digital converter (CDC). Figure 5.9 shows the EasyEDA diagram and Fig. 5.10 shows the PCB board after soldering all the components. It has 13 capacitance sensor inputs and I^2C compatible serial interface. It requires only 1mA current during full mode operation. So, it is very convenient to use in a capacitive-based sensor. This AD 7147-1 is designed for single electrode capacitance sensors. So, only the charged electrodes have connection with this CDC. No connection is necessary from the ground electrode. It helps the ground electrode to freely move under forces. This Capacitance to digital converter (CDC) converts the analog

capacitance measurement into digital and send it to the microcontroller through I2C communication.

Table 5.1: The component list for the capacitance measuring PCB

Component	Model / Value	Quantity	Position in PCB
Microcontroller	ATMEGA644PA-AU	1	U1
CDC	AD7147-1	1	U2
Capacitor	0.1μF	7	C1, C3, C4,C5,C6,C7,C8
Capacitor	1μF	3	C2, C11, C12
Capacitor	22pF	2	C9, C10
Resistor	4.7kΩ	1	R1
LED	LG R971-KN-1	1	LED1
Resistor	56Ω	1	R2
Resistor	2.2KΩ	3	R3, R4, R5
Regulator	TLV70033DDCR	1	U5
Header	Male 2.54_2*3	2	H1, H2
Header	Male 2.54_1*6	1	P1
Header	Male 2.54_1*1	5	P2, P3, P4, P5, P9
Battery Connector	B2B-PH-K-S(LF)(SN)	1	CN1
Crystal Oscillator	ECS-080-18-23G-JGN-TR	1	U3
Switch	TL1015AF160QG	1	S1
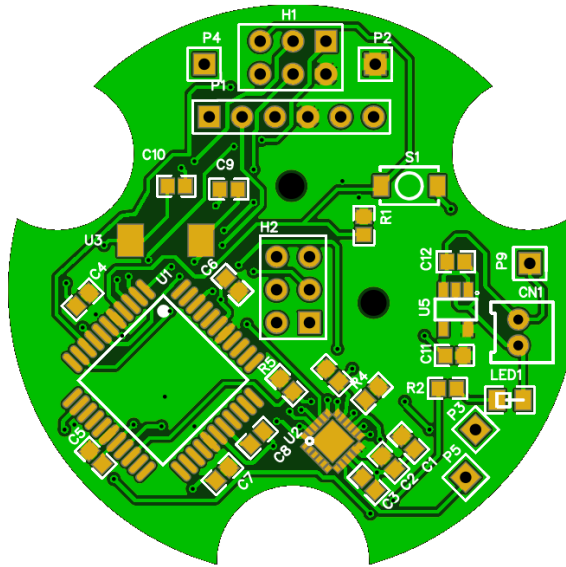
(a)
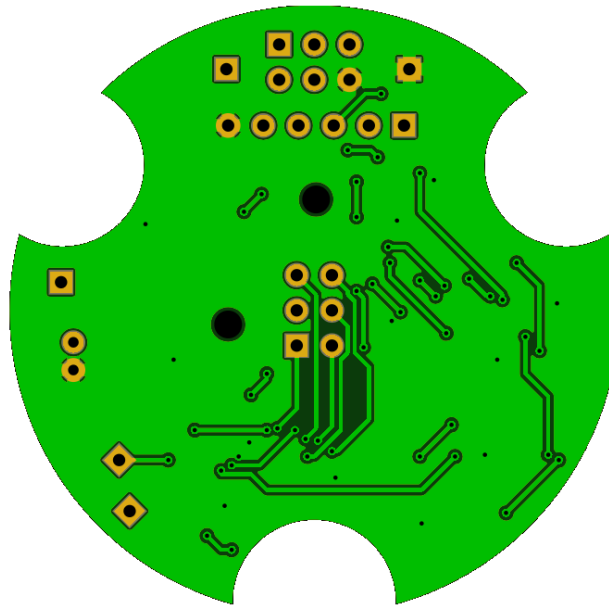
(b)

Figure 5.9: The capacitance measuring PCB (a) top view, and (b) bottom view
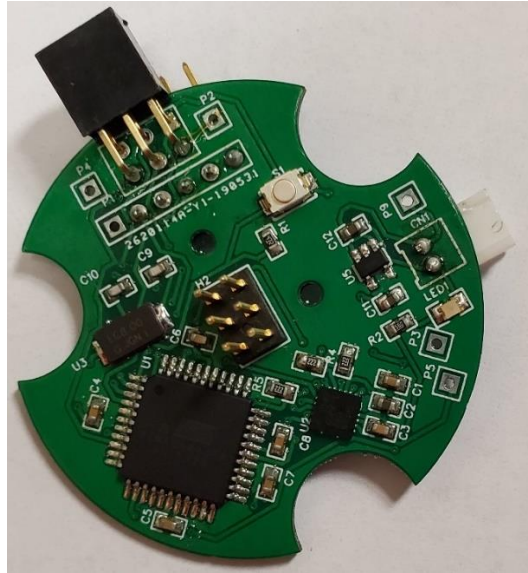
(a)
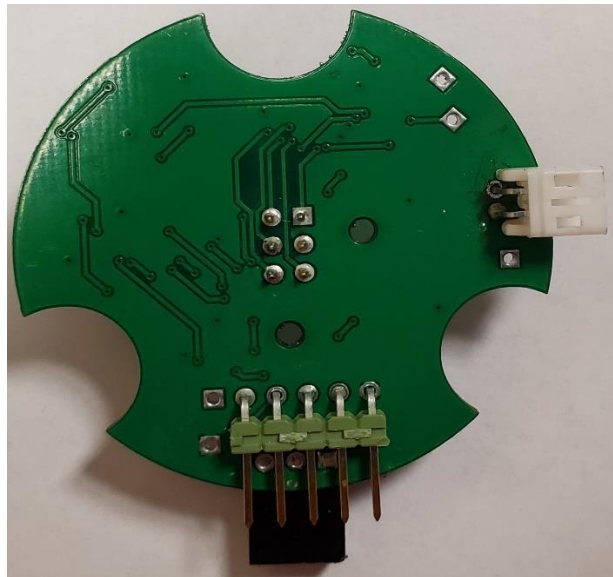
(b)

Figure 5.10: The capacitance measuring PCB after soldering all the components (a) top view, and (b) bottom view

There is a 2×3 position (H1) for programming the microcontroller. 1×6 position (P1) is used for data transfer to the computer. A 12V battery is used to power the PCB. There is a reset switch (S1) which helps to reset the microcontroller to its initial condition. Polulu USB AVR Programmer v2.1 is used for both programming the microcontroller and data transfer. It is a compact, in-system programmer (ISP) for AVR microcontroller. It has the ability of being installed as two virtual COM ports so that both communication for programming and serial communication for data transfer can be done simultaneously.

5.6 Charged Electrode PCB

The three aluminum electrodes were printed on a printed circuit board. So, no manual work is necessary to attach the electrodes. Figure 5.11 shows the charged electrode PCB. The three electrodes are 120^0 degree apart from each other. Though the 2×3 holes (H2), the charged electrode is connected with the capacitance measuring PCB.
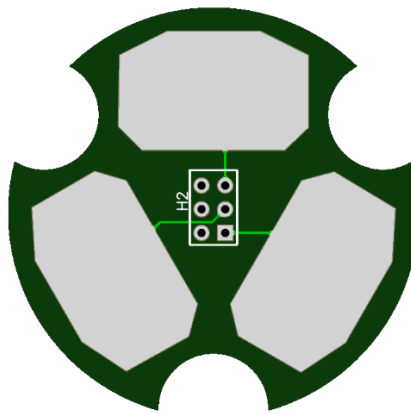
Figure 5.11: The charged electrode PCB

CHAPTER 6

EXPERIMENTS AND RESULTS

Various experiments had been done to calibrate and evaluate the sensor. First, various forces were applied to each direction and capacitance changes were recorded. From this data, calibration matrix was calculated. Using this calibration matrix, more experiments were done to evaluate the sensor. An experimental test setup has been developed to do the experiments.

6.1 Test Setup for the Experiment

Figure 6.1 shows the CAD model of the test setup. The test setup consists of three 500 mm aluminum C-Beam linear actuators with lead screw-mounted gantry carts. Each linear actuator is powered by NEMA-23 stepper motors and is used to apply force in each direction. The linear actuators are supported by a total of four aluminum 20×20 mm linear rails connected using spring loaded tee nuts and cast aluminum corner brackets. The supporting beams are screwed into two aluminum base plates along with side support brackets. They are connected to the base and are screwed to an optical table. A 3D printed end effector is attached at the bottom of the first linear actuator. Three Singletact capacitive based force measuring sensors are used to know how much force is applied in each three direction by the test setup
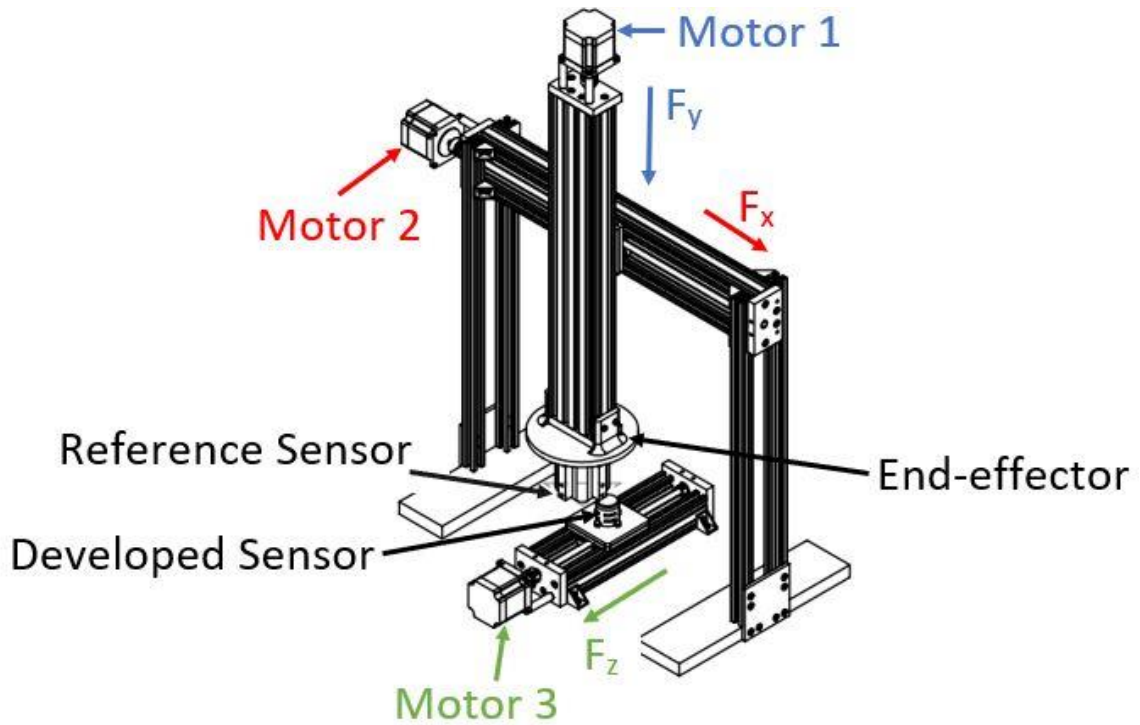
Figure 6.1: The CAD model of the experimental setup

6.1.1 Construction of the Test Setup

First, the gantry cart assemblies were attached to the motors. Two gantry carts then attached perpendicular to each other. V-slot aluminum extrudes hold the gantry cart assemblies to the designed table by support brackets. The third linear actuator lies on the optical table and attached using screws. A base was printed using 3D printer where the developed sensor would sit. This base was attached to the gantry cart of the third linear actuator which lies on the optical table. Then the 3D printed end effector was attached at the bottom of the vertical linear actuator by screws.

6.1.2 End Effector

The end effector was made using a 3D printer. Figure 6.2 shows the CAD model

of the end effector, and its attachments. It had a rectangular hollow box shape, and it was

attached to the linear actuator by 4 screws. Three rectangular small bars were attached to

the bottom of the end effector. These three bars help to apply forces in three directions.

Screws were used to attach the bars to the end effector. So, whenever necessary, these

bars can be removed from the end effector. Singletact capacitive-based sensors

(https://www.singletact.com/) had been used to measure how much force is applied using

the test setup.

These sensors can measure force in only one direction. So, three sensors had been

used to measure forces in three directions. Two sensors were of 100 N force range and

the third sensor was of 450 N force range. These singletact sensors give output in digital

scale. The 100 N force sensor gives output 0 to 511 for force 0 N to 100 N and the 450 N

force sensor gives output 0 to 511 for force 0 N to 4500 N. So, the digital output was

converted into force values by eqn. 6.1 for 450 N sensor and eqn. 6.2 for 100 N sensor.

$$Force\ in\ newton = \frac{450}{511} \times Digital\ Output \qquad (6.1)$$

$$Force\ in\ newton = \frac{100}{511} \times Digital\ Output \qquad (6.2)$$
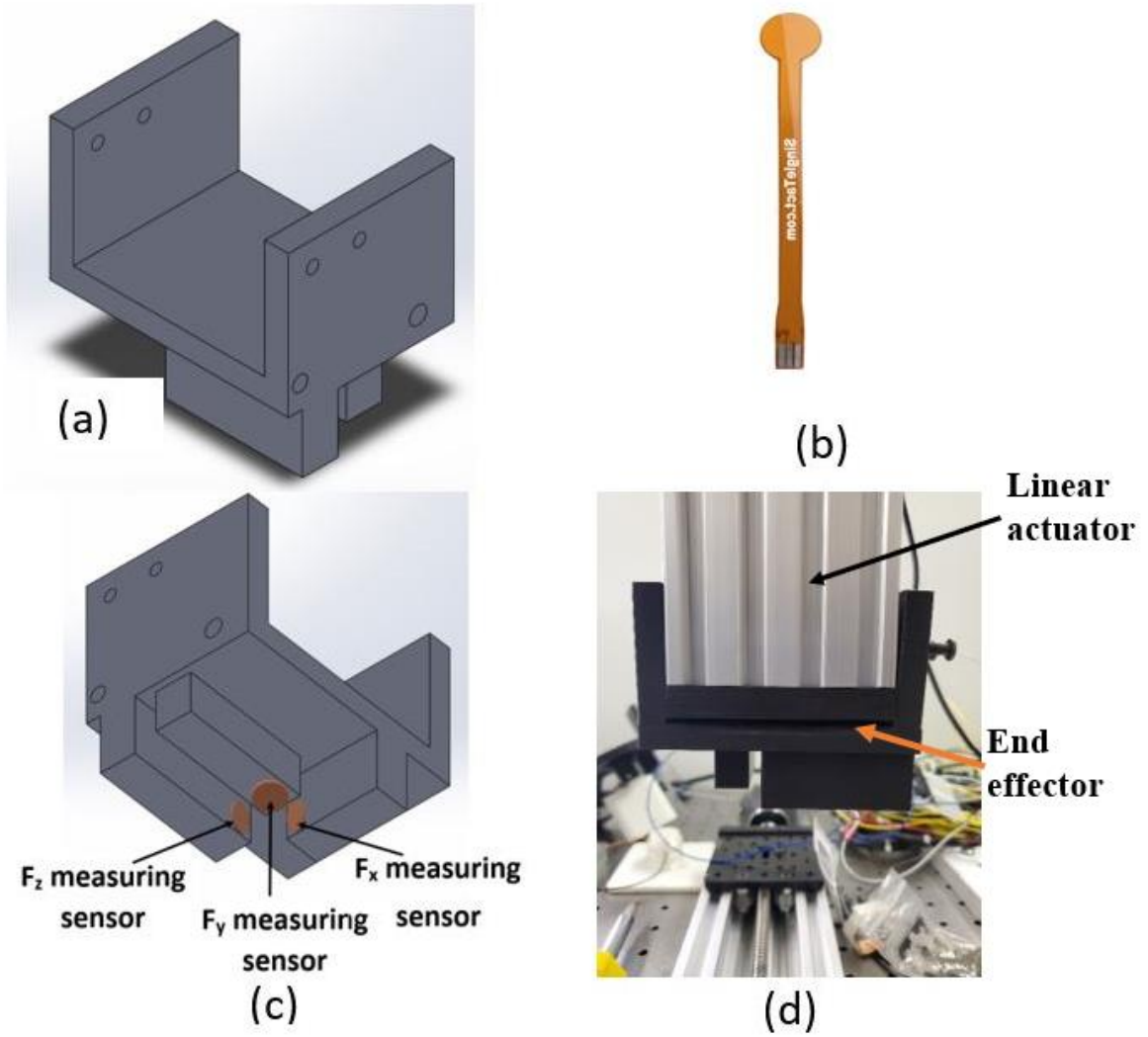
Figure 6.2: The end effector of the test setup including (a) an isometric view of the end effector, (b) a Singletact sensor, (c) the placement of Singletact sensors on the end effector, and (d) the end effector attachment to the setup.

6.2 Experiments

First experiment was done to find the calibration matrix. Then four experiments were done to evaluate the developed sensor. The experiments included – 1) static response, 2) zero-drift analysis, 3) repeatability and maximum hysteresis, 4) time-domain response, and 5) combined condition.

6.2.1 Calibration Matrix

According to the theoretical analysis in section 2.4, the forces were applied in each direction to find the calibration matrix. First, forces were applied in x – direction. The force was increased gradually from 0 N to 100 N. The applied force data were recorded using the reference Singletact sensor and the capacitance data were collected from the developed sensor. Then, the force was applied in y – and z – directions in similar way. The linear least square method was used to calculate the calibration matrix from the applied force data and the capacitance change data. The calibration matrix is shown in eqn. (6.3).

$$C = \begin{bmatrix} 1.82 & 2.71 & 3.51 \\ 4.25 & 3.32 & 1.48 \\ -0.06 & 4.84 & 2.31 \end{bmatrix} \tag{6.3}$$

To test the calibration matrix, forces were applied on the developed sensor in each direction and the errors were calculated from each data point. When the forces were applied in one direction, the developed sensor gave force value for only that direction only and gave close to zero value for all other directions. First, the forces were applied in x – direction. Figure 6.3 shows the plots of the results. The comparison between

reference sensor data and the developed sensor data is shown in Fig. 6.3 (a). From this

plot, it can be seen that the developed sensor gave the force values only in x – direction.

The force values for both y – and z – direction was close to zero. Figure 6.3 (b), (c), and

(d) show the bar plot of the error in each data point for the applied forces for x –, y –, and

z – direction, respectively. The errors mostly occurred around 40 N and 80 N. The errors

were very low when the applied force was less than 20 N. Table 6.1 shows the mean

errors with standard deviations (SD) in newton. From Table 6.1, when the forces were

applied in x – direction, the mean error for x – direction was 2.31 N with a standard

deviation of 2.38 N, the mean error for y – direction was 1.83 N with a standard deviation

of 1.72 N, and the mean error for z – direction was 3.10 N with a standard deviation of

2.44 N. Then forces were applied in y – direction. Figure 6.4 shows the results for this

experiment. Figure 6.4 (a) shows the comparison between the reference sensor data and

the developed sensor data. And Fig. 6.4 (b), (c), and (d) show the bar plot of the errors in

each direction. From the bar plots, the errors in x – direction were much smaller

comparatively to y – and z – directions. The amount of error in y – direction was higher

when forces are applied from 15 N to 50 N.

From Table 6.1, when forces were applied in y – direction the mean error in x –

direction was 1.37 N with a standard deviation of 1.08 N, the mean error in y – direction

was 3.91 N with a standard deviation of 3.23 N, and the mean error in z – direction was

2.52 N with a standard deviation of 1.90 N.

Figure 6.5 shows the plot of the results when forces were applied in z – direction.

Figure 6.5 (a) shows the comparison between reference sensor data and the developed

sensor data. Here, it can be seen that the developed sensor only gave force values for z –

direction only. The data for x – and y – direction were close to zero. Thus, the developed

sensor could distinguish when forces are applied in z – direction only. Figure 6.5 (b), (c),

and (d) show the bar plots of errors in x –, y –, and z – direction respectively. The errors

in x – direction was much smaller. The mean error was 0.62 N, and the standard

deviation is 0.7 N (Table 6.1). The amount of errors in y – and z – direction was higher

when force was applied in the range of 30 N to 45 N. The mean of errors in y – direction

was 2.14 N with a standard deviation of 1.53. In case of errors in z – direction, the mean

was 4.38 N, and the standard deviation is 3.49 N.

Table 6.1: Mean (±SD) error in each direction for each directional force

Force	F_x (N)	F_y (N)	F_z (N)
F_x	2.31(±2.38)	1.83(±1.72)	3.10(±2.44)
F_y	1.37(±1.08)	3.91(±3.23)	2.53(±1.90)
F_z	0.62(±0.7)	2.14(±1.53)	4.38(±3.49)
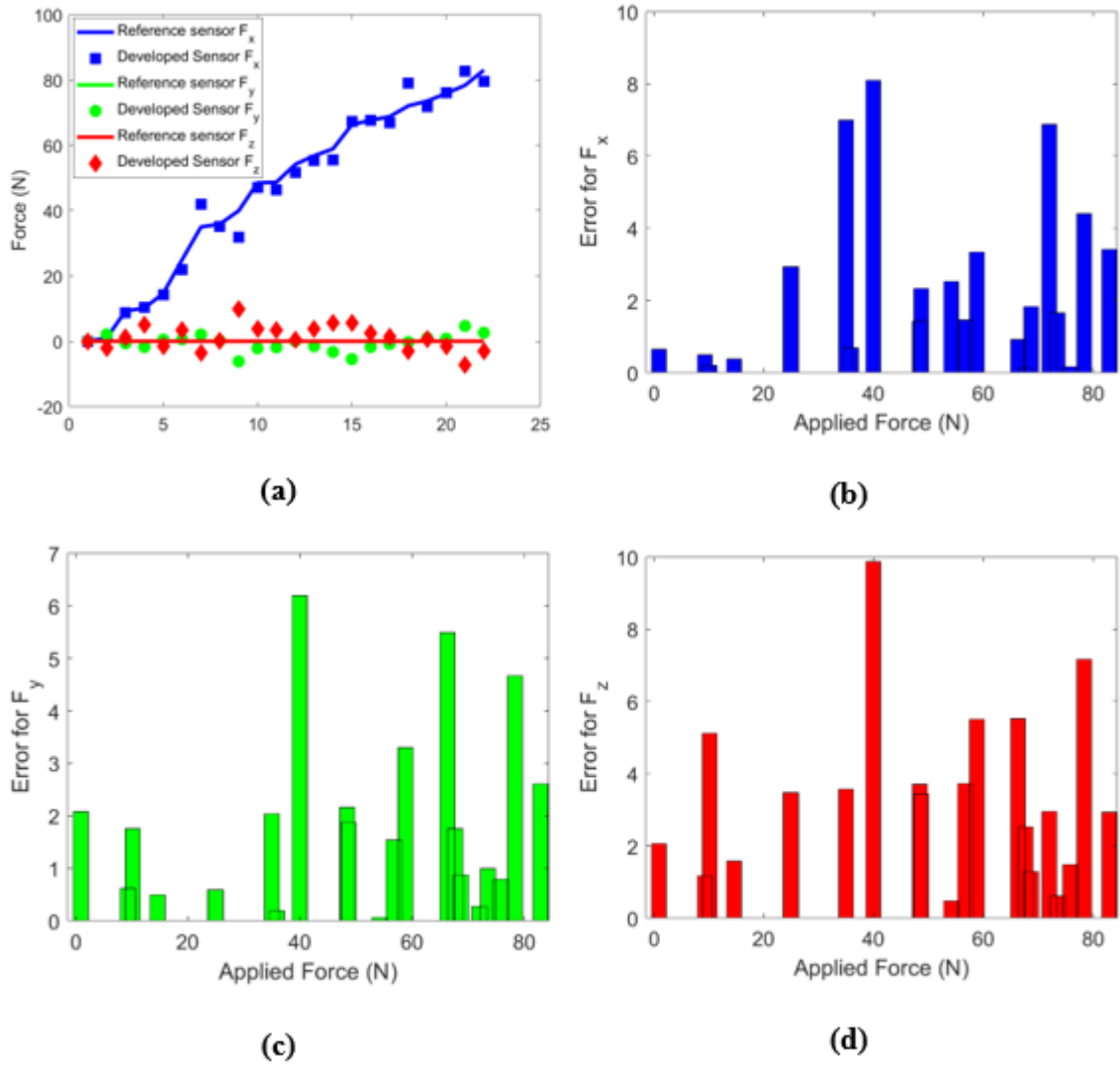
Figure 6.3: The experimental results when the force was applied in x-direction: (a) comparison between reference sensor and developed sensor, (b) error for F_x, (c) error for F_y, and (d) error for F_z
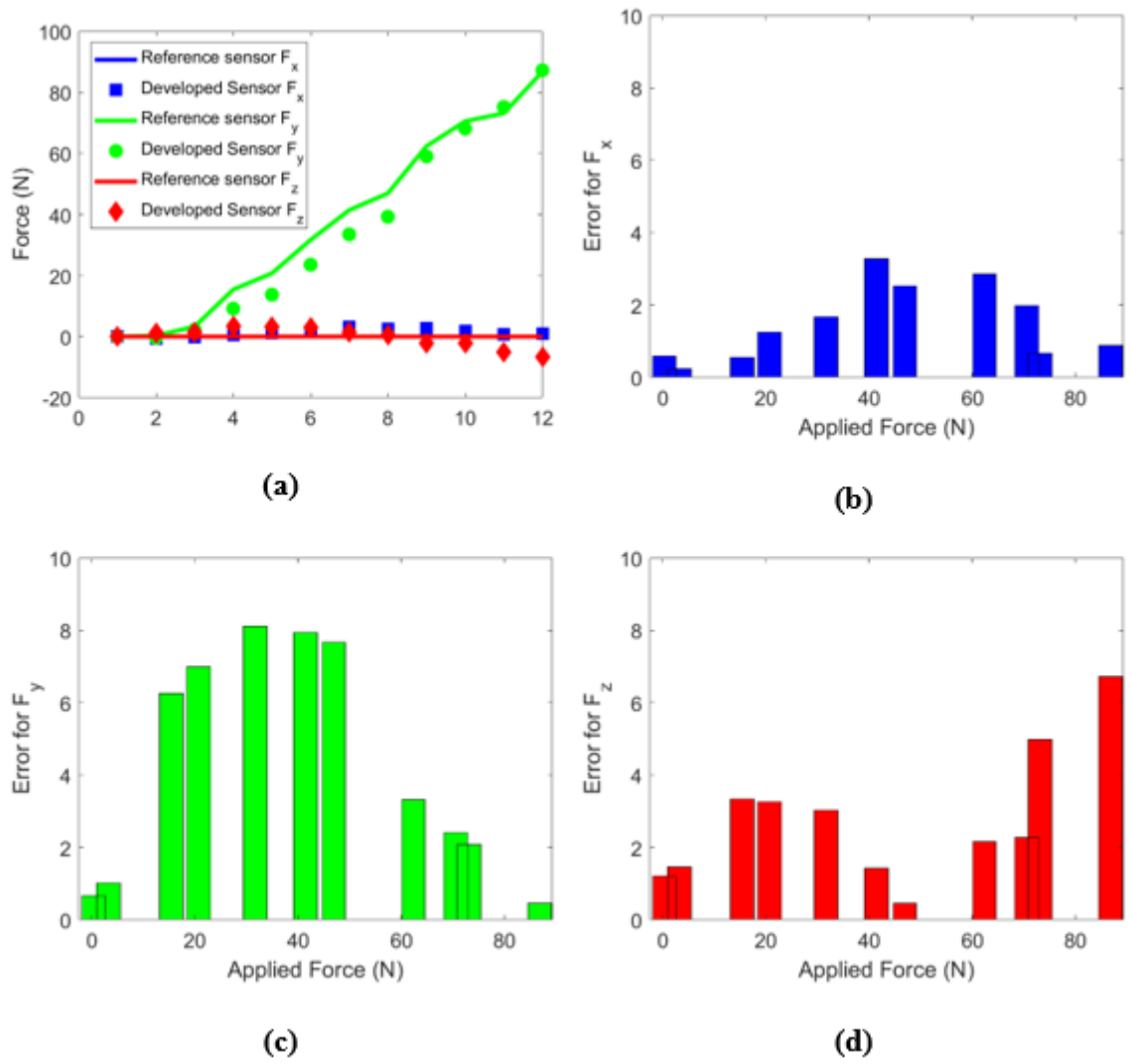
Figure 6.4: The experimental results when the force was applied in y-direction: (a) comparison between reference sensor and developed sensor, (b) error for F_x, (c) error for F_y, and (d) error for F_z
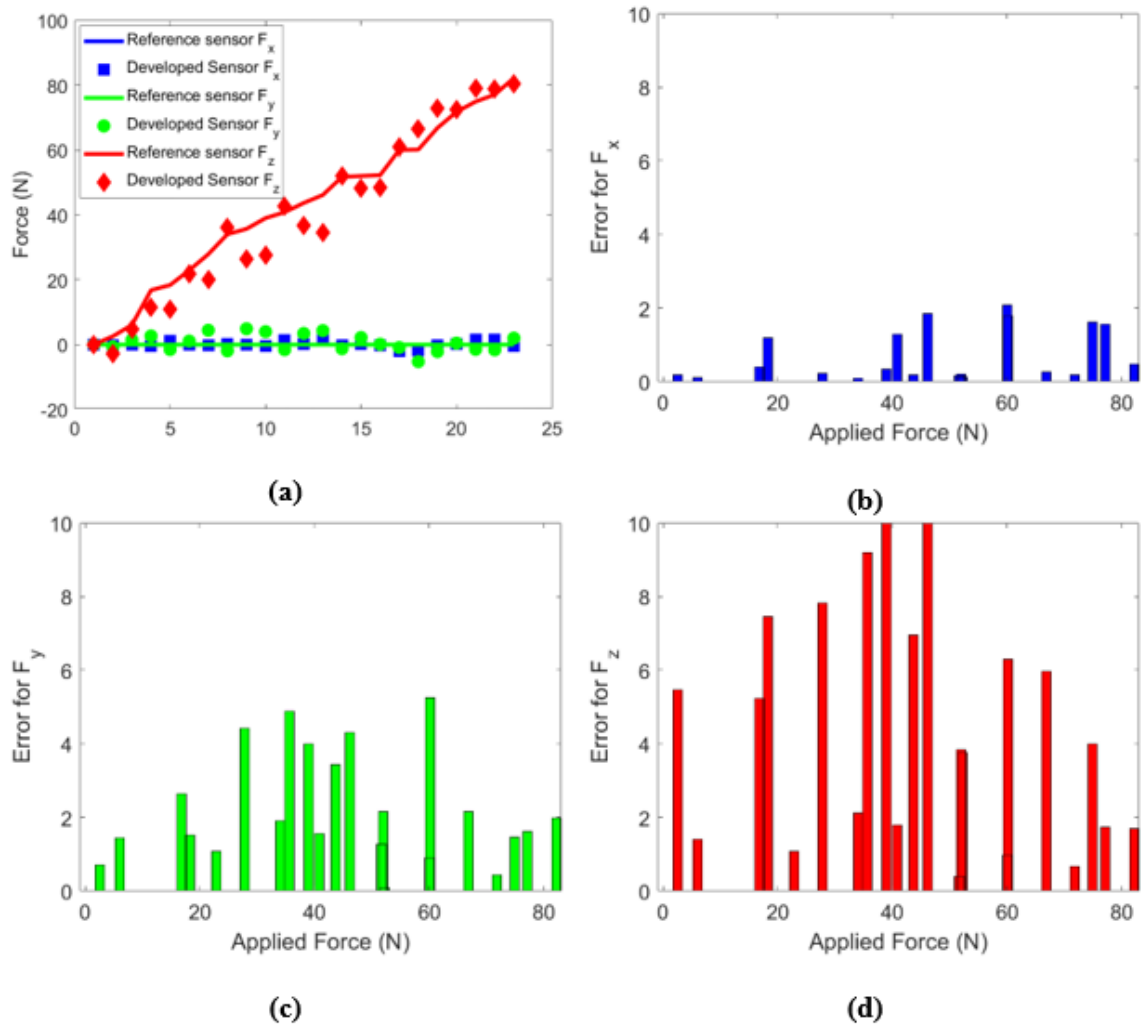
Figure 6.5: The experimental results when the force was applied in z-direction: (a) comparison between reference sensor and developed sensor, (b) error for F_x, (c) error for F_y, and (d) error for F_z

So, the calibration matrix could give force values in each direction from the capacitance data. When forces were applied in one direction, it gave force values in that direction only. The response for other direction was close to zero.

6.2.2 Static Response

Similar to the calibration experiment, forces were applied in each direction at a time. Forces were gradually increased from 0 N to 100 N. From the Fig. 6.6 of applied force vs. developed sensor data, the static response of the developed sensor can be evaluated. The slopes of the linear-fitted lines of the static responses give static accuracy values. The static accuracy value is unitless, and ideally, the slope should be 1 in the axis the force is applied and rests should be zero.

Figure 6.6 (a) shows the static response of the developed sensor when forces were applied in x – direction. From the plot, the force values in all directions were close to zero except the x – direction. From Table 6.2, the slope of the linear-fitted line in x – direction is 0.9935 which is close to 1. In rest of the directions, the slope of the linear-fitted line is close to zero. Figure 6.6 (b) and (c) show the static response for the y – and z – direction forces. When forces were applied in y – direction, the slope of the y – direction linear fitted line was also close to 1 (0.9498), and for the rest of the directions the slope was close to zero. Similarly, when forces were applied in z – axis direction, the slope was close to 1 for only z – direction, and for rest of the directions, it was close to zero.
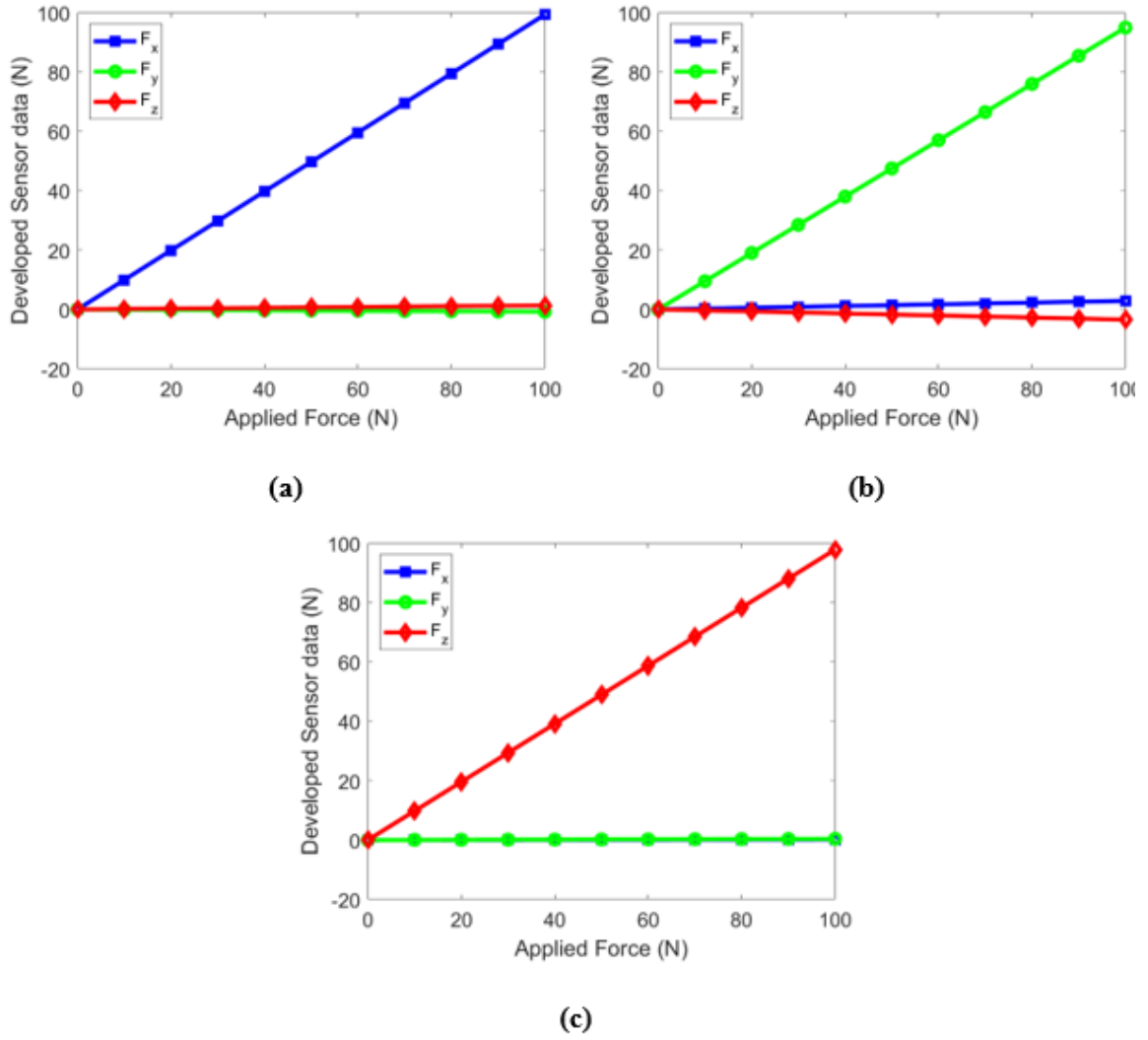
Figure 6.6: The static response of the developed sensor for (a) F_x, (b) F_y, and (c) F_z

Table 6.2: Static accuracy of the developed sensor

Applied Force	F_x	F_y	F_z
F_x	0.9935	-0.0078	0.0134
F_y	0.0287	0.9498	-0.0344
F_z	0.0019	0.0040	0.9789

6.2.3 Drift over Time

The amount of drift over time of the developed sensor was evaluated by recording the output capacitance data for 25 minutes. Figure 6.7 shows the drift of the developed sensor over time in all three directions. The average of the developed sensor in x – direction was 0.46 N, in y – direction was 0.81 N, and in z – direction was 1.21 N. So, the developed sensor can be used for long time.
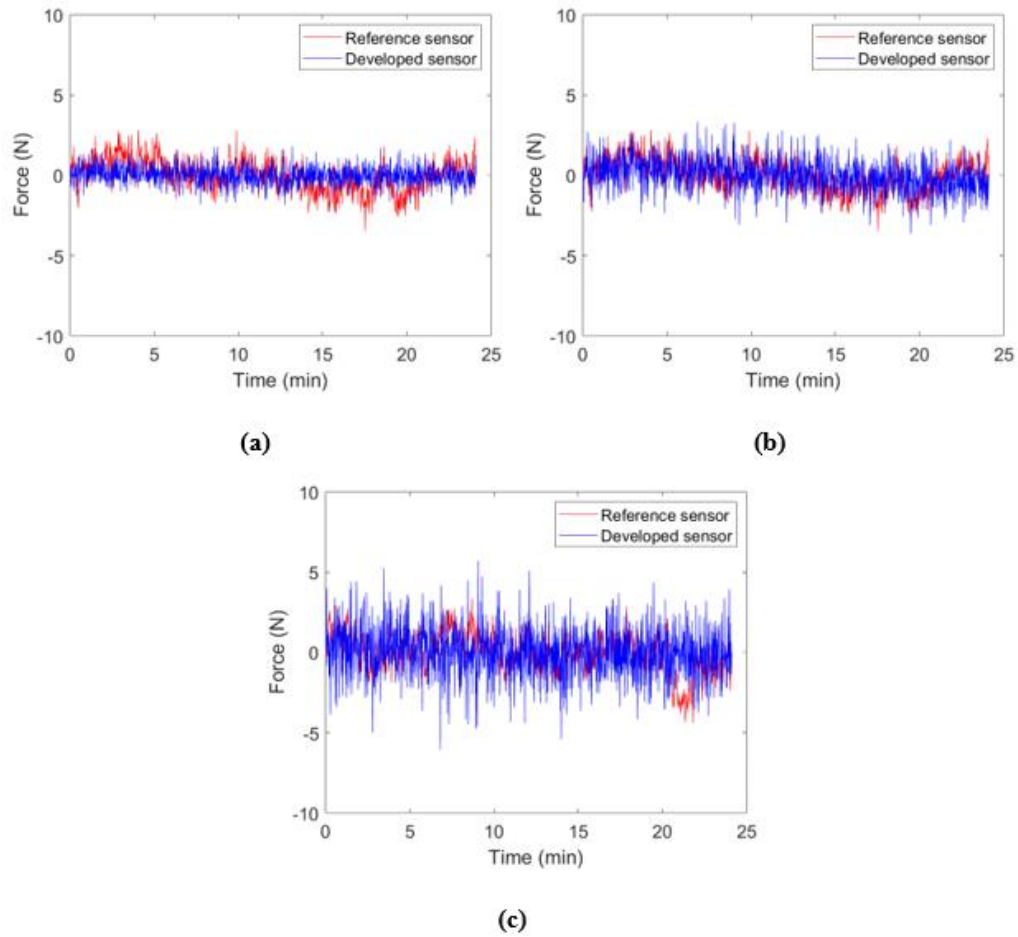
Figure 6.7: Drift of the developed sensor over time (a) F_x, (b) F_y, and (c) F_z

6.2.4 Hysteresis and Repeatability

The hysteresis and repeatability of the developed sensor were evaluated by calculating the maximum hysteresis, the difference between developed sensor data when no forces were applied at the beginning loading and at the end of unloading (Drift – 0), and difference between developed sensor data when maximum force is applied (Drift – 1). This was done by loading and unloading forces five times in each three direction. The forces were applied and released gradually, and the force data were collected from both reference sensor and developed sensor. Figure 6.8 shows the plot of the reference sensor vs. the applied force data for the hysteresis and repeatability test. The maximum difference between the developed sensor data during loading and unloading is called the maximum hysteresis.

Table 6.3 shows the maximum hysteresis and repeatability results of the developed sensor in all three directions. The hysteresis and repeatability errors were low and did not increase over time. So, the developed sensor can be used to measure any repetitive loading-unloading forces.

Table 6.3: Hysteresis and repeatability of the developed sensor

Applied Force	Max. hysteresis (N)	Drift – 0 (N)	Drift – 1 (N)
F_x	3.4656 at 3rd cycle	3.1747	5.9276
F_y	2.7519at 4th cycle	1.6080	5.9820
F_z	5.7469 at 1st cycle	4.7634	7.2863
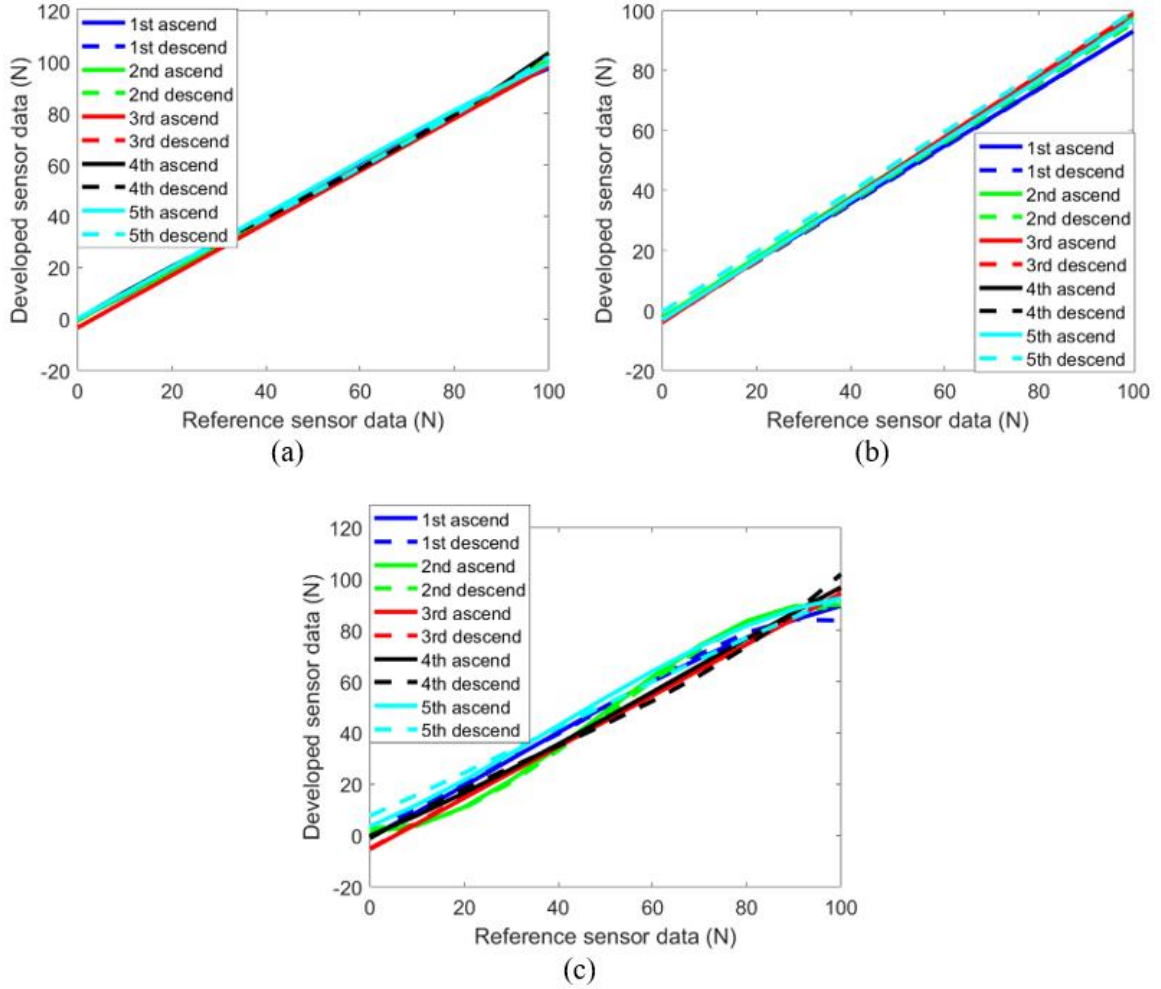
Figure 6.8: Plot for the hysteresis and repeatability test

6.2.5 Time-domain Response

To evaluate the time-domain response of the developed sensor, forces were gradually increase and decrease in each three directions. Figure 6.9 shows the time-domain response of the developed sensor. The developed sensor responded quickly to the applied forces, and matched the reference sensor data. Also, when forces were applied in

x – direction, there were not much response in y – and z – direction. The developed sensor responded in only x – direction. Similarly, when forces were gradually increase and decrease in y – direction, the developed sensor responded in only y – direction, and when forces were applied in z – direction, the developed sensor responded in z – direction only.
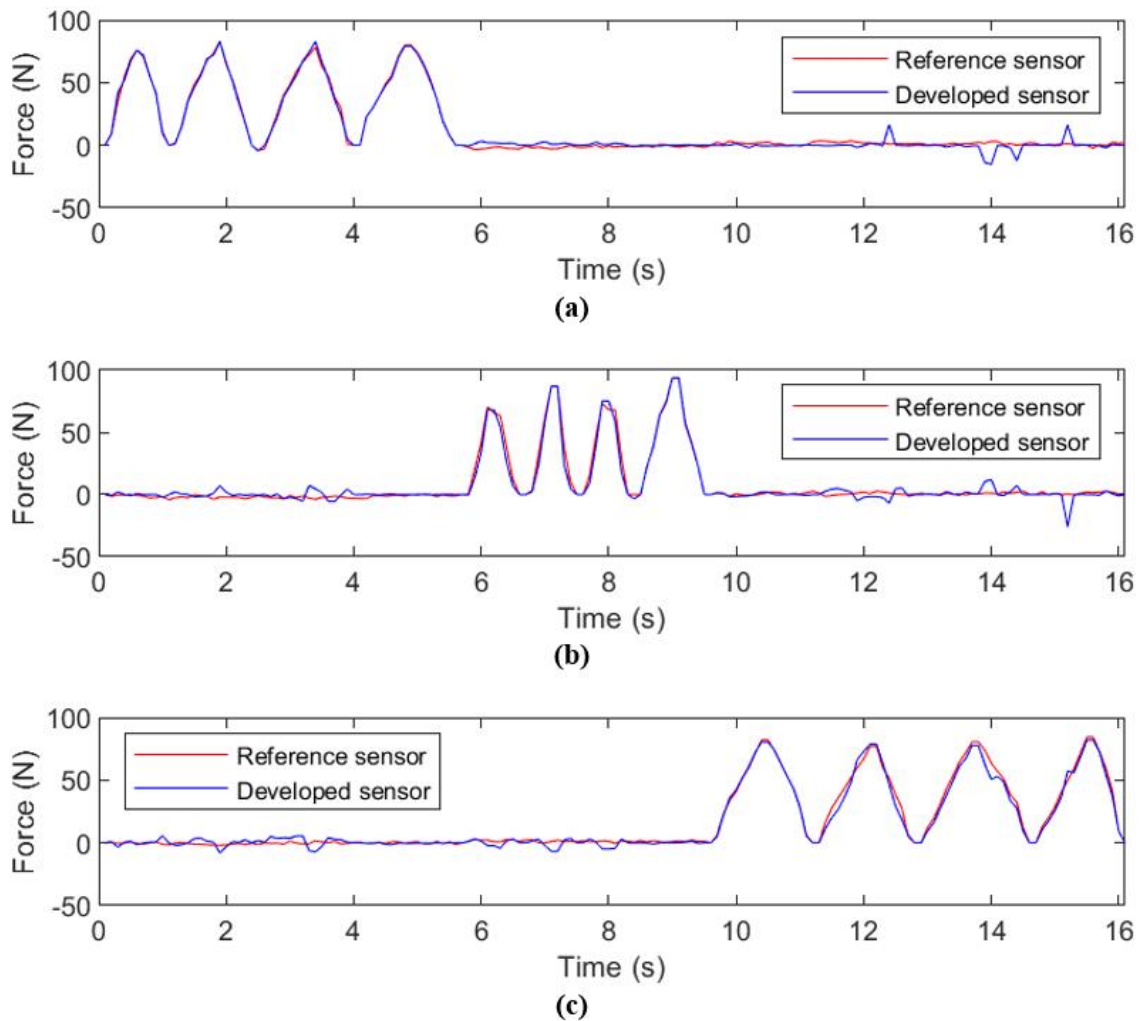
Figure 6.9: The time-domain responses of the developed sensor when the force was applied in (a) x – axis, (b) y – axis, and (c) z – axis

6.2.6 Combined Case

In the previous experiments, forces were applied in only one direction at a time. This experiment evaluates the performance of the developed sensor when multi-directional forces were applied at the same time. The experiment was done in two way. First a constant normal force (F_y) was applied and then the shear force in x – direction was increased gradually. Developed sensor's performance was evaluated by comparing with the reference sensor. Then a constant shear force in x – direction was applied and then the normal force in y – direction was increased gradually.

The developed sensor's performance was evaluated same as before. Figure 6.10 shows the performance of the developed sensor for this combined test. In Fig. 6.10 (a), the results are showing the sensor's performance when a constant normal force in y – direction was applied and force in x – direction was increased gradually. From the figure, the developed sensor could give force value for the constant force in y – axis direction and also could detect the gradual increase of force in x – direction. Figure 6.10 (b) shows the performance of the developed sensor when a constant force in x – direction was applied, and force was increased gradually in y – axis direction. From the plot, this time also the developed sensor can detect both the constant force in x – axis direction and the gradual increase in force in y – axis direction. So, the developed sensor not only can give measurement of the applied force in three directions individually but also can give measurement when forces are combinedly applied in multi-direction.

When a constant force in y – direction was applied and gradual increase of force in x – direction was applied, the mean error in x – direction measurement was 7.8 with a standard deviation of 4.9, the mean error in y – direction was 3.8 with a standard

deviation 3.1, and the mean error in z – direction measurement was 8.28 with a standard deviation of 3.9. But when a constant force in x – direction and gradually increase of force in y – direction was applied, the mean error in x – direction force measurement was 19.8 with a standard deviation of 6.9, the mean error in y – direction was 16.9 with a standard deviation of 13.5, and the mean error in z – direction was 26.7 with a standard deviation of 27. So, the errors were higher in constant force in x – direction and gradual increase in force in y – direction

(a)   (b)
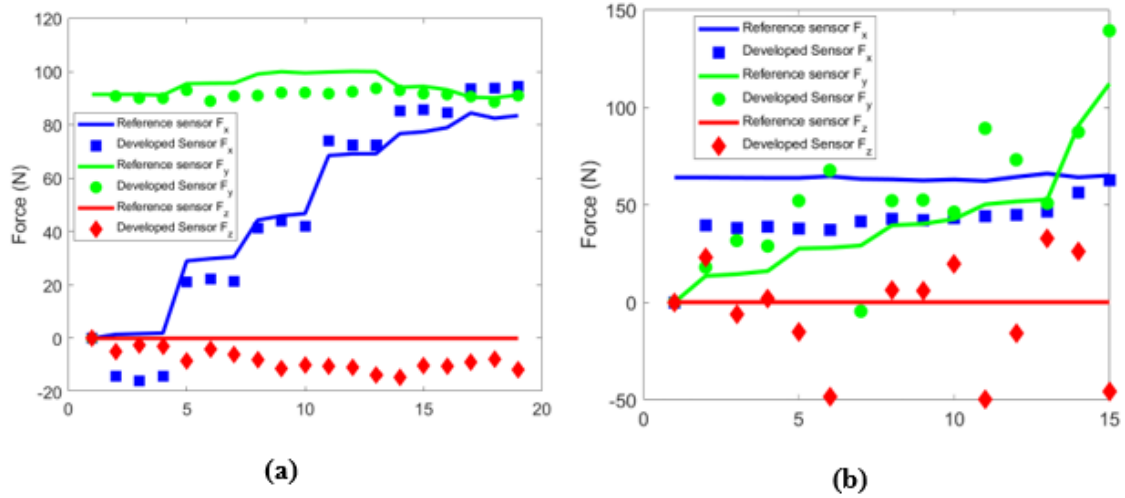
Figure 6.10: Evaluation of the developed sensor when forces are applied in multi-direction together (a) constant normal force in y-direction and gradually increasing shear force in x-direction, and (b) constant shear force in x-direction and gradually increasing normal force in y-direction

CHAPTER 7

CONCLUSION

The capacitive based three-dimensional force measuring can measure force in three directions, and it can be used to measure the ground reaction forces for doing gait analysis. We found a calibration matrix that established a sufficiently accurate relation between the applied forces and the capacitance readings. In all the three directions, the mean errors of the force measurement are below 4.5%. The standard deviations are also low. The static response of the developed sensor showed that the sensor responded only the direction of applied force. Also, the sensor can be used for a long time. The time drift analysis showed that the electrical signal does not significantly change over time, and the sensor can be used for a repetitive loading and unloading. As the applied forces were below the elastic limit of the elastic element, the sensor showed good hysteresis characteristics. In the combined condition, the errors were larger than the single direction forces, and the errors were larger when a constant shear force and gradually increasing normal force is applied. Future work can be done to reduce error during the combined condition.

In this work, the dimension of the elastic element was chosen by performing simulations in the COMSOL. The theoretical analysis is critical to choose the dimensions. An optimization framework which can find these dimensions by optimizing

the elastic element for the given force range will be very helpful. The modeling and simulation of the whole sensor will be very helpful to analyze different elastic element design and different measuring element design which will be helpful to reduce the errors more. Currently, the data is transfer through wires. A Bluetooth enabled microcontroller can make the developed sensor completely wireless.

REFERENCES

[1]   M. W. Whittle, *Gait analysis: an introduction*, 4th ed. Edinburgh: Butterworth-Heinemann.

[2]   W. Pirker and R. Katzenschlager, "Gait disorders in adults and the elderly: A clinical guide," *Wiener Klinische Wochenschrift*, vol. 129, no. 3–4. pp. 81–95, 2017.

[3]   R. L. Waters and S. Mulroy, "The energy expenditure of normal and pathologic gait," *Gait Posture*, vol. 9, no. 3, pp. 207–231, 1999.

[4]   C. M. Said, P. A. Goldie, A. E. Patla, W. A. Sparrow, and K. E. Martin, "Obstacle crossing in subjects with stroke," *Arch. Phys. Med. Rehabil.*, vol. 80, no. 9, pp. 1054–1059, 1999.

[5]   "Balance Disorders," *SpringerReference*. 2012.

[6]   R. B. Davis, S. Ounpuu, D. Tyburski, and J. R. Gage, "A gait analysis data collection and reduction technique," *Human Movement Science*, vol. 10. pp. 575–597, 1991.

[7]   R. Baker, "Gait analysis methods in rehabilitation," *J. Neuroeng. Rehabil.*, vol. 3, pp. 1–10, 2006.

[8]   C. M. Powers, S. Rao, and J. Perry, "Knee kinetics in trans-tibial amputee gait," *Gait Posture*, vol. 8, no. 1, pp. 1–7, 1998.

[9]   A. M. Howell, T. Kobayashi, H. A. Hayes, K. B. Foreman, and S. J. M. Bamberg, "Kinetic gait analysis using a low-cost insole," *IEEE Trans. Biomed. Eng.*, vol. 60, no. 12, pp. 3284–3290, 2013.

[10]   C. J. Chen and L. S. Chou, "Center of mass position relative to the ankle during walking: A clinically feasible detection method for gait imbalance," *Gait Posture*, vol. 31, no. 3, pp. 391–393, 2010.

[11]   G. Bovi, M. Rabuffetti, P. Mazzoleni, and M. Ferrarin, "A multiple-task gait analysis approach: Kinematic, kinetic and EMG reference data for healthy young and adult subjects," *Gait Posture*, vol. 33, no. 1, pp. 6–13, 2011.

[12]   P. Mahaudens, X. Banse, M. Mousny, and C. Detrembleur, "Gait in adolescent idiopathic scoliosis: Kinematics and electromyographic analysis," *Eur. Spine J.*, vol. 18, no. 4, pp. 512–521, 2009.

[13]   S. Y. Yoon, S. C. Lee, Y. sil An, and Y. W. Kim, "Neural correlates and gait characteristics for hypoxic-ischemic brain injury induced freezing of gait," *Clin. Neurophysiol.*, vol. 131, no. 1, pp. 46–53, 2020.

[14] J. F. Item-Glatthorn and N. A. Maffiuletti, "Clinical assessment of spatiotemporal gait parameters in patients and older adults," *J. Vis. Exp.*, no. 93, pp. 1–6, 2014.

[15] S. Barker, R. Craik, W. Freedman, N. Herrmann, and H. Hillstrom, "Accuracy, reliability, and validity of a spatiotemporal gait analysis system," *Med. Eng. Phys.*, vol. 28, no. 5, pp. 460–467, 2006.

[16] K. A. Pierz, J. R. Lloyd, M. J. Solomito, P. Mack, and S. Õunpuu, "Lower extremity characteristics in recurrent clubfoot: Clinical and gait analysis findings that may influence decisions for additional surgery," *Gait Posture*, vol. 75, no. August 2019, pp. 85–92, 2020.

[17] P. Ornetti, J. F. Maillefert, D. Laroche, C. Morisset, M. Dougados, and L. Gossec, "Gait analysis as a quantifiable outcome measure in hip or knee osteoarthritis: A systematic review," *Jt. Bone Spine*, vol. 77, no. 5, pp. 421–425, 2010.

[18] P. Krawetz and P. Nance, "Gait analysis of spinal cord injured subjects: Effects of injury level and spasticity," *Arch. Phys. Med. Rehabil.*, vol. 77, no. 7, pp. 635–638, 1996.

[19] M. Saleh and G. Murdoch, "In defence of gait analysis. Observation and measurement in gait assessment," *J. Bone Jt. Surg. - Ser. B*, vol. 67, no. 2, pp. 237–241, 1985.

[20] S. E. Lord, P. W. Halligan, and D. T. Wade, "Visual gait analysis: The development of a clinical assessment and scale," *Clin. Rehabil.*, vol. 12, no. 2, pp. 107–119, 1998.

[21] C. M. O'Connor, S. K. Thorpe, M. J. O'Malley, and C. L. Vaughan, "Automatic detection of gait events using kinematic data," *Gait Posture*, vol. 25, no. 3, pp. 469–474, 2007.

[22] R. G. Cutlip, C. Mancinelli, F. Huber, and J. Dipasquale, "Evaluation of an instrumented walkway for measurement of the kinematic parameters of gait," *Gait Posture*, vol. 12, no. 2, pp. 134–138, 2000.

[23] M. A. Finley and R. Y. Lee, "Effect of sitting posture on 3-dimensional scapular kinematics measured by skin-mounted electromagnetic tracking sensors," *Arch. Phys. Med. Rehabil.*, vol. 84, no. 4, pp. 563–568, 2003.

[24] K. Kobayashi, L. Gransberg, E. Knutsson, and P. Nolén, "A new system for three-dimensional gait recording using electromagnetic tracking," *Gait Posture*, vol. 6, no. 1, pp. 63–75, 1997.

[25] P. M. Mills, S. Morrison, D. G. Lloyd, and R. S. Barrett, "Repeatability of 3D gait kinematics obtained from an electromagnetic tracking system during treadmill locomotion," *J. Biomech.*, vol. 40, no. 7, pp. 1504–1511, 2007.

[26] A. D. Milne, D. G. Chess, J. A. Johnson, and G. King, "Accuracy of an electromagnetic tracking device: A study of the optimal operating range and metal interference," *J. Biomech.*, vol. 29, no. 6, pp. 791–793, 1996.

[27] A. Ishihara, S. M. Reed, P. J. Rajala-Schultz, J. T. Robertson, and A. L. Bertone, "Use of kinetic gait analysis for detection, quantification, and differentiation of hind limb lameness and spinal ataxia in horses," *J. Am. Vet. Med. Assoc.*, vol. 234, no. 5, pp. 644–651, 2009.

[28] T. Marasovič, M. Cecič, and V. Zanchi, "Analysis and interpretation of ground reaction forces in normal gait," *WSEAS Trans. Syst.*, vol. 8, no. 9, pp. 1105–1114, 2009.

[29] P. O. Riley, J. Dicharry, J. Franz, U. Della Croce, R. P. Wilder, and D. C. Kerrigan, "A kinematics and kinetic comparison of overground and treadmill running," *Med. Sci. Sports Exerc.*, vol. 40, no. 6, pp. 1093–1100, 2008.

[30] R. Kram, T. M. Griffin, J. M. Donelan, Y. H. U. I. Chang, T. M. Griffin, and J. Maxwell, "Force treadmill for measuring vertical and horizontal ground reaction forces," p. J. Appl. Physiol. 85(2): 764–769, 1998.

[31] F. Dierick, M. Penta, D. Renaut, and C. Detrembleur, "A force measuring treadmill in clinical gait analysis," *Gait Posture*, vol. 20, no. 3, pp. 299–303, 2004.

[32] K. F. Orishimo, I. J. Kremenic, A. J. Deshmukh, S. J. Nicholas, and J. A. Rodriguez, "Does total knee arthroplasty change frontal plane knee biomechanics during gait?," *Clin. Orthop. Relat. Res.*, vol. 470, no. 4, pp. 1171–1176, 2012.

[33] F. Alton, L. Baldey, S. Caplan, and M. C. Morrissey, "A kinematic comparison of overground and treadmill walking," *Clin. Biomech.*, vol. 13, no. 6, pp. 434–440, 1998.

[34] P. G. Rosquist *et al.*, "Estimation of 3D Ground Reaction Force Using Nanocomposite Piezo-Responsive Foam Sensors During Walking," *Ann. Biomed. Eng.*, vol. 45, no. 9, pp. 2122–2134, 2017.

[35] A. Forner Cordero, H. J. F. M. Koopman, and F. C. T. Van Der Helm, "Use of pressure insoles to calculate the complete ground reaction forces," *J. Biomech.*, vol. 37, no. 9, pp. 1427–1432, 2004.

[36] D. T. P. Fong, Y. Y. Chan, Y. Hong, P. S. H. Yung, K. Y. Fung, and K. M. Chan, "Estimating the complete ground reaction forces with pressure insoles in walking," *J. Biomech.*, vol. 41, no. 11, pp. 2597–2601, 2008.

[37] H. Rouhani, J. Favre, X. Crevoisier, and K. Aminian, "Ambulatory assessment of 3D ground reaction force using plantar pressure distribution," *Gait Posture*, vol. 32, no. 3, pp. 311–316, 2010.

[38]   H. Rouhani, J. Favre, X. Crevoisier, and K. Aminian, "A wearable system for multi-segment foot kinetics measurement," *J. Biomech.*, vol. 47, no. 7, pp. 1704–1711, 2014.

[39]   S. A. Liu and H. L. Tzo, "A novel six-component force sensor of good measurement isotropy and sensitivities," vol. 100, no. 112, pp. 223–230, 2002.

[40]   A. A. De Carvalho, "A Strain Gauge Tactile Sensor for Finger-Mounted Applications," vol. 51, no. 1, pp. 18–22, 2002.

[41]   G. Mastinu, M. Gobbi, and G. Previati, "A New Six-axis Load Cell. Part I: Design," *Exp. Mech.*, vol. 51, no. 3, pp. 373–388, 2011.

[42]   R. S. Stoughton, "(12) United States Patent," no. 12, 2001.

[43]   J. W. Joo, K. S. Na, and D. I. Kang, "Design and evaluation of a six-component load cell," *Meas. J. Int. Meas. Confed.*, vol. 32, no. 2, pp. 125–133, 2002.

[44]   G. S. Kim, "Design of a six-axis wrist force/moment sensor using FEM and its fabrication for an intelligent robot," *Sensors Actuators, A Phys.*, vol. 133, no. 1, pp. 27–34, 2007.

[45]   J. E. Sanders, R. A. Miller, D. N. Berglund, and S. G. Zachariah, "A modular six-directional force sensor for prosthetic assessment: A technical note," *J. Rehabil. Res. Dev.*, vol. 34, no. 2, pp. 195–202, 1997.

[46]   T. P. Quinn and C. D. Mote, "Optimal design of an uncoupled six-degree-of-freedom dynamometer," *ASTM Spec. Tech. Publ.*, no. 1104, pp. 94–111, 1991.

[47]   J. Ma and A. Song, "Fast estimation of strains for cross-beams six-axis force/torque sensors by mechanical modeling," *Sensors (Switzerland)*, vol. 13, no. 5, pp. 6669–6686, 2013.

[48]   M. I. Tiwana, A. Shashank, S. J. Redmond, and N. H. Lovell, "Characterization of a capacitive tactile shear sensor for application in robotic and upper limb prostheses," *Sensors Actuators, A Phys.*, vol. 165, no. 2, pp. 164–172, 2011.

[49]   L. Viry *et al.*, "Flexible three-axial force sensor for soft and highly sensitive artificial touch," *Adv. Mater.*, vol. 26, no. 17, pp. 2659–2664, 2014.

[50]   P. Peng and R. Rajamani, "Flexible microtactile sensor for normal and shear elasticity measurements," *IEEE Trans. Ind. Electron.*, vol. 59, no. 12, pp. 4907–4913, 2012.

[51]   D. Kim *et al.*, "Six-axis capacitive force/torque sensor based on dielectric elastomer," *SPIE Smart Struct. Mater. Nondestruct. Eval. Heal. Monit.*, vol. 8687, p. 86872J, 2013.

[52] D. Lee, U. Kim, H. Jung, and H. R. Choi, "A Novel Six-Axis Force/Torque Sensor for Robotic Applications," vol. 16, no. 8, pp. 2290–2299, 2017.

[53] U. Kim, D. H. Lee, Y. B. Kim, D. Y. Seok, and H. R. Choi, "A novel six-axis force/torque sensor for robotic applications," *IEEE/ASME Trans. Mechatronics*, vol. 22, no. 3, pp. 1381–1391, 2017.

[54] H.-R. Choi, D.-H. Lee, U. Kim, T. Gulrez, B. Hannaford, and W. J. Yoon, "A Laparoscopic Grasping Tool with Force Sensing Capability," *IEEE/ASME Trans. Mechatronics*, vol. 21, no. 1, pp. 1–1, 2015.

[55] U. Kim, Y. B. Kim, D. Y. Seok, J. So, and H. R. Choi, "Development of surgical forceps integrated with a multi-axial force sensor for minimally invasive robotic surgery," *IEEE Int. Conf. Intell. Robot. Syst.*, vol. 2016–Novem, pp. 3684–3689, 2016.

[56] U. Kim, Y. B. Kim, J. So, D. Y. Seok, and H. R. Choi, "Sensorized surgical forceps for robotic-assisted minimally invasive surgery," *IEEE Trans. Ind. Electron.*, vol. 65, no. 12, pp. 9604–9613, 2018.

[57] U. Kim, Y. B. Kim, D. Y. Seok, J. So, and H. R. Choi, "A surgical palpation probe with 6-axis force/torque sensing capability for minimally invasive surgery," *IEEE Trans. Ind. Electron.*, vol. 65, no. 3, pp. 2755–2765, 2018.

[58] Q. Liang, D. Zhang, Q. Song, Y. Ge, H. Cao, and Y. Ge, "Design and fabrication of a six-dimensional wrist force/torque sensor based on E-type membranes compared to cross beams," *Meas. J. Int. Meas. Confed.*, vol. 43, no. 10, pp. 1702–1719, 2010.

[59] Q. Liang, D. Zhang, Y. Wang, G. Coppola, and Y. Ge, "PM based multi-component F/T sensors-State of the art and trends," *Robot. Comput. Integr. Manuf.*, vol. 29, no. 4, pp. 1–7, 2013.

[60] H. S. Oh, U. Kim, G. Kang, J. K. Seo, and H. R. Choi, "Multi-Axial Force/Torque Sensor Calibration Method Based on Deep-Learning," *IEEE Sens. J.*, vol. 18, no. 13, pp. 5485–5496, 2018.

BIOGRAPHY OF THE AUTHOR

Md Shafiqur Rahman was born in Mymensingh, Bangladesh on March 20, 1992. He was graduated with a Bachelor of Science in Mechanical Engineering from Khulna University of Engineering and Technology, Khulna, Bangladesh in July 2014. He worked as an instructor for a couple years and after that he began his graduate degree in Mechanical Engineering in the Fall 2018 at University of Maine with Dr. Babak Hejrati.

Md Shafiqur Rahman is a candidate for the Master of Science in Mechanical Engineering from the University of Maine in December 2020.